

# **Use of Wavelets and Filter Banks in 2D Gel Electrophoresis Images in Spot Picker Robot for Precise Protein Identification**

*By*

**Ratnesh Singh Sengar**

**< ENGG01201004024 >**

**Bhabha Atomic Research Centre, Mumbai**

*A thesis submitted to the*

*Board of Studies in Engineering Sciences*

*In partial fulfillment of requirements*

*for the Degree of*

**DOCTOR OF PHILOSOPHY**

*of*

**HOMI BHABHA NATIONAL INSTITUTE**



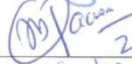
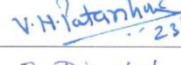
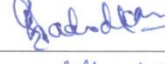
**February, 2017**

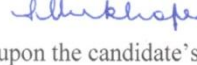
# Homi Bhabha National Institute

## Recommendations of the Viva-Voce Board

As members of the Viva Voce Board, we certify that we have read the dissertation prepared by **Ratnesh Singh Sengar** titled "Use of Wavelets and Filter Banks in 2D Gel Electrophoresis Images in Spot Picker Robot for Precise Protein Identification" and recommend that it may be accepted as fulfilling the thesis requirement for the award of Degree of Doctor of Philosophy.

### 1. Name and Signature of the Viva Voce Board (Doctoral Committee & External Examiner):

Sr No	Composition	Name	Signature with date
a.	Chairman	Dr. Archana Sharma	
b.	Convener (Guide)	Prof. Vikram M Gadre	 23.2.2017
c.	External Examiner	Prof. R.B.Pachori	 23/02/2017
d.	Member	Dr. Gopika Vinod	 23/02/2017
e.	Member	Dr. V.H.Patankar	 23/02/2017
g.	Member	Dr. B.Dikshit	 23/2/2017
f.	The Technology Adviser	DR. D. N. BADODKAR	 23/02/2017

g. Member - Expert Dr. S. Mukhopadhyay  23/2/17

Final approval and acceptance of this thesis is contingent upon the candidate's submission of the final copies of the thesis to HBNI.

I hereby certify that I have read this thesis prepared under my direction and recommend that it may be accepted as fulfilling the thesis requirement.

Date: 23 FEBRUARY 2017

Place: HBNI MUMBAI

 23.2.2017  
Prof. Vikram M Gadre  
(Guide & Convenor)

## **STATEMENT BY AUTHOR**

This dissertation has been submitted in partial fulfillment of requirements for an advanced degree at Homi Bhabha National Institute (HBNI) and is deposited in the Library to be made available to borrowers under rules of the HBNI.

Brief quotations from this dissertation are allowable without special permission, provided that accurate acknowledgement of source is made. Requests for permission for extended quotation from or reproduction of this manuscript in whole or in part may be granted by the Competent Authority of HBNI when in his or her judgment the proposed use of the material is in the interests of scholarship. In all other instances, however, permission must be obtained from the author.



(Ratnesh Singh Sengar)

## **DECLARATION**

I, hereby declare that the investigation presented in the thesis has been carried out by me. The work is original and has not been submitted earlier as a whole or in part for a degree / diploma at this or any other Institution / University.



(Ratnesh Singh Sengar)

# COURSES and PUBLICATIONS

## Courses Completed

भारतीय प्रौद्योगिकी संस्थान मुंबई  
INDIAN INSTITUTE OF TECHNOLOGY BOMBAY

पवई / POWAI, / मुंबई / MUMBAI 400 076

दिनांक / Date: 20-06-2021 **सत्र ग्रेड रिपोर्ट / SEMESTER GRADE REPORT**

छात्र / छात्रा का नाम Student's Name	रोल नं. Roll No.	सत्र Semester	वर्ष Year	विभाग काड Deptt. Code
R.S. Sengar	10V070007	2	1	EE

कार्यक्रम / Programme: **Visiting Students**

विभाग / Department: **Electrical Engineering**

पाठ्य क्रम क्र. Course Number	पाठ्य क्रम नाम Course Name	पाठ्य क्रम अंक Course Credit	आजत ग्रेड Grade Obtained
EE 678	Wavelets	6.0	AB
EE 702	Computer Vision	6.0	AB
--	----	--	--
--	----	--	--
--	----	--	--
--	----	--	--
--	----	--	--
--	----	--	--
--	----	--	--
--	----	--	--
--	----	--	--
--	----	--	--
--	----	--	--
--	----	--	--
--	----	--	--
--	----	--	--

टिप्पणा / Remarks:

चालू सत्र प्रदर्शन Current Semester Performance			सांचत प्रदर्शन Cummulative Performance		
कुल पंजाकृत अंक Total Credit Registered	ग्रेड प्वाइंट Grade Points	एसपाआइ SPI	कुल पंजाकृत अंक Total Credit Registered	ग्रेड प्वाइंट Grade Points	सापाआइ CPI
12.0	108.0	9.0	12.0	108.0	9.0

उप / सहायक कुलसाचव (शासक)  
Deputy/Asstt. Registrar(Academic)

*Asha*  
*HUP*  
20-6-21

## List of Publications arising from the thesis

### Journal

1. "Analysis of 2D-Gel Images for Detection of Protein Spots Using a Novel Nonseparable Wavelet Based Method", Ratnesh Singh Sengar, A. K. Upadhyay, M. Singh, V. M. Gadre, *Biomedical Signal Processing and Control(Elsevier journal)*, vol. 25, 2016, pp. 62-75, doi:10.1016/j.bspc.2015.10.013.
2. "Protein Spot Extraction in 2D Gel Images Using Sign of Wavelet Coefficients", Ratnesh Singh Sengar and V.M.Gadre. (Communicated)

### Chapters in books and lectures notes

1. "Wavelet and Fractals in Earth Science", Chapter-4: Multiscale Processing-A Boon for Self-similar Data, Data Compression, Singularities and Noise Removal", Ratnesh Sengar, Venkateswarao Cherukuri, Arpit Agrawal and Vikram M. Gadre, *CRC Press, Taylor & Francis Group*, 2013.

### Conferences

1. "Approaches based on nonseparable filter banks in 2D Gel electrophoresis image analysis", Ratnesh Singh Sengar, A. K. Upadhyay, P. G. Patwardhan, M. Singh, V. M. Gadre, *Proceedings of Asia Pacific Signal and Information Processing Association (APSIPA) International Conference*, Biopolis, Singapore, 2010, pp. 387-392, [www.scopus.com/inward/record.url?eid=2-s2.0-79958151381&partnerID=40&md5=a0de44adfb291971da479e13af6e41c](http://www.scopus.com/inward/record.url?eid=2-s2.0-79958151381&partnerID=40&md5=a0de44adfb291971da479e13af6e41c).
2. "Segmentation of two-dimensional electrophoresis gel image using the wavelet transform and the watershed transform", Ratnesh Singh Sengar, A. K. Upadhyay, M. Singh, V. M. Gadre, *The eighteenth annual National Conference on Communications (NCC-2012)*, (3-5 Feb. 2012), DOI:10.1109/NCC.2012.6176861.
3. "Development of Spot Picker Robot for Proteomics Applications", Ratnesh S Sengar, A.K.Upadhyay, D.N.Badodkar, R.K.Puri, Manjit Singh, MGR Rajan, Vikram M Gadre, *IEEE International Conference on Robotics & Automation (IEEE-ICRA2013) at Karlsruhe, Germany*, 2013, pp 1704-1709, DOI: 10.1109/ICRA.2013.6630801.

### Workshop

1. "Wavelets: Data Processing across Scales", Ratnesh S Sengar, Venkateshwararao Cherukuri, Satyaprakash Pareek, Arpit Agarwal, Vikram M. Gadre, *National Workshop on Wavelets, Multiresolution and Multifractal Analyses in Earth, Ocean and Atmospheric Sciences - Current Trends (WMMFA-2012), Session I, IIT, Bombay, Mumbai*, February 29 - March 2, 2012.



(Ratnesh Singh Sengar)

*Dedicated to my Parents*

## ACKNOWLEDGEMENTS

I would like to thank my guide, Prof. (Dr.) V. M. Gadre, Department of Electrical Engineering, IIT-Bombay for giving me the opportunity to pursue a PhD and for his excellent supervision, practical help, unabated inspiration, valuable suggestions and most untiring help at all stages, which has helped me to complete this project in the present form. I am particularly grateful to my office supervisors and technical advisor, Mr. Manjit Singh, Ex Director, DMA Group and Dr. D. N. Badodkar, Distinguish Scientist, Associate Director, DMAG & Head, DRHR for lending me their understanding, constructive guidance and support during my course work at IIT-Bombay. I would also like to thank my immediate supervisor Mr. R. K. Puri for his constant support and encouragement to complete my PhD work. A special thanks to Dr. Kallol Roy, Dr. Archana Sharma and other members of the Doctorate committee for giving me extremely helpful and logical suggestions, and everyone in my department (DRHR) for making this a very enjoyable time. I also extend my sincere thanks to Dr S. Mukhopadhyay, Head, Siesmology Division for useful suggestions and available for all the worthwhile discussions. I am extremely thankful to our DRHR, BARC colleagues Mr. A.K Upadhyay and Mr. Rohit Sharma, who gave their time and insight for the successful completion of my thesis. I would also like to thank Prof. Sanjeeva Srivastva, Biosciences & Bioengineering, IIT-Bombay, Dr. MGR Rajan (RMC, BARC), Dr. H.S.Mishra (MBD, BARC) and Dr. Bhakti Basu (MBD, BARC) for providing me with the required assistance and the gel images that were used in this thesis. I would like to thank the students of Electrical Engineering Department, IIT-Bombay who have contributed their time in helping me with this thesis and for fruitful discussions and critical review.

Finally, I would like to express my sincere gratitude to my wonderful parents for their love and support throughout the whole project. I would like to thank my wife Jaya for standing beside me during this project. I also thank my lovely children Swastika and Suryaansh for always making me smile and for understanding on those weekend morning when I was working on this project instead of spending time with them. A special thanks to my sister Rashmi for devoting her time and efforts with the editing of the thesis and providing insight to make it more meaningful.

# Contents

Abstract.....	iv
List of Figures .....	v
List of Tables .....	x
Chapter 1 Introduction .....	1
1.1 Motivation.....	1
1.2 The virtue of Proteomics.....	2
Two-Dimensional Gel Electrophoresis in Proteomics.....	2
1.3 Spot Picker Robot.....	7
1.3.1 Illumination System .....	7
1.3.2 Spot Cutting Tool.....	9
1.3.3 Robotic System.....	9
1.3.4 Control System and Software .....	10
1.3.5 Image Analysis of 2DGE Images .....	11
1.4 Literature for 2DGE Images Analysis.....	16
1.5 Problems Addressed in This Thesis .....	18
1.5.1 Contribution of This Thesis .....	19
Chapter 2 Multi-Scale Processing and Nonseparable Wavelets.....	22
2.1 Introduction .....	22
2.2 Dyadic Multiresolution Analysis (MRA) .....	23
2.2.1 Axioms of Dyadic MRA.....	24
2.2.2 Theorem of MRA.....	27
2.3 Singularities and Noise behavior.....	29
2.3.1 Singularities.....	29
2.3.2 Wavelets in Singularity Detection.....	30
2.4 Nonseparable Wavelet.....	33
2.4.1 Building Blocks of Multi-rate System .....	35
2.5 Quincunx Wavelet Transform .....	41
2.6 Lifting Scheme.....	44
Chapter 3 Denoising Of 2DGE Images.....	48
3.1 Introduction .....	48

3.2 Denoising Techniques .....	49
3.3 Wavelet Shrinkage Method .....	50
3.3.1 Motivation for Wavelet Shrinkage.....	50
3.3.2 Thresholding: Soft and Hard .....	52
3.3.3 Image Denoising Algorithm.....	53
3.3.4 Threshold Determination.....	53
3.4 Image Denoising: A Wavelet Domain Modeling Approach.....	56
3.4.1 Stochastic Model for Wavelet Coefficient .....	57
3.5 Use of Nonseparable Wavelet .....	62
3.6 Evaluation Methodology.....	62
3.6.1 PSNR Based Analysis on Synthetic Images.....	64
Chapter 4 Segmentation of Low-resolution 2DGE Images .....	72
4.1 Introduction .....	72
4.2 Method using Wavelet Transform and Watershed Transform .....	74
4.2.1 Watershed Transform and Problems.....	74
4.2.2 Proposed Segmentation Method.....	75
4.2.3 Experiments and Results.....	79
4.3 Method using Wavelet Interscale Ratios .....	82
4.3.1 Proposed Image Model.....	83
4.3.2 Image Decomposition .....	83
4.3.3 LMMSE Based Denoising.....	83
4.3.4 Discrimination Power of the Wavelet Coefficients.....	85
4.3.5 Discrimination among Spot Region, Edge and Background.....	87
4.3.6 Texture Characterization and Spot Detection .....	90
4.3.7 Energy Distribution Model.....	94
4.3.8 Oversaturated Spots .....	96
4.3.9 Overall Strategy.....	99
4.3.10 Experimental Results and Discussions .....	100
Chapter 5 Segmentation of High-resolution 2DGE Images.....	112
5.1 Introduction .....	112
5.2 Method using Wavelet and Kernel Density Estimation (KDE) .....	112
5.2.1 Foundation .....	113

5.2.2 Wavelet and Blob Regions .....	117
5.2.3 Proposed Method .....	120
5.2.4 Region Refinement.....	123
5.2.5 Experimental Results and Discussion.....	129
5.2.6 Detailed Results on Synthetic Image .....	142
Conclusion.....	148
Appendix I 2DGE Image Registration .....	150
I.1 Introduction .....	150
I.2 Registration Techniques.....	151
I.2.1 Intensity Based.....	151
I.2.2 Point Set Registration .....	153
References .....	157

## **Abstract**

The main aim of this thesis is to bring in novel advanced techniques for the analysis of two-dimensional gel electrophoresis (2DGE) images, to provide more accurate protein spot detection in the field of proteomics. 2DGE is an important and the most widely used technique for analyzing protein expression in this field. By this technique, a very large number of proteins can easily and simultaneously be separated, identified and characterized. Due to very tedious and laborious work involved in the separation of thousands of proteins, a completely automated integrated system for the analysis of 2DGE images and spot excision is increasingly in demand. The nature of 2DGE images poses some great challenges, such as very noisy and inhomogeneous background with several irregular protein spots. These irregular protein spots are of varying size, shape and intensity. In this Thesis, problems of noise removal and methods of image segmentation are addressed to solve various challenges, such as faint or weak spots, overlapped spots and streaks, to a great extent. These challenges lead us to develop three novel segmentation methods; each method provides different insights into the problem and exhibits significant improvements over the available commercial software and methods for 2DGE images.

The main contribution of the proposed algorithms is the use of nonseparable wavelets to study the nature of protein spots in the scale-space paradigm and to formulate efficient strategies for recognition. The first method analyzes the difference between streaks and spots, which are characterized in a nonseparable wavelet domain and combined with the watershed method for complete segmentation. In the second method, we have devised a technique to find out the faint spots by using inter-scale ratios of the wavelet coefficients. This technique is based on a single threshold and is independent of the gray value of the image. It copes with the inhomogeneities in the 2DGE images up to a large extent, which is helpful for finding the protein spots accurately. The third method emphasizes the minimization of artifacts and actual blob region identification in the noisy inhomogeneous background, by using kernel density estimation technique in the nonseparable wavelet domain.

## List of Figures

1.1	Laboratory process of making of 2DGE image	6
1.2	1D gel image	6
1.3	2D gel images	6
1.4	Spot Picker Robot	8
1.5	Typical flow of gel-based proteomics	8
1.6	Illumination Source	9
1.7	Spot Cutting Tool	9
1.8	Computer based control system for Spot Picker Robot	10
1.9	Spot cut from the gel (a) by Spot Picker Robot (b) by manual operation	11
1.10	Different types of protein spots	12
1.11	(a) A typical 2DGE image with varying background (b) Intensity line profile	13
1.12	a) Foreground intensity histogram (range covered 0-253)	14
	b) Background intensity histogram (range covered 20-255)	15
	c) Gel image histogram	15
2.1	Illustration of Ladder Axiom	25
2.2	Types of Singularities	29
2.3	Retention of singularities across the scales	31
2.4	Illustration of noise removal using 'db8': (a) original signal, (b) signal with additive random noise, (c) detail coefficients at scale 1, (d) detail coefficients at scale 2 and (e) detail coefficients at scale 3	32
2.5	Division of frequency region with 2D two channels separable filter banks, (a) vertical, (b) horizontal [34]	35
2.6	Lattice generated by Quincunx matrix	36
2.7	(a) Before down-sampling, (b) Down-sampling by Quincunx matrix	37
2.8	(a) Based-band region (b), (c) and (d) three aliases for decimation matrix M	38
2.9	Decimation	39
2.10	Up-sampling using matrix $M$ (a) (a) Input signal (b) Up-sampled signal	39
2.11	Interpolator	40
2.12	Perfect reconstruction filter bank	40
2.13	The Quincunx lattice (shaded point shows lattice points)	43
2.14	Quincunx filter bank	44

2.15	Frequency supports of filters in Quincunx filter bank	44
2.16	Lifting Structure for Quincunx filter Bank in (a)-Analysis and (b)-Synthesis	47
3.1	(a) Original signal with singularities (in black) and noisy signal (in yellow) (b) histogram of magnitude of `db6' wavelet coefficients of noisy signal	51
3.2	(a) Hard thresholding (b) Soft thresholding	52
3.3	(a) Original Image (b) Corrupted by Gaussian noise (c) Denoised by VisuShrink (d) Denoised by SUREshrink (e) Denoised by BayesShrink	56
3.4	(a) Histogram of the high-band wavelet coefficients of gel Image (b) Blue line: histogram of the same coefficients scaled by estimated local standard deviations. Red line: unit-variance, zero-mean Gaussian pdf	58
3.5	A 2DGE image from database [1]	59
3.6	(a) Block diagram of the denoising algorithm (b) Histogram of the estimated local variance of the coefficients(solid line) in wavelet image sub-band, approximated using a single exponential prior (dash-dotted line) and a mixture of exponentials that consists of three single exponentials in three non-overlapping regions (dashed line)	60
3.7	Histograms of Quincunx wavelet coefficients of various sub-bands of the 2DGE image in Figure 3.7 (a) Level-1 Scale-1 (b) Level-1 Scale-2 (c) level-2 Scale-1(d) Level-2 Scale-2	63
3.8	(a) Clean synthetic image (b) Noisy image-1( $\sigma=30$ ) (c) Noisy image-2 ( $\sigma=35$ ) (d) Noisy image-3( $\sigma=40$ )	64
3.9	Denoised Synthetic Images using (a) CWT with BayesShrink (b) Quincunx with BayesShrink (c) Coif5 with Bayes shrink (d) Db8 with BayesShrink (e) Statistical Model on Quincunx coefficients with 7x7 window (MAP rule) (f) Statistical Model on db8 coefficients with 7x7 window(MAP rule)	70
3.10	3D view of synthetic images.	71
3.11	De-noised images are processed through Delta 2D package. Segmented images are shown. (a) image denoised by coiflet and processed. Total 412 spots are detected out of 457 true spots. (b) image denoised by quincunx and processed. Total 446 spots are detected out of 457 true spots.	71
4.1	Block diagram of proposed segmentation approach	80
4.2	Segmented Spots	81
4.3	A part of gel image showing some missing spots and false spots using Delta2D and using the proposed method	81
4.4	The histogram of the wavelet coefficients is plotted along with a Gaussian curve for comparison and measurement of DP values	85
4.5	The pdf of IDI and two threshold levels T1 and T2	88
4.6	A real 2D gel image with protein spots (left) and corresponding IDI values (right). The dark colors indicate low values and bright colors indicate high values	88

4.7	The tricolor image of IDI values of the protein spots (right) with corresponding original image (left). Black colors indicates interiors ( $IDI < T1$ ), white color indicates edges ( $IDI > T2$ ) and gray color indicates background ( $T1 < IDI < T2$ ).	89
4.8	The oversaturated spots (left) and corresponding IDI values (right). In right image, bright color indicates high IDI values	90
4.9	(a) The edge information from IDI ( $IDI > T2$ ) is overlaid on the corresponding part of the real gel image. (b) The interior information ( $IDI < T1$ ) is overlaid on the same part of the real gel image	90
4.10	(a) An original 2D gel image with (b) its ITP, (c) its binary image made by $ITP \geq 0.02$ and (d) its binary image obtained using global 2D Otsu threshold on gray value image	93
4.11	(a) A 2D gel image. (b), (c) and (d) its binary images obtained through applying different gray value thresholds (b) 100 (c) 75 and (d) 25 respectively	94
4.12	3D profile of ITP of a typical faint spot	94
4.13	(a) An oversaturated spot with multiple regional maxima of ITP on its boundary. (b) The segmentation of the overlapped oversaturated spots	97
4.14	Effect of different values of $ITP_{MIN}$ on the segmentation result of a real gel image. (a) $ITP_{MIN} = 1\%$ (b) $ITP_{MIN} = 2\%$ (c) $ITP_{MIN} = 5\%$ and (d) $ITP_{MIN} = 10\%$ . Spots identified as oversaturated spots are depicted with green border and the rest of spots are depicted with pink border	103
4.15	(a) a real gel image from public dataset [77] and segmentation results using (b) Proposed method (c) ImageMaster 7 and (d) SCIMO	104
4.16	A part of the image and results shown in Figure 5.15(b, c, d) is selected and zoomed for better visibility. (a) Result by Proposed method (b) Result by ImageMaster 7 and (c) Result by SCIMO	105
4.17	(a) A synthetic image and its segmentation using (b) Proposed method (c) ImageMaster 7 and (d) SCIMO	106
4.18	(a) A synthetic image and its segmentation results using (b) Proposed method (c) ImageMaster 7 and (d) SCIMO	107
4.19	Mean error in spot area overlap between the segmentation method and ground truth. The error bar indicates the standard deviation of the corresponding measure (%) across images in dataset	109
4.20	Effect of different amounts of Gaussian noise on the segmentation results of the methods.	110
5.1	(a) A synthetic image of flat objects. (b) A synthetic 2D Gaussian blob image. (c) A noise free synthetic dark flat top Gaussian blob image	114
5.2	Hessian Analysis of a noise free and noisy synthetic image at different scales: $\sigma=2$ (first row) and $\sigma = 6$ (second row). (a) Noise free image at specified resolution (b) Hessian minima (regions satisfying condition: $det(H(x,y; \sigma)) > 0$ and $trace(H(x,y; \sigma)) > 0$ ) for noise free image (c) positive Hessian trace (regions satisfying condition: $trace(H(x,y; \sigma)) > 0$ ) for noise free image (d) Hessian minima for noisy image (e)	118

	positive Hessian trace for noisy image	
5.3	Blob regions obtained using Hessian Analysis at different scales for the noise free and noisy synthetic image. The region of each blob is obtained at its corresponding scale by searching in the scale range of $\sigma = 2$ to $\sigma = 16$ in step of 0.5. (a) Original noise free synthetic image and (b) blob regions obtained for noise free image (c) noisy synthetic image and (d) blob regions obtained for noisy image	118
5.4	Lifting scheme for undecimated quincunx wavelet: (a) analysis and (b) synthesis. Predict (P) and update (U) filters are upsampled by dilation matrix $\mathbf{D}$ . $\mathbf{I}_1$ and $\mathbf{D}_1$ represents the approximation and detail part of the next scale and $\hat{\mathbf{I}}$ represents the reconstructed image. $P_2$ and $U_2$ denotes the second order filters are used [70]	120
5.5	Effect of selection of kernel bandwidth on the obtained binary region. (a) Original synthetic images and obtained binary regions using proposed method at following kernel bandwidths: (b) $h = 1$ (c) $h = 6$ and (d) $h = 10$	124
5.6	Pseudo code of the Region Refinement method	127
5.7	Pseudo code for separation of overlapped spots in 2D gel image	128
5.8	(a) Protein spots from original image and separation of overlapped spots after segmentation, using (b) Euclidian distance, (c) regional minima and (d) proposed approach	129
5.9	Effect of the parameter $R_N$ on the final segmentation. (a) A 2D gel image and (b)-(e) segmented results using our method when $R_N$ was set to 2, 5, 10 and 15 respectively. As value of $R_N$ increases, region of blobs spreads out and may merge nearby blobs. It leads to more global segmentation. (f) Segmentation by a global method – active contour [7]	133
5.10	Plot of kernel bandwidth ( $h$ ) vs. average segmentation accuracy SA (%) for six synthetic images. Images are corrupted with Gaussian noise (with a standard deviation between 1 and 5) and salt and pepper (1%-3%). Solid line represents average SA for all mages	134
5.11	Original synthetic/ real images (first row) and segmentation results obtained using proposed approach ( second row)	135
5.12	(a) A synthetic image consisting 2D Gaussian blobs and its segmentation results using (b) the proposed approach, (c) watershed method, (d) Otsu's threshold, (e) Delta2D and (f) ImageMaster 7	137
5.13	Boundaries of the spots are assumed at a distance of two standard deviations from their center	137
5.14	Comparison of different segmentation methods for synthetic Gaussian blob images. (a) The segmented spot regions are evaluated using the terms JD and SA. (b) The number of segmented spots is evaluated as fraction of the total number of true spots in ground truth	139
5.15	(a) Real 2D gel sub-image and segmentation results using (b) proposed approach, (c) watershed, (d) Otsu's threshold, (e) Delta2D and (f) ImageMaster 7	140
5.16	(a) Real 2D gel sub-image and segmentation results using (b) proposed approach,	141

	(c) watershed, (d) Otsu's threshold, (e) Delta2D and (f) ImageMaster 7	
5.17	Segmentation errors for the image of Fig. 5.21(a) with different methods. The horizontal axis represents the standard deviation of Gaussian noise in the image	145
5.18	Comparison with other state-of-the-art methods	146
5.19	First Row: CV method on synthetic and real 2D gel images. Second Row: KWFCM method on the same synthetic and real 2D gel images	147
5.20	(a) An image from the public database and its segmentation using (b) our approach (c) CV and (d) KWFCM	147

## List of Tables

Table 1.1 Proposed segmentation methods.....	20
Table 3.1 Mean PSNR values for our set of synthetic images with noise variance 40 .....	66
Table 3.2 Mean PSNR values for our set of synthetic images with noise variance 35 .....	67
Table 3.3 Mean PSNR values for our set of synthetic images with noise variance 30 .....	68
Table 3.4 Comparison of denoising methods for synthetic images.....	69
Table 4.1 Results in terms of 'spot efficiency' .....	82
Table 5.1 Detailed result on synthetic image .....	143

# Chapter 1 Introduction

## 1.1 Motivation

Proteomics is the field which involves study of multi-protein systems, focusing on the interplay of multiple proteins as functional components in a biological system. Two-dimensional gel electrophoresis (2DGE) is an important and the most widely used technique of analyzing protein expression in this field. By this technique, a very large number of proteins can easily and simultaneously be separated, identified and characterized. The detailed study of proteins in this manner is very useful to analyze earlier protein databases and compare them against the new proteins which are responsible for making new biomarkers, which helps in diagnosing specific diseases like cancer. Separating thousands of protein spots is a very tedious and laborious job. Protein spots are highly irregular in terms of their shape, size and intensity, which make their automated detection very challenging. Hence, a completely automated system for the analysis of 2DGE images is increasingly in demand.

We have developed the “Spot Picker Robot”, which automates the excision of the protein spots from 2D gels (up to a size format of 220 mm x 240 mm) obtained from electrophoresis process for screening of a large number of proteins. Spots can be picked from fluorescent, coomassie blue or silver stained gels. The spot picker system is capable of imaging as well as direct picking of protein spots with the help of a 3-axes robotic system.

It is a very challenging task to find out the correct position coordinates of all the proteins in a 2D gel because proteins change their position in each experiment, according to their mass and charge and also contain a large amount of noise and non-uniform background. The precise

excision of correct protein spots is crucial for further analysis. After processing the gel image, the system generates the spot position coordinates and spot picking list, which are the reference coordinates of each dynamic protein spot, this is then directly interfaced with the robotic system for automated protein spot excision. Detection and interpretation of protein spots depend on the accuracy and reliability of the image processing methods. In this dissertation, the emphasis has been on proposing solutions to cater the challenges involved in noise removal and protein spot segmentation of 2DGE images.

The thesis describes and proposes solutions to some of the current challenging problems in image analysis of two-dimensional gel electrophoresis (2DGE) images. 2DGE is the leading technique to separate individual protein in plant cells and human cells for drugs and new biomarkers development. This technique results in an image, where the proteins appear as dark spots on a bright background. However, the analysis of these images is time-consuming and requires a large amount of manual work. A lot of commercial software is available which is mostly based on spatial filtering, and hence, none of it is capable of detecting all the true protein spots in 2DGE images. So our main objective is to develop robust and fast methods based on image analysis techniques to detect all the true protein spots, in order to significantly accelerate this technology.

## **1.2 The virtue of Proteomics**

### **Two-Dimensional Gel Electrophoresis in Proteomics**

Proteomics is becoming an increasingly important part of cell biology and it aims to understand the basic principles of life “how the living cell works” [1]. This part of the thesis will give a basic introduction to proteomics, the process of two-dimensional gel electrophoresis for

protein separation and the motivation for applying image analysis in the field of proteomics will be further explained.

Protein is the end product of the gene by transcription and translation of the genome. It is a dynamic entity which has kinematics and functionality. Due to the distinctive properties of specific proteins, researchers can find the exact function of various human cells.

In proteome analysis, two-dimensional gel electrophoresis is a high-resolution technique which is capable of separating thousands of proteins from the human cell or plant tissue on a gel. It is a technique to analyze proteins by mass spectrometry for each spot and it is used in differential analysis of several proteins. Image resulting from this analysis/technique is captured as digital images by an imaging system mounted on a 3-axes robotic system [2]. This image is then analyzed in order to quantitate the relative amount of each of the proteins in the sample in question or to compare the sample with other samples or with a database. After image analysis, the system generates the centroid of each protein spot in the image plane and generates the pick list in the robotic plane. The robotic system has to provide automation for the screening of a large number of proteins and transfer all proteins selected by the user into well plates. Finally, protein analysis is done by mass spectrometry for each protein present in the well plates. The typical flow of gel-based proteomics is depicted in Figure 1.1.

A gel image contains few hundreds to few thousands of spots of varying size and intensities in an inhomogeneous background. The task of analyzing the images can be tedious and subjective, (dependent on the human operator) if performed manually. The use of digital image analysis in the field of proteomics is primarily motivated by the need to improve speed and consistency in the analysis of 2DGE images. The most important issues and challenges related to

digital image analysis of the gel images, namely the de-noising of the images and segmentation of protein spots will be described in subsequent chapters. Knowledge of the basic principles in proteome analysis and gel electrophoresis provides a good background to understand the issues related to the image analysis part of the process which is the main focus of this thesis.

A short definition of proteome analysis is identification, separation, and quantification of proteins. The first publication of the word proteome was in 1995 by Wasinger et al. Wilkins [1] defines the concept of proteome analysis as *“The analysis of the entire Protein complement expressed by a genome, or by a cell or tissue type”*. In other words, a proteome is the complete set of proteins that is expressed by the genome at a given time point and under given conditions in the cell.

## **Biological Applications**

Proteome analysis has a number of biological applications; examples include [1]

- Understanding of the basic principles of life
- Relating the genome and the environment to the organism’s phenotype
- Drug development/evaluation (including toxicology and mechanism of action)
- Disease prognosis, diagnosis, screening, monitoring of e.g., diabetes, all types of cancer, cardiovascular, and much more
- Identification of new drug or vaccine targets
- Improvement of food quality
- Monitoring environmental pollution, and
- Prevention of microorganism/parasite infections

For instance, in drug development, pharmaceutical companies spend large amounts of resources in studying the drug effect in animal experiments. Some of these effects can be assessed by measuring changes in protein levels across different tissue samples.

### **Two-dimensional Gel electrophoresis Process**

2DGE enables separation of mixtures of proteins due to differences in their isoelectric points (pI), in the first dimension, and subsequently by their molecular weight (MWt) in the second dimension.

A gradient of pH is applied to the electrophoresis gel, and an electric field is applied across the gel, making one end more positive than the other. Naturally, at all pHs other than their isoelectric point, proteins will be charged. If they are positively charged, they are pulled towards the most negative end of the gel and if they are negatively charged they will be pulled towards the most positive end of the gel. The proteins in the first dimension will move along the gel and will accumulate at their isoelectric point; that is, the point at which the overall charge on the protein is zero (a neutral charge). The Laboratory process is shown in Figure 1.1. A typical one-dimensional and two-dimensional gel image is shown in Figure 1.2 and Figure 1.3 respectively.

The main advantage of this technique is that it enables, from very small amounts of material, the simultaneous investigation of the protein expression for thousands of proteins. After protein separation as described above, an image of the protein spots is generated for accurate segmentation and subsequent correct matching of the protein spot patterns. This allows not only for the comparison of two or more samples, but furthermore, makes the creation of a 2DGE image database possible.

Even though promising attempts have been made to make the technique as reproducible as possible, there are still differences in protein spot patterns from run to run. Also, due to improvements in the composition of the chemicals used to extract as many proteins as possible, the patterns become so dense that locating the individual protein spots is a non-trivial task.

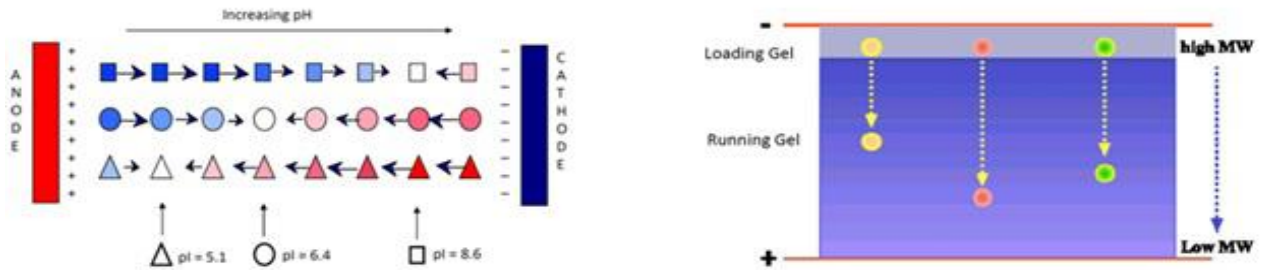
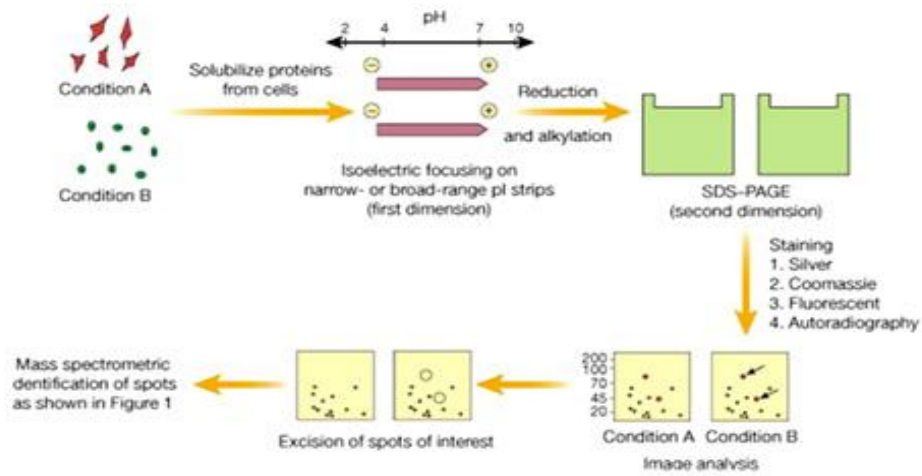


Figure 1.1: Laboratory process of making of 2DGE image,

Courtesy: CPA( Centre for protein analysis)

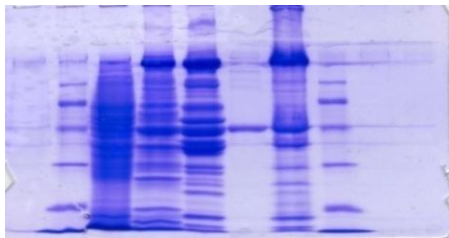


Figure 1.2: 1D gel image

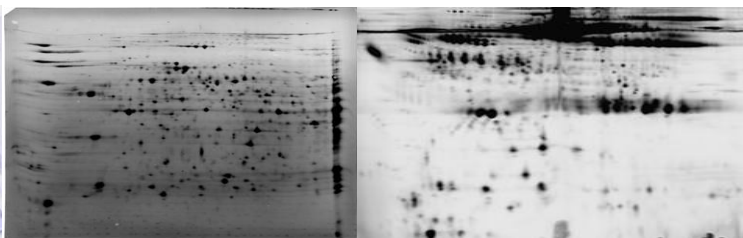


Figure 1.3: 2D gel images

## **1.3 Spot Picker Robot**

The Spot Picker Robot [2] can be seen as an essential tool in proteomics. It is a 3-axes robotic system as shown in Figure 1.4, that we have designed for precise protein spot identification, excision and to accurately pick spots from 2D gel electrophoresis (2DGE). It transfers the picked protein into well plates for analyzing protein expression and helps in discovering new proteins to develop biomarkers for new diagnostic tests. It provides the necessary automation for high throughput analysis. Design and development of such system poses challenges, such as the need for uniform illumination, precise spot excision and accurate imaging algorithms. The Spot picker robot designed by us features novel nonseparable wavelet based imaging algorithms and an improved light illumination system for detection of faint, irregular and overexposed protein spots in a non-uniform background. The system includes a high performance solenoid controlled surgical grade protein spot excision tool and a novel wavelet based accurate positioning algorithm to reduce the effect of jerks on the system [2]. These challenges have been discussed briefly in subsequent sections. Post that, this thesis addresses the most challenging problem – image analysis of 2DGE images and discusses it in detail. 2D Gel based proteomics flow is depicted in Figure 1.5.

### **1.3.1 Illumination System**

We have implemented a novel hardware feature for illumination in our system. Uniform non-heating illumination is an important requirement for imaging the protein spots without any distortion of the gel or denaturing of proteins. A light source as shown in Figure 1.6 has been designed and developed which consists of arrays of LEDs and provides 90% color index rendering along with 100% diffused pure white light with low power consumption.

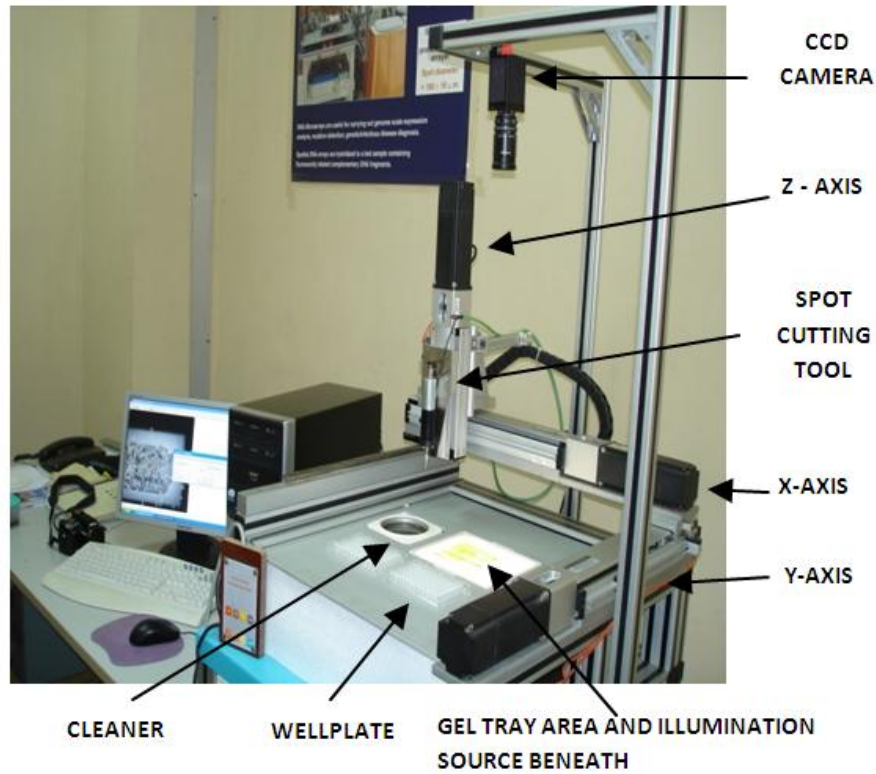


Figure 1.4: Spot Picker Robot

1. Sample preparation from cell/tissue
2. Separation of protein in sample by Electrophoresis
3. Image Acquisition: High resolution color CCD camera
4. 2D Gel Image Analysis :
  - a. Image Preprocessing (De-noising)
  - b. Segmentation (Spot detection)
  - c. Image Registration
  - d. Protein Quantification in spot (shape, size, intensity, contrast)
5. Spot Picking Robot for Automation: A 3-axes robot for picking the protein spots from 2D gel surface
6. Protein spot cutting tool
7. Data Analysis and Integration
8. The excised protein is identified by Mass Spectroscopy

Figure 1.5: Typical flow of gel-based proteomics

### 1.3.2 Spot Cutting Tool

Excision of individual protein spots from a 2D electrophoresis gel without deformation is another important task. We have developed a cutting tool, as shown in Figure 1.7, made of surgical grade stainless steel with a diamond coated surface. It is designed to minimize carry over or damage to the gel or membrane when properly handled. A solenoid based pneumatic actuated displacement system with silicon diaphragm is used to create pressure inside the cutting tool to expel the gel from the tip into the well plate. It provides fast and accurate pick and place of the protein spot.



Figure 1.6: Illumination Source



Figure 1.7: Spot Cutting Tool

### 1.3.3 Robotic System

The spot picker robot is a critical part for precise picking of the protein spots from 2D gels and to transfer picked proteins into the well plate for further analysis. Hence the system hardware consisting of a 3-axes robotic motion has been designed to be highly precise with a positioning accuracy of  $\pm 10$  microns as measured from the axis movement as well as from the spot locations. This can be achieved with the help of servomotors, high-resolution encoders, precision ground ball-screw based linear actuator, an advanced control system scheme and a well damped table. A control block diagram of the whole system is represented in Figure 1.8.

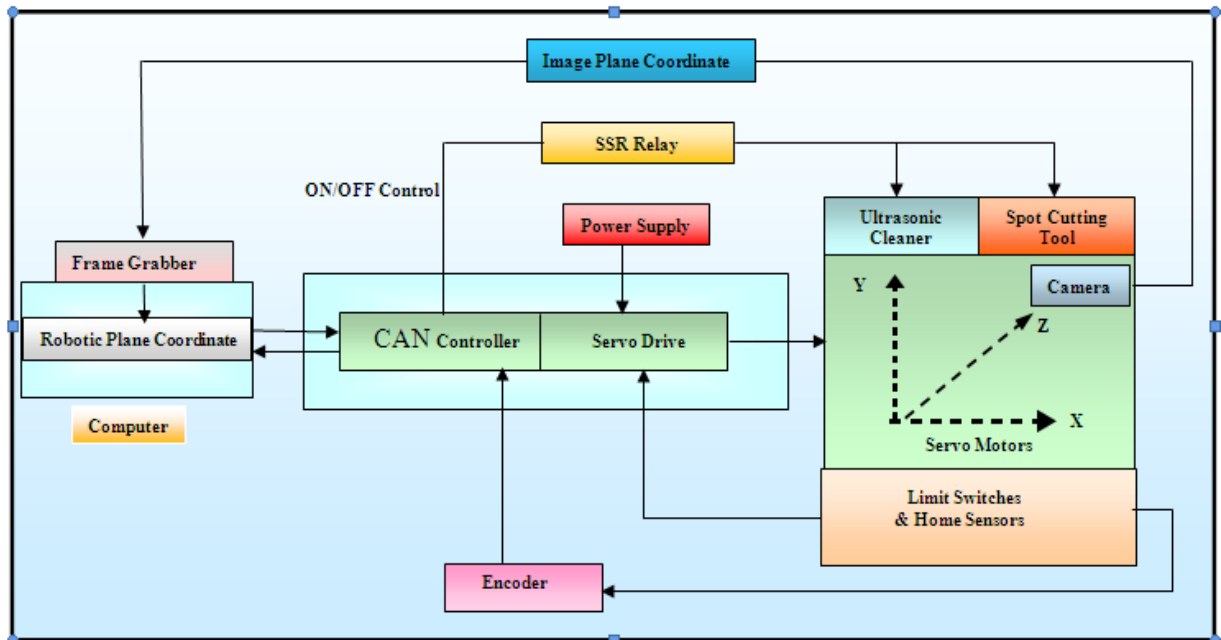


Figure 1.8: Computer based control system for Spot Picker Robot

### 1.3.4 Control System and Software

All axes are interfaced with servomotors along with an encoder and linear actuators. All motors are interfaced with servo drives and all three drives are connected to the CAN network. The communication of all the drives connected to the CAN bus network have been set-up through an RS-232 link between a PC and one of the drives. CAN open protocol is used for setting up the drives for motion control parameters and communication between the drives. Optical limit switches are provided for each axis and interfaced with I/O of the servo drive. The Ultrasonic and spot cutting tools are interfaced with solid state relay and controlled through the digital output of a controller.

A realistic servo dynamic model of the system is constructed; various control loop compensators are used to achieve a fast response and less oscillation in the system. The position and speed loop compensators are implemented as software based lead, lag compensators and

notch filters. Depending on the bandwidth requirements, different loops may cycle at different rates and be tuned for a stable system.

Object oriented multithreading software has been developed to provide real time and user friendly control for each resource of the system. It grabs the image, analyzes it and presents the segmented result of protein spots to the user for automated or manual picking of the spots. The centroid coordinates of spots in the image plane are transformed into the robotic plane and the robot cuts, picks and delivers the spots. After cleaning the cutting tip, the robot picks the next spot and the cycle continues to reach the final spot.

Sample outputs coming from our system are shown in Figure 1.9. One can clearly see the superior quality of the output of the spot picker robot.

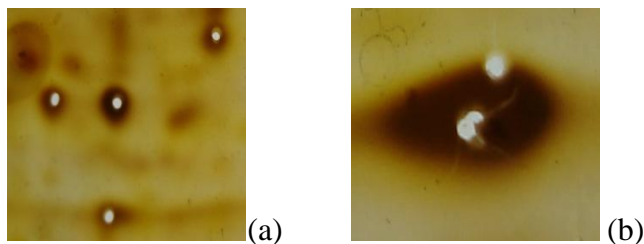


Figure 1.9: Spot cut from the gel (a) by Spot Picker Robot (b) by manual operation

### 1.3.5 Image Analysis of 2DGE Images

In order to detect protein spots accurately, the 2D gel image is scanned through a highly sensitive CCD camera. The set of image processing tasks is pipelined in the following stages.

- Image Preprocessing- Denoising and background correction
- Image segmentation-In this step, image is segmented into two parts, foreground, and background and followed by detection of spot and separation of overlapping spots

- Feature extraction and spot filtering-Artifacts and streak removal
- Image Registration
- Quantification of spots

In this thesis, we have focused on denoising and segmentation of gel images. The problems that occur in 2DGE images pose challenges in accurate image denoising and segmentation of the images. These are discussed in great detail in this thesis.

### 1.3.5.1 Problems in Image Processing of 2DGE Images

Due to practical limitations such as the system nonlinearities in 2DGE process and image acquisition, many streaks and multiple overlapped protein spots appear in the gel image. A gel image contains a few hundreds to a few thousands of spots of varying size and intensities in a non-uniform background. Some examples of various kinds of protein spots are shown in Figure 1.10. The presence of faint spots, spots in exposed background, streaks, artifacts, overlapped and saturated spots makes the segmentation task extremely difficult [3] [4] [5].

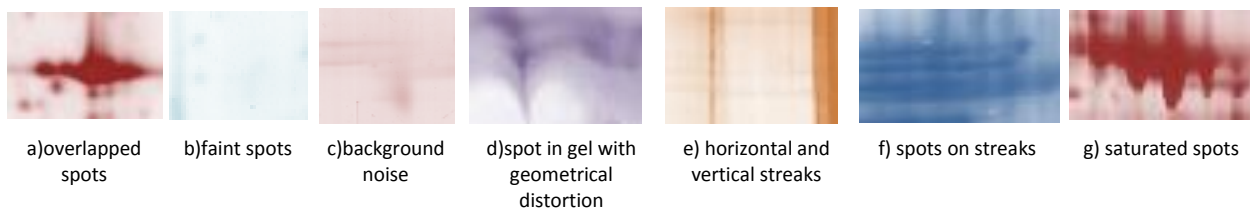


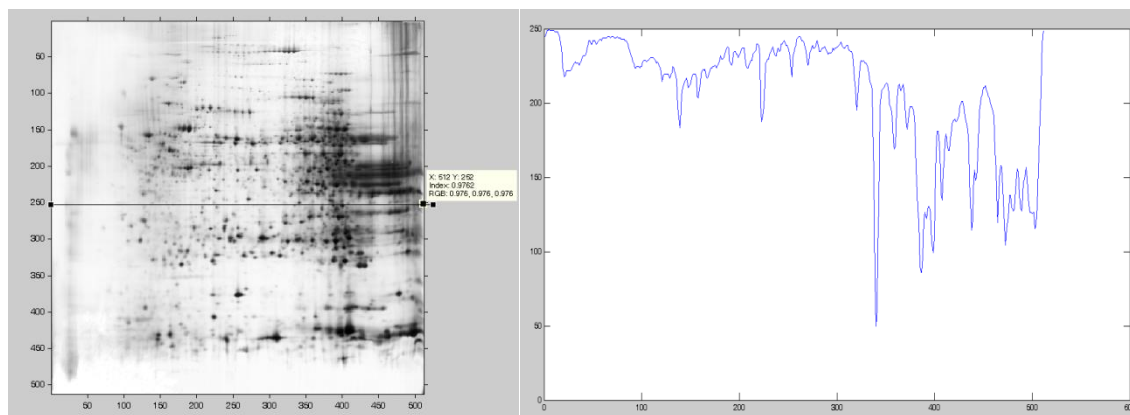
Figure 1.10: Different types of protein spots

### 1.3.5.2 Problems in Denoising

It is well known that 2DGE images are inherently noisy due to the nonlinear electrophoresis process, the gel's susceptibility to dust and the imperfect image acquisition process. Due to

inherent non-linear background variation, denoising of the 2DGE images is a non-trivial task.

Figure 1.11 shows a line profile of a gel image.



(a)

(b)

Figure 1.11: (a) A typical 2DGE image with varying background (b) Intensity line profile

Most commercial software use spatial filtering to attenuate noise from the image, which works on raw intensity value. The Spatial filter replaces the original gray value with a weighted average/median of the neighborhood. This leads to a change in the original intensity value of the spot and also produces distortion in the edges.

Collective individual pixel statistics of protein spots in space are not constant, so it is very difficult to distinguish the signal from noise in space or frequency domain separately. The Wavelet transform is a good tool to distinguish the signal from noise in both space and frequency domain as it outperforms spatial filtering. It provides coarse and fine variations separately, i.e., it can give a better signal to noise ratio and reduced edge distortion. Traditional Wavelet basis functions capture discontinuities at edge points but will not see the smoothness along the edges. They cannot capture the complete geometrical information of the images due to limited

directionality (horizontal, vertical, and diagonal) as this approach is a separable extension of 1D methods.

The denoising methods based on nonseparable wavelets, which take into account all these considerations, namely nonuniform background, visual distortions, preservation of weak edges and artifacts, will be suitable for our purpose.

### 1.3.5.3 Problems in Segmentation

The segmentation of 2DGE images is the process of extracting true protein spots from the inhomogeneous background. A gel image contains a hundred to thousand spots of various shapes, sizes and intensities. Large variations in intensities pose challenges in the segmentation of the protein spots. In typical 2D gel images, foreground and background are both heterogeneous and share nearly the same statistical model. Intensity histograms of carefully segmented foreground and background regions of 2D gel images exhibit a long range of overlapping gray values. The histogram in Figure 1.12 shows the skewed distribution of the protein spots and the background.

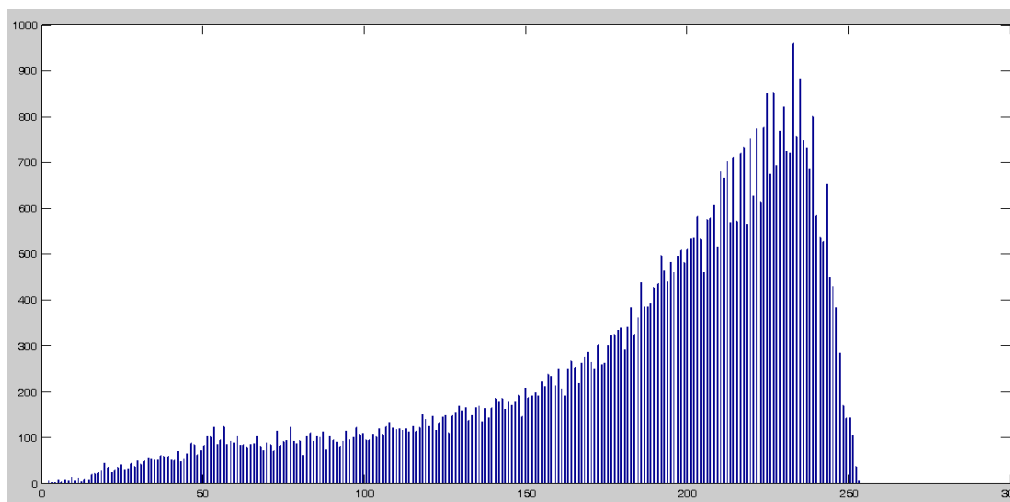


Figure 1.12: a) Foreground intensity histogram (range covered 0-253)

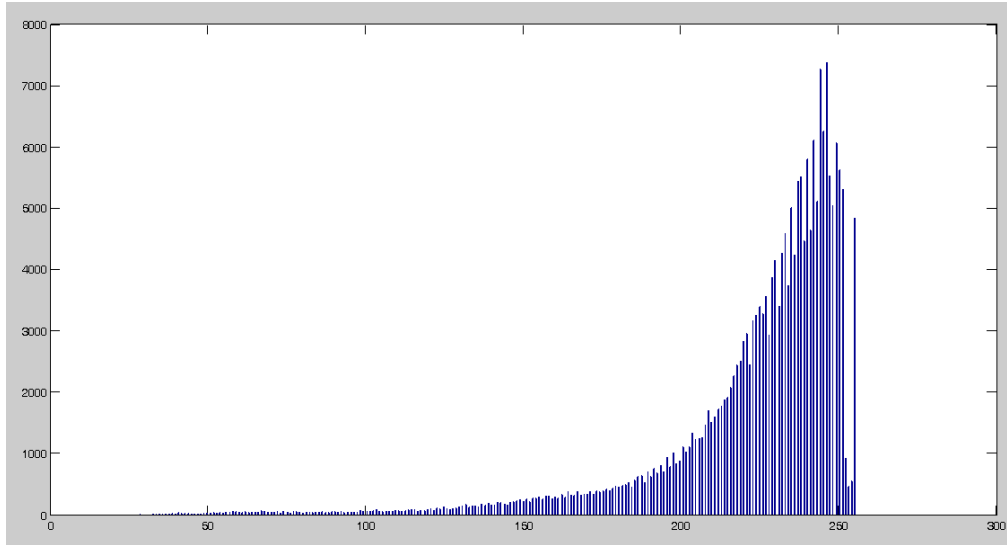


Figure 1.12: b) Background intensity histogram (range covered 20-255)

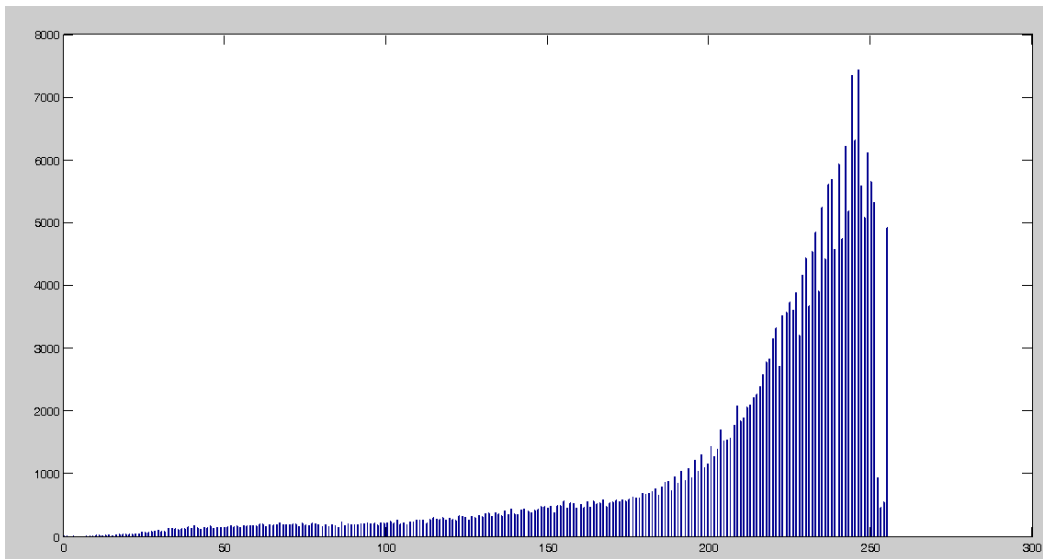


Figure 1.12: c) Gel image histogram

Low amounts of proteins results into a faint spot in the gel images. Due to indistinct edges and a low contrast with the background, faint spots are difficult to analyze and segment, since they may get lost in the background. If we try to avoid losing these faint spots, a lot of extraneous spots are detected.

During the electrophoresis process, the motion of a stained protein sometimes generates horizontal and vertical streaks. These streaks pose a big challenge in spot detection, as they may overlap one or more spots or can themselves be detected as spots.

To summarize, the major challenges in the segmentation of gel images are:

- Intensity inhomogeneity in background and foreground
- Faint spots with indistinct edges
- Horizontal and vertical streaks
- Overlapping spots
- Saturated spots (protein abundant spots)

The state-of-the-art methods available in the literature fail to give an accurate segmentation. Complex and saturated spots cannot be accurately modeled by a Gaussian or any other similar function.

## **1.4 Literature for 2DGE Images Analysis**

A gel image contains spots of varying intensities in the inhomogeneous background with many streaks. P.Cutler et al. developed methods [6] to capture spots of varying intensities, using a serial analysis of the image through a range of gray value density levels. It does not incorporate spatial correlation information and thus fails to distinguish between a spot and noise. Due to a large overlap between foreground and background gray values, researchers are inclined to use local intensity features. Methods [7] based on local features provide better results, but are still insufficient to distinguish between artifacts and spots. The watershed [9] is a good method to divide the image into local homogeneous regions and is extensively used for gel image segmentation by many researchers. Watershed methods result in over segmentation and thus

require post-processing. Kim [10] et al. addresses this issue by combining the idea of hierarchical thresholds with the watershed, but their approach usually misses many faint spots. A.dos Anjos [12] et al. utilized the difference between local variances of foreground and background to identify spots in each watershed basin. It removes most of the background regions, but there is still a tradeoff between detection of faint spots and background removal. All above methods available in the literature assume that the spot lie at the regional minima of the image. To distinguish from the background minima, regional minima are searched in a larger sub-region. Mylona et al. [11] simplified the spot detection method by searching only for the spot center at the regional extreme in a circular sub-region. This method is able to detect the spots on a streak. To avoid the detection of a false center, global thresholds are used, which fail to cope with nonlinearity in the image. Savelonas et al. [8] applied contrast limited adaptive histogram equalization to enhance the faint spots. They also applied active contour methods in a local sub-region to find out the accurate boundaries of the protein spots in the noisy and inhomogeneous background. The method is parametric and requires proper tuning of parameters. It is unable to separate out the overlapping spots and also misses some faint spots. Recently Kostopoulou et al. [13] utilized the 2D OTSU threshold technique in a recursive manner to extract the region of the spots, including faint spots. This method uses two different thresholds to distinguish between artifacts and spots. These two thresholds are a percentage of the local maxima inside the spot and the coefficient of variation. Due to statistical similarities between faint spots and artifacts, this method fails to provide a good tradeoff. To improve the situation, contrast enhancement techniques and background elimination techniques [15]-[17] are also used as a preprocessing step, but such techniques do not take care of the spot morphology and thus, they may cause several faint spots to go undetected. The parametric modeling of the spots has been explored

[18]-[21] for the further refinement of the results. Since one gel image may contain hundreds to thousands of spots, the parametric modeling increases the time complexity of the segmentation method and also fails to represent all spots in the gel image.

Many researchers are dependent on the commercial software packages such as ImageMaster 7 (Geneva Bioinformatics/ GE Healthcare) [22] and Delta2D (Decodon) [23] for gel image analysis. The output of these software packages is very much dependent upon the selection of the thresholds. Researchers first try to find out a good set of thresholds for individual gel images and then they invest many hours modifying the results by manual editing, so that false spots can be eliminated and undetected true spots can be added. This is a very laborious, time-consuming and error-prone process. The faint spots, artifacts, overlapping spots and the streaks are big challenges for these state-of-the-art methods and further investigation in this field is needed.

## **1.5 Problems Addressed in This Thesis**

In this thesis, we focus on denoising and segmentation of 2DGE images. These images contain objects of varying intensity in an inhomogeneous background. There are several methods available in the literature for denoising and segmentation of inhomogeneous images. Preservation of weak edges in denoising methods is necessary and has not been addressed up to satisfactory levels. The nonseparable wavelet can capture the multi-directional singularity of the spots including faint spots. The method based on nonseparable wavelets can perform better in terms of preservation of weak edges.

Despite all the research activity in the segmentation of 2DGE images as mentioned in section 1.4, there are open issues that are not adequately addressed. All the methods assume the spots lie on regional minima; therefore they miss some spots which are not on regional minima.

Sometimes a single spot also contains more than one regional minimum and it results in over segmentation of the spot. The available methods usually take a large sub-region to filter the regional minima. Since there are spots of varying sizes, this approach is still not sufficient. These issues need to be satisfactorily resolved.

### **1.5.1 Contribution of This Thesis**

Main contributions of this thesis are as follows:

- We present a method for denoising 2D Gel images, which is based on nonseparable wavelets which preserve the faint edges along with smoothing the background area. We have used the quincunx wavelet and found it to give better results than separable wavelets [24]. We discuss this proposed denoising approach in Chapter 3.
- The watershed transform is a useful tool in dividing the image into local homogeneous regions, but exhibits over segmentation. The wavelet transform is useful in capturing singularities. We have employed both transforms to study singularities in local homogeneous regions. This approach is efficient to find spots in each local region and it also tackles over segmentation [25]. This method is discussed in detail in Chapter 4.
- Methods which identify regional minima as spots, such as the watershed approach, usually miss the small sized faint spots either not occurring on regional minima or containing multiple noisy regional minima, so detection of faint spots is also a difficult task. This thesis presents the second novel segmentation method to observe the nature of faint spots in the inter-scale ratio of quincunx wavelet coefficients framework and extracts the regions of faint small spots. This characterization enables us to detect the spots, independent of their intensity. The advantage of this characterization is that it does

not depend on the regional minima of the image [80]. This method is discussed in detail in Chapter 4.

- The need for a large number of decompositions for large sized spots leads to an increase in the computational complexity for high-resolution images. Based upon observation and analysis performed in above two cases, we present a more versatile third novel segmentation method [81] to cope with the noisy and in-homogenous background. For complete characterization of all types of spots, we have incorporated kernel density estimation (KDE) technique in the nonseparable wavelet domain. The result is fewer artifacts, less number of missing spots and more accurate segmentation. This method is discussed in detail in Chapter 5.

**A brief about these proposed segmentation methods and their applicability are tabulated as:**

**Table 1.1 Proposed segmentation methods**

	<b>Challenges to address</b>	<b>Suitable images for best case</b>	<b>Method applicable</b>	<b>Remarks and difficulties of method</b>
1.	Streaks	Fast segmentation for low-resolution 2D gel images having spots with distinct boundaries	Proposed watershed based segmentation method discussed in Chapter 4 [25].	Manual selection of global threshold for each image separately
2.	Segmentation of faint spots	2D gel images with many faint spots or spots in overexposed background	Wavelet inter-scale ratio based proposed method discussed in	No. of scales increase with the size of spots and thus increase computational complexity

			Chapter 4[80].	
3	Reduction of artifacts Segmentation of all types of spots Separation of overlapped spots	Any 2D gel images or any noisy images containing several blob objects	Wavelet and KDE based proposed method discussed in Chapter 5[81].	Performance may be slightly improved by incorporating elliptical fitting for separation of overlapped spots at the cost of computational complexities

## Chapter 2 Multi-Scale Processing and Nonseparable Wavelets

### 2.1 Introduction

The wavelet transform has allowed scientists and engineers to analyze the time varying and transient phenomena of a signal. The Continuous Wavelet Transform (CWT) is used to measure the similarity between the signal and the analyzing wavelet function. The CWT represents the signal in terms of translated and dilated versions of the mother wavelet. The discrete version of CWT is called Discrete Wavelet Transform (DWT). A dyadic sampling of the time-frequency plane results in a very efficient algorithm for calculating the DWT. Dyadic Multiresolution Analysis (MRA) is one of the techniques which help us study how to analyze functions in the space  $\mathcal{L}^2(\mathbb{R})$  at different scales. The different scales at which the functions are analyzed are powers of 2.

In this chapter, we are going to see how and why wavelets are used in processing data across scales. The axioms of dyadic MRA are briefly discussed in this chapter. We will discuss singularities and noise removal. Noise removal is an important pre-processing step for analyzing any real signal or detecting singularities. We present a brief overview of the different types of noise present in signals.

An image is a 2D signal, whose intensity is a function of two variables (horizontal, vertical coordinates). However, images contain multi-dimensional features such as smooth contour and are not simply stacks of 1D piecewise smooth scan-lines. Discontinuity points (edges) are typically located along smooth curves/contours due to smooth boundaries of physical objects. Thus, natural images contain intrinsic geometrical structures that are key features of visual information. Due to simplicity and low computational complexity, tensor product of 1D wavelet

is used to analyze the images. Because of the anisotropic nature and rectangular sampling support, this formulation captures the singularities in limited directions (horizontal, vertical and diagonal) only.

The multi-dimensional filter banks are preferred over tensor product of 1D wavelet for better frequency selection, better extraction of geometrical and directional features of the images. It involves the mathematical concepts of lattices in the form of sampling. Rectangular sampling results in a separable wavelet which is the extension of the 1D wavelet. It is not considered as an efficient way to sample a multi-dimensional band limited signal. A non-rectangular sampling geometry can represent the band limited signal in efficient way. The nonseparable wavelets using arbitrary sampling lattices provide the advantage of more degrees of freedom and hence allow better design of the filter bank adapted to signal geometry.

The wavelets are implemented using filter banks. The lifting framework provides fast implementation and decomposes the filter banks into a finite sequence of simple filtering steps known as predict and update steps. The decomposition asymptotically reduces the computational complexity of the transform.

## **2.2 Dyadic Multiresolution Analysis (MRA)**

In Dyadic MRA, we study how to analyze functions in space  $\mathcal{L}^2(\mathbb{R})$  at different scales. In dyadic MRA, the scale is discretized by powers of two and the time axis is translated by discrete steps corresponding to the given scale. The basic theory of Dyadic MRA helps in understanding why wavelets are actually used for processing data across scales. So, a different perspective of the axioms of dyadic MRA and the theorem of MRA is presented below. To make it easier to appreciate this, we use Haar MRA as the context of the discussion.

### 2.2.1 Axioms of Dyadic MRA

**1. Ladder Axiom:** The name Ladder axiom is due to the way subspaces are organized. Let  $V_0, V_1, \dots, V_n$  be a ladder of subspaces which belong to  $\mathcal{L}^2(\mathbb{R})$ . Each subspace  $V_i, i \in \mathbb{Z}$  contains functions which are piecewise constant in the intervals  $[2^{-i}l, 2^{-i}(l+1)], l \in \mathbb{Z}$ , then

$$\dots \subset V_{-2} \subset V_{-1} \subset V_0 \subset V_1 \subset V_2 \dots \quad (2.1)$$

Intuitively, a function which is piecewise constant in the intervals  $[2^{-(i+1)}l, 2^{-(i+1)}(l+1)], l \in \mathbb{Z}$  is also piecewise constant in the intervals  $[2^{-i}l, 2^{-i}(l+1)], l \in \mathbb{Z}$ . To span the entire subspace  $V_i$ , a set of linearly independent functions which belong to  $V_i$  are used. They are called the basis functions for  $V_i$ . From the above axiom, we can say that the basis functions of  $V_{i+1}$  can be used to represent the functions in  $V_i$ .

As the above axiom is interpreted, it is observed that as a function in a lower subspace is contracted it becomes a part of the higher subspace and vice versa, as illustrated in the next subsection. It implies that the above subspaces are self-similar in nature. Hence, the basis of the above subspaces is also self-similar. As we see each subspace contains the information of a signal corresponding to that “scale”. This property of a subspace embedded in another subspace is exclusively used for analyzing singularities and self-similar functions. Singularity refers to discontinuity in the signal. This property of singularities propagates through scales. This is because the information obtained at one scale is embedded in another scale. So, a trend is observed at the singular points across each scale. By observing this trend we can detect singularities in the given data. We will discuss singularities in more details in the later sections. The ladder axiom also brings out the fact that the basis of MRA is self-similar in nature, which, in turn, helps out in analyzing the self-similar functions effectively.

**Ladder axiom illustration:**

Figure 2.1 shows functions  $F_0, F_1, F_2$  which belong to subspaces  $V_0, V_1$  and  $V_2$  respectively. Rectangles in the figure show the maximum resolution possible in each subspace (1 in  $V_0$ , 1/2 in  $V_1$  and 1/4 in  $V_2$ ) i.e. the scale of the wavelet function used in them. The values a, b, c, d, e, f and g depend on the signal amplitude. For the functions,  $F_0$  and  $F_1$ , if we put the condition  $b = c$  then  $F_0 \equiv F_1$ . Which means  $F_0$  is a special case of subspace  $V_1$ . Similarly if the condition is  $d = f$  and  $e = g$  then  $F_1 \equiv F_2$ , which means  $F_1$  is a special case of subspace  $V_2$ . Also if  $d = e = f = g$  then  $F_0$  is a special case of subspace  $V_2$ . From the above inferences we can conclude that,  $V_0 \subset V_1 \subset V_2$ , can be extended to the Ladder axiom.

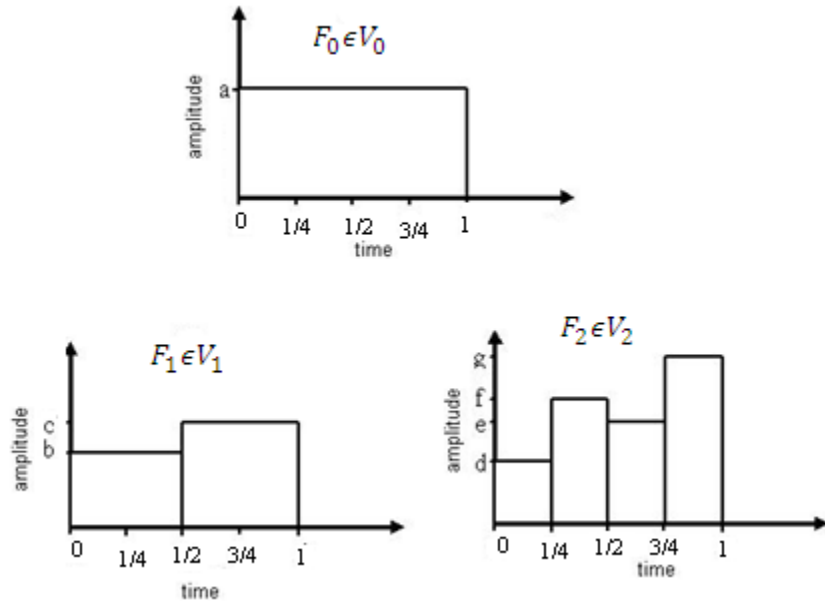


Figure 2.1 Illustration of Ladder Axiom

This axiom combined with other axioms lead us to the Theorem of Multi-resolution Analysis. The result of the theorem of MRA and the above axiom is exploited in many applications in one way or the other.

**2. Axiom of perfect reconstruction:** When a closed union of all the  $V_i$ 's is taken we get the  $\mathcal{L}^2(\mathbb{R})$  space.

$$\overline{\bigcup_{i \in \mathbb{Z}} V_i} = \mathcal{L}^2(\mathbb{R}) \quad (2.2)$$

Intuitively we can say that if we take the union of all the functions which are piecewise constant at different scales of powers of 2, we can go arbitrarily close to a function in  $\mathcal{L}^2(\mathbb{R})$ . This axiom reveals that a function in  $\mathcal{L}^2(\mathbb{R})$  can be reconstructed back almost perfectly if the information across each scale or in each subspace is preserved.

**3.** The intersection of all the subspaces is the trivial subspace  $\{0\}$ . This is because a function cannot have a finite energy and be piecewise constant with an infinite support. This axiom also reveals that a function in  $\mathcal{L}^2(\mathbb{R})$  has significantly less information at scales which have large support and as the length of the time scale reaches infinity, the content of the signal approaches zero. The mathematical equation is given in (2.3).

$$\bigcap_{i \in \mathbb{Z}} V_i = 0 \quad (2.3)$$

**4.** If a function  $x(t) \in V_0$ , then  $x(2^i t) \in V_i$ . Intuitively, we can say that if a function belongs to  $V_0$ , then the time scaled version of the same function belongs to its respective  $V_i$ . This axiom implies that when a function is contracted or expanded by a factor of 2, the function moves into a different subspace in the same ladder.

**5.** Similarly, if  $x(t) \in V_0$ , then  $x(t - n) \in V_0, n \in \mathbb{Z}$ . It can be generalized as, if  $x(t) \in V_i$  then  $x(t - n2^{-i}) \in V_i, n \in \mathbb{Z}$ , i.e., if a function belongs to  $V_i$ , then the same function translated by a discrete step also belongs to  $V_i$ .

**6. Axiom of orthogonal Basis:** There exist a function  $\Phi(t)$  and its integer translates, which form an orthogonal basis for  $V_0$ . Then by using axioms 4 and 5 we can establish the orthogonal basis for the rest of the  $V_i$ 's i.e.,  $\Phi(2^i t)$  and its integer translates form the basis for  $V_i$ . This axiom lays down the basic foundation in decomposing the signal into different scales.

These subspaces can also be thought of as those subspaces which give some approximate information of a function at each time scale. So while we move from one subspace  $V_i$  to the next level of subspace  $V_{i+1}$ , we require some incremental information about the function. The theorem of Multi-resolution analysis helps us to establish results about this incremental information. From the above results we can actually bring out a relation between the ladder of subspaces. From axiom 1 and axiom 6 we can establish the following result:

$$\phi(t) = \sum_{n \in \mathbb{Z}} h(n) \phi(2t - n), \quad h(n) \text{ is a discrete sequence} \quad (2.4)$$

This relation is valid because any function in  $V_0$  can be represented with the basis of  $V_1$ . It can be seen that  $\phi(t)$  can be expressed as a linear combination of its contracted and translated versions  $\phi(2t - i)$ ,  $i \in \mathbb{Z}$ . This property is exhibited by self-similar functions. Hence, the basis of these  $V_i$  sub spaces are self-similar. These basis which are self-similar by themselves, are very useful and efficient in representing self-similar data.

### 2.2.2 Theorem of MRA

Given the axioms of Multi-resolution analysis, there exists a function  $\psi(t) \in \mathcal{L}^2(\mathbb{R})$  and  $\psi(t) \in V_1$  such that  $\{\psi(2^m t - n)\}_{m \in \mathbb{Z}, n \in \mathbb{Z}}$  forms an orthogonal basis for  $\mathcal{L}^2(\mathbb{R})$ .

Proof of this theorem can be referred in [26] [82] [83]. The space spanned by  $\{\psi(2^m t - n)\}_{m \in \mathbb{Z}, n \in \mathbb{Z}}$  is denoted by  $W_m$ . These subspaces can be thought of as incremental subspaces

which give incremental information of a function while moving from one scale to another.

While establishing the proof of this theorem we can form several results. We know that,

$$\overline{\bigcup_{i \in \mathbb{Z}} V_i} = \mathcal{L}^2(\mathbb{R}) \quad (2.5)$$

Also,

$$V_{m+1} = V_m \oplus W_m \quad (2.6)$$

Using Equations (2.5) and (2.6) we can form a chain equation resulting in the following equation.

$$\mathcal{L}^2(\mathbb{R}) = V_0 \oplus (\bigoplus_{n=0}^{\infty} W_n) \quad (2.7)$$

Using the above result any function  $f(t)$  in  $\mathcal{L}^2(\mathbb{R})$  can be represented as follows:

$$f(t) = \sum_{n=0}^{\infty} a_n \phi(t-n) + \sum_{n=0}^{\infty} \sum_{m=0}^{\infty} b_{m,n} \psi(2^m t - n), \quad (2.8)$$

where,  $a_n = \int_{\langle t \rangle} f(t) \phi(t-n) dt$

$$b_{m,n} = 2^{m/2} \int_{\langle t \rangle} f(t) \psi(2^m t - n) dt \quad (2.9)$$

The representation of the signal as shown in equation (2.9) is called the dyadic wavelet transform. The coefficients  $a_n$  and  $b_{m,n}$  provide a lot of information about a signal at a particular scale and at a specific region of time in the frequency band corresponding to that scale. The spectral content of  $\phi(t)$  is concentrated around zero frequency whereas that of  $\psi(t)$  is concentrated around a non-zero frequency between 0 and  $\pi$ . So, the functions  $\phi(t)$  and  $\psi(t)$  are approximately Low Pass and Band Pass functions. Particularly,  $\psi(t)$  at different scales acts as the impulse response of a band-pass filter of different pass band frequencies. So, if we consider a

particular  $b_{m,n}$  it gives information about the signal in the interval  $[n2^{-m}, (n + 1)2^{-m}]$  and information about the spectral content in the pass band frequencies of  $\psi(2^m t)$ . So, when a function is decomposed in the above way, information about that function in a specific region of time and in a particular frequency band corresponding to the given scale is obtained. This is the reason why wavelets have become an efficient tool for processing data across scales. This way of representing data helps in many applications of signal processing including fractals [27] [29].

## 2.3 Singularities and Noise behavior

### 2.3.1 Singularities

A singularity is, in general, a point at which the signal blows up or becomes degenerate in some particular way such as differentiability. Singularities and irregular structures generally carry the most important information in any signal. In 2D signals such as images, irregular structures like sharp changes in intensity provide the contour location and help in recognition. For other signals like electrocardiograms and sound pressure waves, the interesting information lies in the transients like peaks and troughs, all of which constitute singularities. Also, it is equally important to study the irregularities in any signal to study its deviation from ideality to detect several abnormalities. Different types of singularities are shown in Figure 2.2.

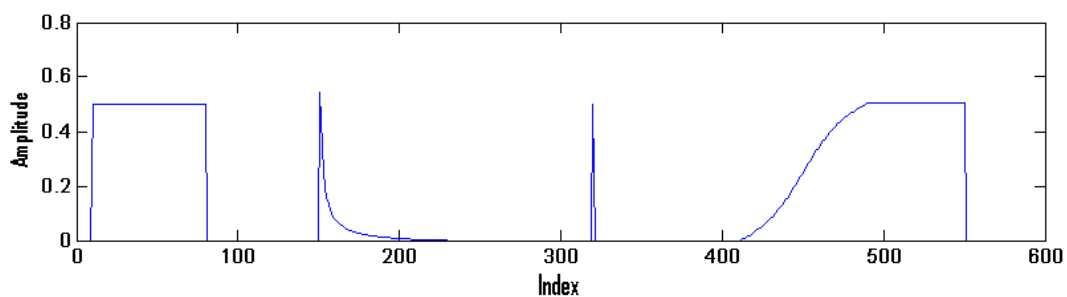


Figure 2.2: Types of Singularities

Before wavelets became an often used signal processing tool, the Fourier transform was the sole mathematical tool available to analyze singularities. The Fourier transform indicates the global overall regularity of a signal but fails to provide the spatial location of the singularity. Due to this constraint, the Short-Time Fourier Transform (STFT) was introduced, which could provide the spatial location of the singularities. The STFT could still not provide a good enough resolution in both time and frequency simultaneously. There had to be a trade-off between time resolution and frequency resolution. The Wavelet transform was a carefully meditated approach to deal with these diverse issues [30]. Wavelet transform breaks the signal into several building blocks, which are well localized in both space and frequency simultaneously.

### **2.3.2 Wavelets in Singularity Detection**

#### **Singularities in a signal without noise**

Stephane Mallat and Wen Liang Hwang explained the notion of singularity detection in a signal by decomposition over a wavelet function, which is the derivative of a zero phase, low pass smoothing function [31]. They further found that the information in a signal is mainly represented by the wavelet transform modulus maxima (WTMM) and can be used to locate the singularities in any signal, whether one-dimensional or two-dimensional. One of the main features of the wavelet transform is that it retains and, in fact, emphasizes the points of singularities in the original signal. To locate these singularities, an appropriate threshold can be applied on the sub-bands. We can get an idea of the WTMM method through the simple example depicted in Figure 2.3.

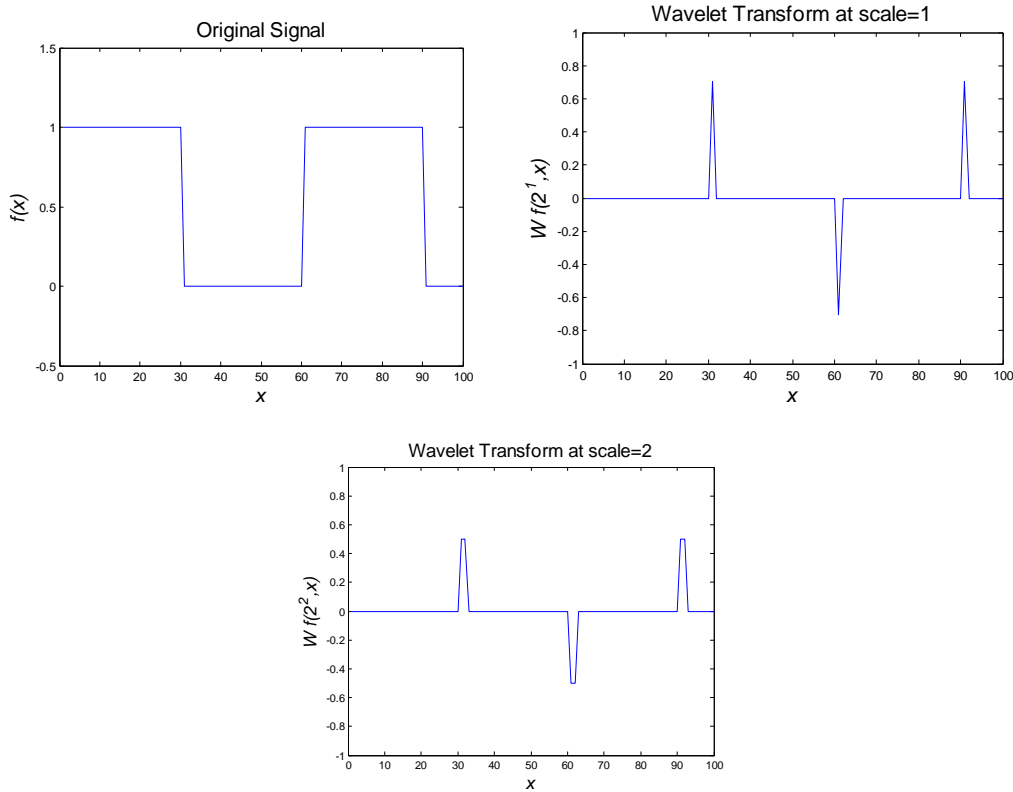


Figure 2.3: Retention of singularities across the scales

In the above example, singularities are located at  $(x=30, 60, 90)$  in the original signal (without noise). It is visible that from Figure 2.3, the locations of these singularities are retained across the scales. If we take modulus maxima of the wavelet transform at multiple scales, exact locations of singularities can be obtained. Now, we will see what happens in signals contaminated by noise.

### Singularities in noisy signals

The main theme of this chapter is to exploit the correlation of wavelet information across scales. This correlation is very important in terms of removing the noise from the signal. In the wavelet transform of a noisy signal, the singularities of the original signal and some part of the noise are retained at each scale. A. Pizurica and her colleagues exploited this interscale

information successfully to classify the wavelet coefficients [32]. If a coefficient has a smaller magnitude at a coarser scale, then its descendants at finer scales are likely to be small. Conversely, if coefficients corresponding to features are of larger magnitude at a finer scale, its parents at coarser scale are likely to be large. However, for coefficients caused by noise, the magnitudes will always decay along the scales, as shown in Figure 2.4. As one can see, the amplitude of the coefficients corresponding to singularities keeps on increasing from  $W_1$  to  $W_3$  and those corresponding to noise keeps on decreasing, giving only the signal singularities at scale 3.

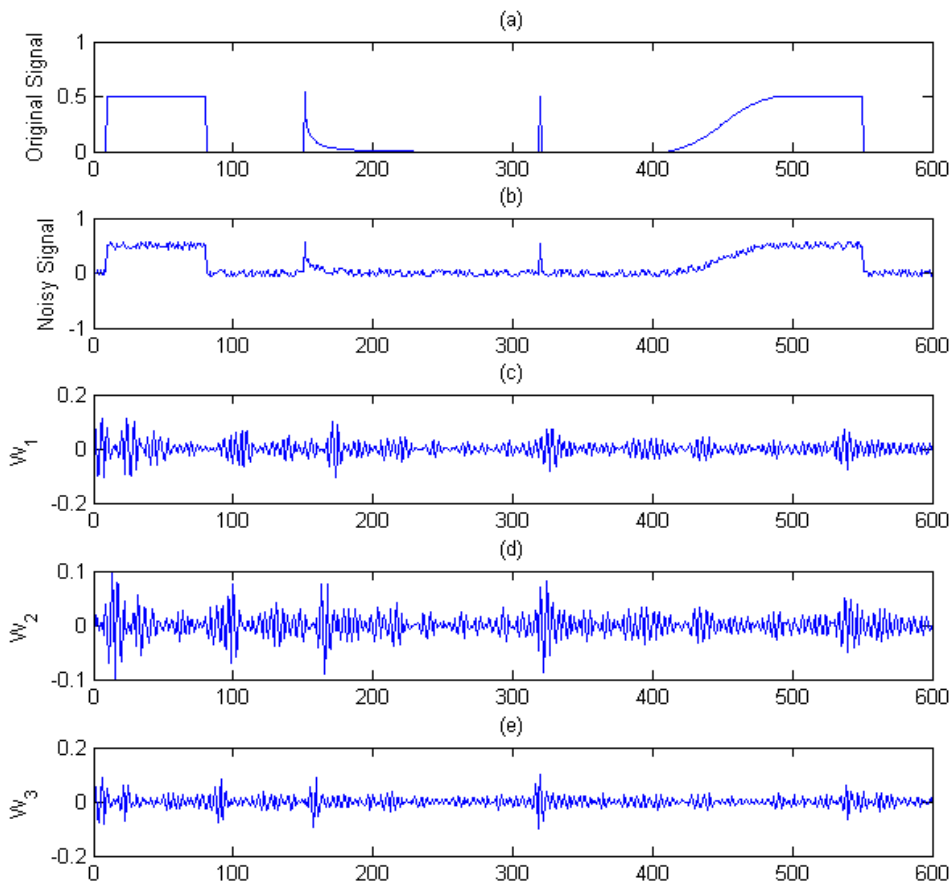


Figure 2.4: Illustration of noise removal using 'db8': (a) original signal, (b) signal with additive random noise, (c) detail coefficients at scale 1, (d) detail coefficients at scale 2 and (e) detail coefficients at scale

## 2.4 Nonseparable Wavelet

Wavelet transform is a mathematical tool having a family of basis functions with compact support. Basis functions are dilation and translation of mother wavelet.

Multi-dimensional sampling is represented by a lattice which can be separable or nonseparable. The research to date has focused more on separable wavelets and can be performed along one dimension at a time. Indeed, almost all wavelet image coding algorithms make use of the separable dyadic 2D discrete wavelet transform (DWT) [33], which applies the DWT separately to the rows and columns of the image. A 2D discrete time filter is a linear time-invariant system characterized by the transfer function:

$$H(\mathbf{z}) = \sum_{\mathbf{n} \in \mathbb{Z}^2} h[\mathbf{n}] \mathbf{z}^{-\mathbf{n}} \quad (2.10)$$

Where  $h[\mathbf{n}]$  is the impulse response of the filter and  $\mathbf{z} = \begin{bmatrix} z_0 \\ z_1 \end{bmatrix}$  is a complex vector. The frequency response  $H(\boldsymbol{\omega})$  of the filter is given by

$$H(\boldsymbol{\omega}) = \sum_{\mathbf{n} \in \mathbb{Z}^2} h[\mathbf{n}] e^{-j\boldsymbol{\omega} \mathbf{n}} \quad (2.11)$$

A 2D signal is said to be separable if it can be written as a tensor product of two 1D signals i.e.

$$x[\mathbf{n}] = x_0[n_0] \cdot x_1[n_1] \quad (2.12)$$

A 2D filter is said to be separable if its impulse response is a separable 2D signal. Or, in other words, the transfer function of a 2D separable filter can be written as a product of two 1D transfer functions i.e.

$$H(\mathbf{z}) = H_0(z_0) \cdot H_1(z_1) \quad (2.13)$$

Only if a 2D filter is separable, can it be implemented as two 1D filters, with each operating along each dimension. However, this is not true for general nonseparable 2D filters.

The advantage of this algorithm is its simplicity, which is beneficial for implementation. Separable multi-dimensional (MD) wavelets have a limitation in that their frequency support is always rectangular shaped. This limitation has been discussed in [34]. Consider a 2D sub-band coding scheme, where we want to separate the input 2D signal (image) into two sub-bands, a low-frequency sub-band and a high-frequency sub-band. With separable filter banks, this can be done by dividing the frequency region, either with respect to the horizontal frequency or with respect to the vertical frequency, as in Figure 2.5(a) and (b).

Separable wavelets are an extension of 1D bases and are good at capturing singularities in a localized region. In the case of images, objects usually have smooth boundaries which play an important role in visualizing and recognizing them. The separable wavelets can capture singularities in limited directions only and thus, they are not efficient in capturing smoothness across all possible directions. Therefore, a better representation is evolved in the form of nonseparable wavelets. It contains all the properties of separable wavelets- e.g. multiresolution, compact support, critical sampling etc. - along with the property of directionality. Some nonseparable wavelets, such as quincunx, are isotropic in nature and capture singularities in all directions. The quincunx wavelet has been discussed in detail in this thesis and is found to provide better results in comparison with 1D wavelets. For more versatile solutions, smoothness across different directions can be captured more efficiently using a variety of elongated shaped directional wavelets. The contourlet transform has incorporated this solution using different directional filter banks [36]-[41].

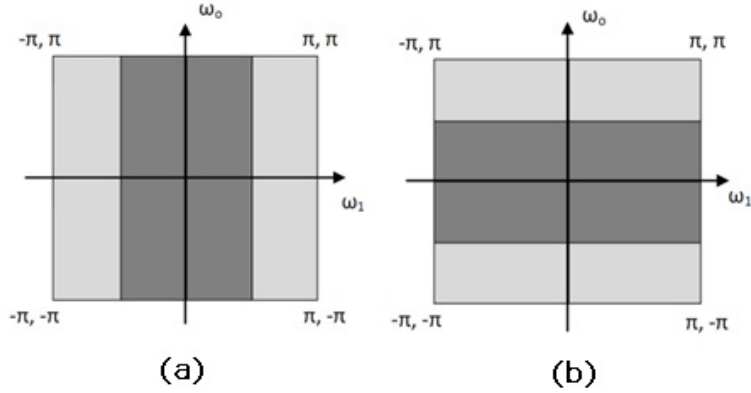


Figure 2.5: Division of frequency region with 2D two channels separable filter banks, (a) vertical, (b) horizontal [34]

### 2.4.1 Building Blocks of Multi-rate System

Similar to filter banks in 1D, 2D filter banks also have two basic building blocks, up-sampler and down-sampler. These basic operations are best understood using the concept of lattices. Consider a vector  $n \in \mathbb{Z}^2$  and  $V$  is a non-singular  $2 \times 2$  matrix. Lattice generated by matrix  $V$ , denoted by  $LAT(V)$  is the set of all two component vectors  $x$  such that  $x = V n$  and  $V$  is called generating matrix of  $LAT(V)$ . Clearly, the cardinality of set  $LAT(V)$  is infinity. For discrete time 2D signals, elements of  $V$  must be integers. We must note that lattice generated by a matrix  $V$  is unique but the converse is not true. For any unimodular matrix  $E$ ,  $LAT(V) = LAT(V E)$ .

For Example, lattice generated by Quincunx matrix  $Q = \begin{bmatrix} 1 & 1 \\ 1 & -1 \end{bmatrix}$  is shown in Figure 2.6. Note that the two vectors marked in the figure are the column vectors of the Quincunx matrix. The lattice points are linear combinations of these columns. It can be seen that the lattice generated by any matrix is a linear combination of the column vectors of the corresponding matrix. Also, note that the integer grid  $\mathbb{Z}^2$  can be seen as lattice generated by an identity matrix  $I$ ,

i.e.,  $LAT(I)$ . Both the basic operations up-sampling and down-sampling are described using a non-singular integer matrix (also called as sampling matrix).

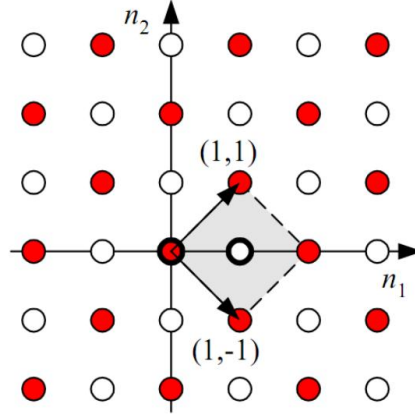


Figure 2.6: Lattice generated by Quincunx matrix

### 2.4.1.1 Down-Sampling

In simple terms, down-sampler or decimator (characterized by decimation matrix  $M$ ) accepts only points which are in the mapping of a point on  $LAT(M)$ . Mathematically, if  $y$  is the decimated signal and  $x$  is the input signal, then  $y[n] = x[Mn]$ . Down-sampling operation is shown in Figure 2.7 for Quincunx matrix.

Clearly, retained sample locations are linear combinations of the columns of the sampling matrix  $M$ . The columns of the matrix  $M$  form a parallelepiped, referred to as the fundamental parallelepiped  $FPD(M)$ . In 2D case,  $FPD(M)$  is a parallelogram but in higher dimensions, it is a parallelepiped.  $FPD(M) = \text{set of all the points } Mx, \text{ with } x = [0,1)^2$ .  $N(M)$  is the set of integer vectors in  $FPD(M)$ .  $J(M)$  is the number of integer vectors in  $FPD(M)$ .

$$J(M) = |\det(M)| \quad (2.14)$$

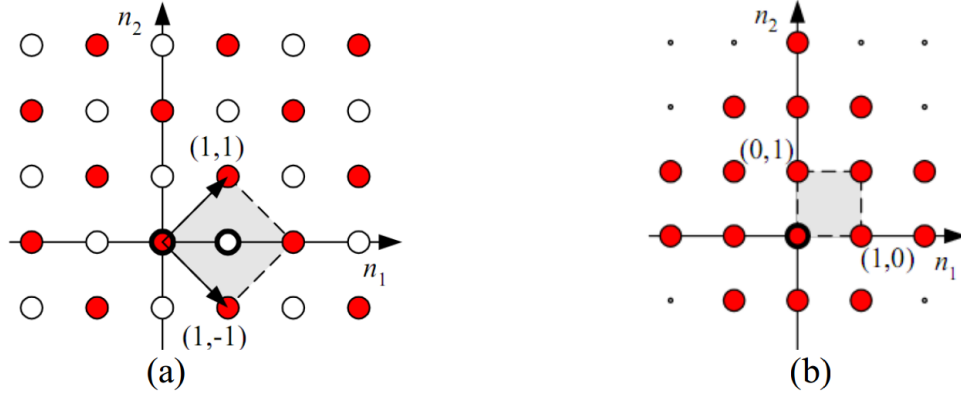


Figure 2.7: (a) Before down-sampling, (b) Down-sampling by Quincunx matrix

As the decimator picks only integer points (i.e., from set  $N(M)$ ), it picks one out of  $J(M)$  points. Hence, the decimation ratio is  $J(M)$ . To understand the aliasing caused by the decimator, we need to analyze it in the frequency domain. Fourier transform of the decimator is given by:

$$Y(\omega) = \frac{1}{J(M)} \sum_{k \in M(N^T)} X(M^{-T}\omega - 2\pi M^{-T}k) \quad (2.15)$$

Output at each frequency  $\omega$  can be obtained by summing the signal as a set of  $J(M)$  aliasing frequencies  $M^{-T}\omega - 2\pi M^{-T}k$  where  $k$  is a point in  $N(M)$ . Therefore, there are  $J(M) - 1$  aliases of the original signal. To get the original signal back, any one of  $J(M)$  bands can be non-zero at a time. Similar to 1D, a decimator simply maps a baseband signal and its  $J(M)-1$  shifted copies, which are centered at the offset frequencies  $2M^{-T}k$ , to unit frequency cell  $[-\pi, \pi]^2$ . As an example for the down-sampling matrix  $\begin{bmatrix} 1 & 1 \\ 2 & -2 \end{bmatrix}$ ,  $J(M)=4$ . Therefore, there will be 3 aliased regions. Figure 2.8(a) shows the baseband frequency support and Figure 2.8(b-d) show three aliases.

A filter  $H(z)$  can be used to remove all but one of the aliases and then decimate the signal to get the down-sampled signal. The filter  $H(z)$  is called decimation filter. The process is shown in

Figure 2.9. Superficially it looks like we cannot select the pass band for the decimation filter arbitrarily and it gets fixed as soon as the matrix and signal are fixed, but a closer look tells us that we can actually choose the shape of the pass band arbitrarily and yet get the correctly decimated signal. The only requirement is that one should not have copies of any frequency  $\omega$  in any other alias band.

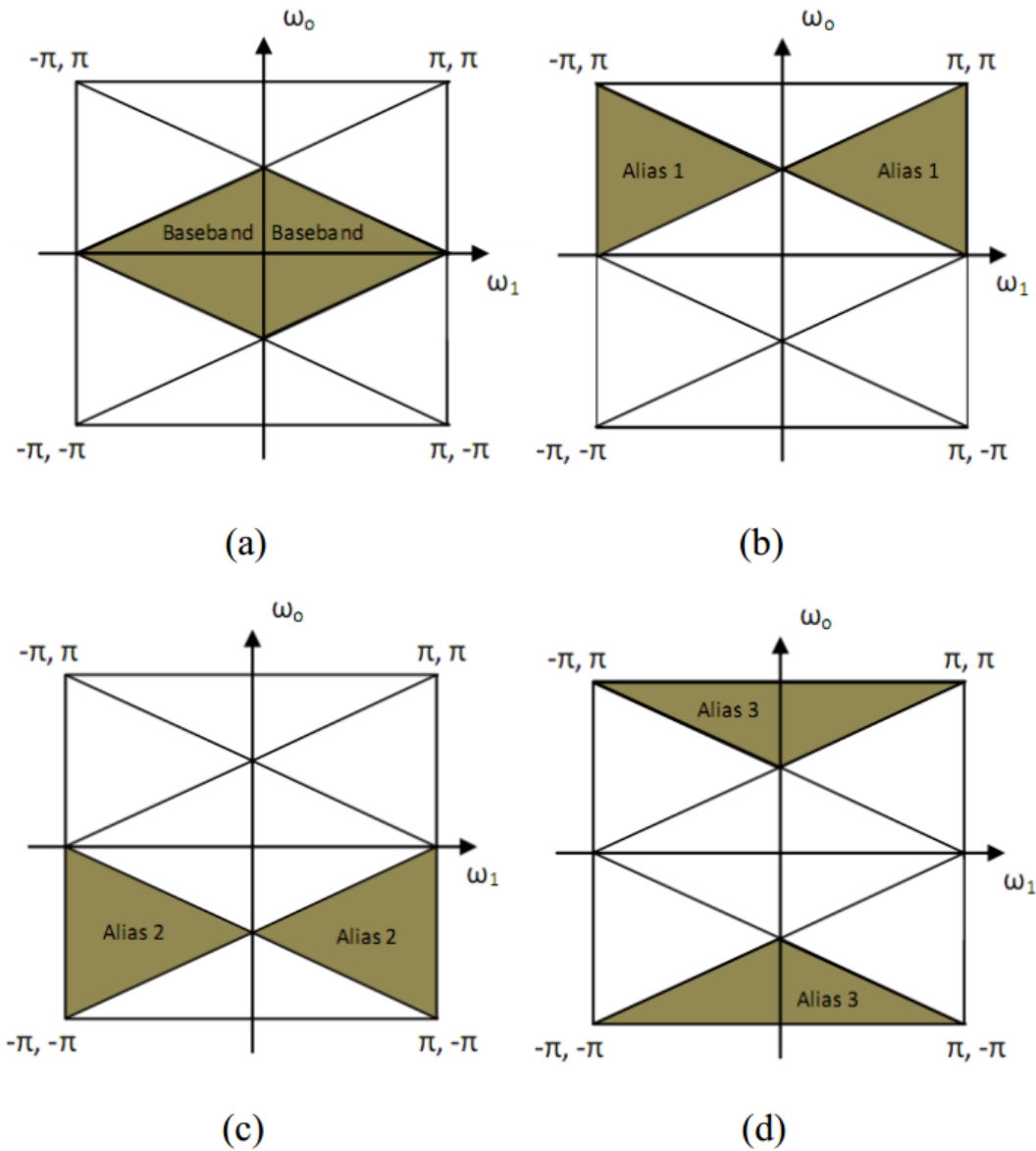


Figure 2.8: (a) Based-band region (b), (c) and (d) three aliases for decimation matrix M



Figure 2.9: Decimation

### 2.4.1.2 Up-Sampling

Up-sampler (characterized by non-singular matrix  $M$ ) maps a signal on the integer lattice, to a signal that is non-zero only on the points of the lattice generated by matrix  $M$ . Mathematically, the output is related to the input as follows:

$$y[n] = \begin{cases} x[M^{-1}n], & \text{if } M^{-1}n \in \mathbb{Z}^2 \\ 0, & \text{else} \end{cases} \quad (2.16)$$

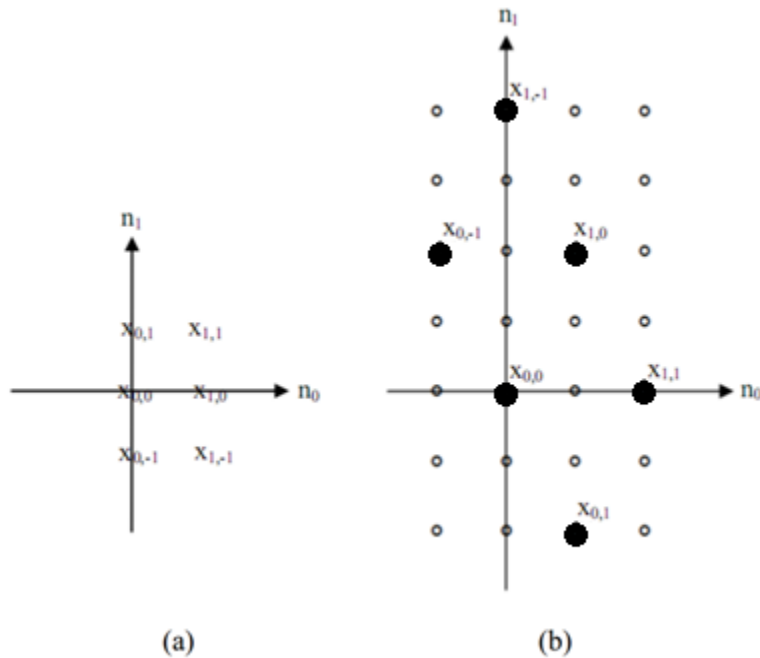


Figure 2.10: Up-sampling using matrix  $M$  (a) Input signal (b) Up-sampled signal

The process has been shown for matrix  $\begin{bmatrix} 1 & 1 \\ 2 & -2 \end{bmatrix}$  in Figure 2.10. Figure 2.10 (a) shows the 2x3 input signal and Figure 2.10(b) shows the output signal after up-sampling using the above

matrix. In frequency domain,  $Y(Z) = X(Z^M)$ . A vector  $Z = \begin{bmatrix} Z_0 \\ Z_1 \end{bmatrix}$  raised to matrix power  $M = \begin{bmatrix} M_{00} & M_{01} \\ M_{10} & M_{11} \end{bmatrix}$  is defined as follows:  $Z^m$  is a vector whose  $i^{\text{th}}$  entry is  $Z_0^{M_0} Z_1^{M_1}$ . In Fourier domain,  $(\omega) = X(M^T \omega)$ . Therefore, in Fourier domain up-sampling compresses pass-bands and skews their orientations (simple analogy to 1D case, where pass-band is simply compressed and scaled). One more feature to note is that the up-sampler gives a mapping such that  $J(M)$  similar compressed pass-bands are mapped to the unit cell. One unit cell of input is mapped to  $SPD(\pi M^T)$  which is defined as the set of all points  $\pi M^T x$ , where  $x \in [-1,1)^2$ . An up-sampler followed by a filter  $G(z)$  that passes only one of the compressed images and filters out all others is known as an interpolator. This is shown in the Figure 2.11. A perfect reconstruction filter bank is shown in the Figure 2.12. For a detailed derivation, refer to [35].

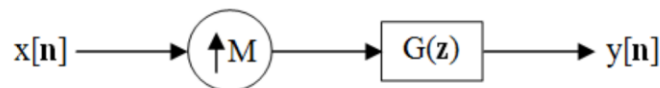


Figure 2.11: Interpolator

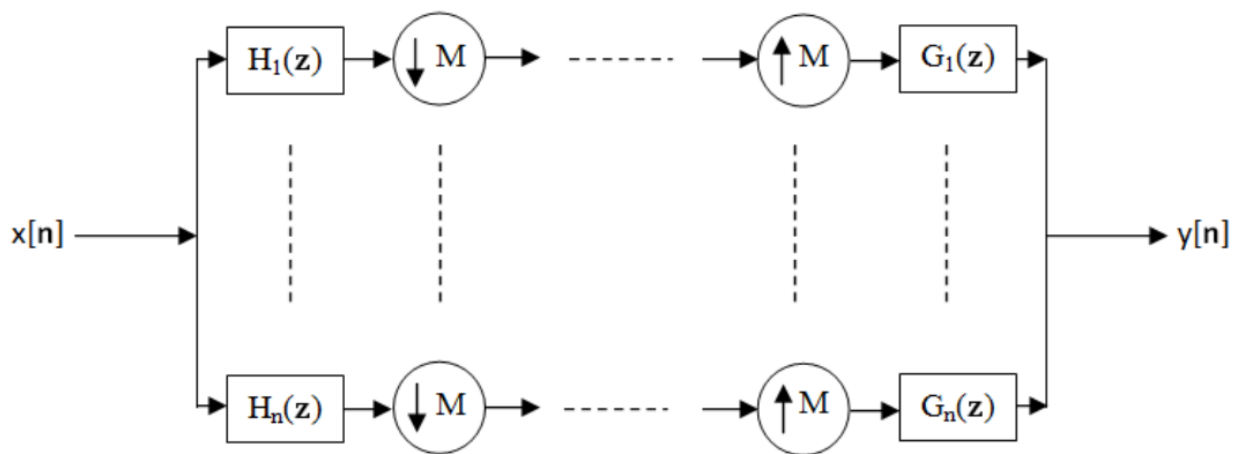


Figure 2.12: Perfect reconstruction filter bank

## 2.5 Quincunx Wavelet Transform

The quincunx is the simplest nonseparable decomposition which can be implemented using two-band filter bank. Due to the diamond shape support, a low pass filter has a diagonal cut off which is best suited for the human visual system. The detailed band captures the isotropic singularity and low pass band produces the approximate image. The quincunx has many applications in image processing such as denoising, texture characterization and video coding. The isotropic nature of quincunx filter banks utilizes the smoothness across contour direction which is needed at each scale for an in-depth study of noisy images [34] [35]. The quincunx has many applications in image processing such as denoising, texture characterization and video coding.

The subsampling process generates a sublattice starting from an input lattice. In general, the subsampling matrix  $D$  characterizes the subsampling of a discrete signal  $X(n)$  through the following equation:

$$Y(n) = X(Dn) \text{ with } n = (n_1, n_2)^T \quad (2.17)$$

$Y(n)$  is the signal after subsampling. For example, the dyadic sublattice, which is rectangular, is determined by:

$$D_d = \begin{pmatrix} 2 & 0 \\ 0 & 2 \end{pmatrix} \quad (2.18)$$

Or equivalently,

$$Y(n_1, n_2) = X(2n_1, 2n_2) \quad (2.19)$$

This is the most familiar way of subsampling for the 2D DWT. In this case, the matrix is diagonal, which implies the separability of dyadic subsampling. Indeed, horizontal and vertical

subsampling can be performed separately. The subsampling factor  $N$  is given by  $N = |Det(D)| = 4$ , implying that the number of samples per channel is reduced by the factor 4. Consequently, the wavelet filter bank has 4 channels with filters corresponding to three wavelets and one scaling function. Furthermore, the scaling factor is given by  $S = \sqrt{N} = 2$ . Hence, for dyadic subsampling the horizontal and vertical dimensions are reduced by the factor 2. The Quincunx lattice is shown in Figure 2.13, where gray dots represent the points on the Quincunx lattice.

Analogously, the following matrix characterizes the non-rectangular quincunx sublattice:

$$D_q = \begin{pmatrix} 1 & 1 \\ 1 & -1 \end{pmatrix} \quad (2.20)$$

Or equivalently,

$$Y(n_1, n_2) = X(n_1 + n_2, n_1 - n_2) \quad (2.21)$$

In this case, the quincunx sublattice is nonseparable because the matrix is not diagonal. Furthermore the subsampling factor  $N$  equals 2, which implies that the quincunx 2D DWT has two channels corresponding to one wavelet and one scaling function. This is similar to the 1D DWT. In each channel the number of samples is reduced by the factor 2 and the horizontal and the vertical dimensions are reduced by the scaling factor  $\sqrt{2}$ .

If we iterate the filter bank to obtain higher level decompositions, then the new sublattice is characterized by a matrix which is an integer power of the subsampling matrix  $D$ . For example, after two iterations or equivalently two decomposition levels, equation (2.21) becomes  $Y(n_1, n_2) = X(2n_1, 2n_2)$ . It is same as equation (2.18) which is a separable lattice, so we obtain for the quincunx case the following subsampling matrix:

$$D_d = \begin{pmatrix} 2 & 0 \\ 0 & 2 \end{pmatrix} \quad (2.22)$$

In general, the quincunx sublattice obtained after an even number of iterations corresponds to the dyadic sublattice with half the number of iterations. In quincunx, an odd number of iterations correspond to the nonseparable lattice and an even number of iterations corresponds to the separable lattice. Therefore, the quincunx 2D DWT requires twice the number of decomposition levels of the dyadic 2D DWT to obtain the same scale reduction factor  $S$ .

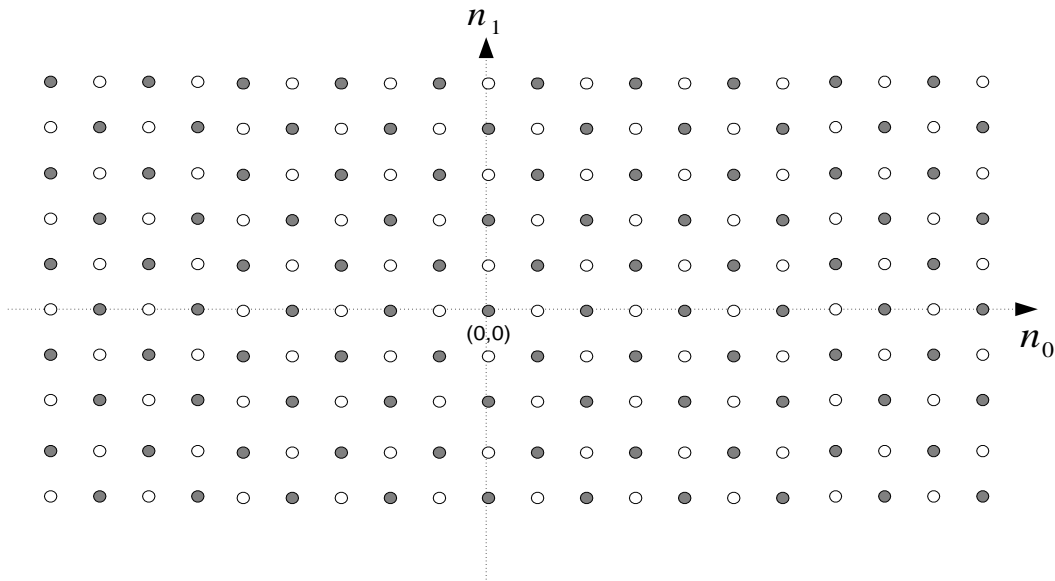


Figure 2.13: The Quincunx lattice (shaded point shows lattice points)

The 2-channel Quincunx filter bank is shown in Figure 2.14. The Quincunx low pass and high pass filters are often chosen to have diamond-shaped frequency supports, as shown in Figure 2.15. With this diamond-shaped frequency response, the low pass filter can preserve the high frequencies in the vertical and horizontal directions, which is a good match to the human visual system since the visual sensitivity is higher to changes in these two directions than the other directions.

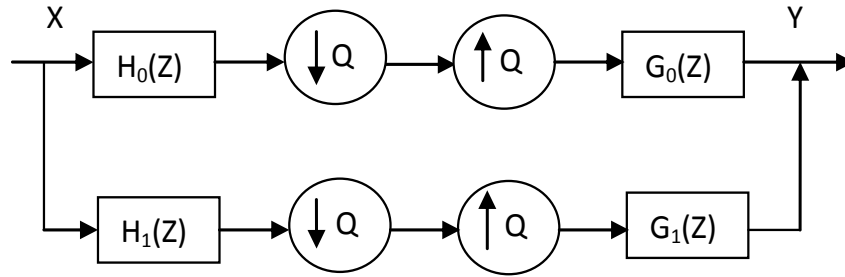


Figure 2.14: Quincunx filter bank

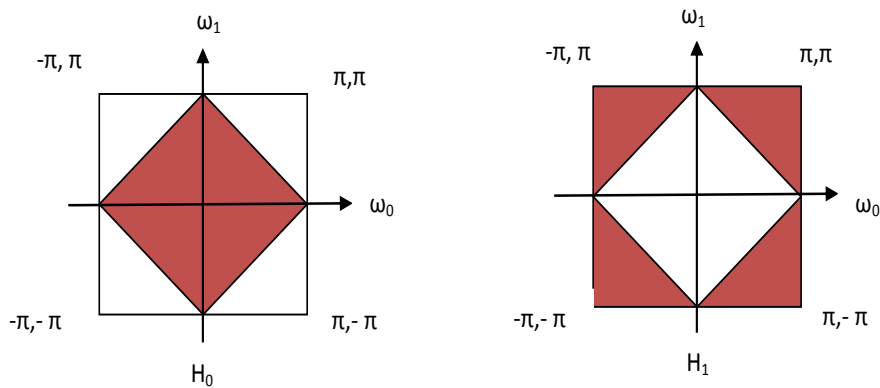


Figure 2.15: Frequency supports of filters in Quincunx filter bank

## 2.6 Lifting Scheme

Lifting scheme is a method developed by Wim Sweldens [70] for the construction of biorthogonal wavelets without using the Fourier transform. It requires far fewer computations and reduced memory for the DWT. The main motivation behind the development of the lifting scheme and the several related ideas was the search for fast algorithms to compute compact representations of functions and data sets using wavelets and filter banks.

Lifting consists of three stages, which are referred as *split*, *predict*, and *update*. These three stages will be briefly explained below. Consider a signal  $c^j$  with  $2^j$  samples which we want to transform into a coarser signal  $c^{j-1}$  and detail  $d^{j-1}$ .

**Split:** In this stage, the signal is split into two disjoint sets of samples. We can form one subset with even-indexed samples  $c_{2l}$  and other subsets consisting of the odd indexed samples  $c_{2l+1}$ . Each subset contains half as many samples as the original signal. The splitting into even and odd indexed samples is called the lazy wavelet transform.

$$(even_{j-1}, odd_{j-1}) := split(c^j)$$

**Predict:** If the signal has local correlation then we can use the even set to predict the odd one. Let us define an operator  $P(even_{j-1})$  for the prediction of the odd set. We then let the detail  $d^{j-1}$  be the difference between the odd sample and its prediction.

$$d^{j-1} = odd_{j-1} - P(even_{j-1})$$

In the case of Haar, the prediction is particularly simple.

$$d_i^{j-1} = c_{2l+1}^j - c_{2l}^j$$

**Update:** One of the key properties of the coarser signal is that it has the same average value as the original signal. It defines an operator  $Up$  of the form

$$c^{j-1} == even_{j-1} - Up(d^{j-1})$$

All this can be computed in place: The even location can be overwritten with the averages and the odd ones with details. An abstract implementation is given by

$$(odd_{j-1}, even_{j-1}) := split(c_j);$$

$$odd_{j-1} := P(even_{j-1});$$

$$even_{j-1+} := U(odd_{j-1});$$

The lifting structure guarantees Perfect Reconstruction (PR), and the so-called predict and update lifting steps can be used to increase the order of the polyphase matrix (and thus of the filters) while maintaining PR. Predict and update steps involve factorizing the analysis polyphase matrix in factors of the following form:

$$E'(z) = \begin{bmatrix} \overline{H_e} & \overline{H_o} \\ \overline{G_e} & \overline{G_o} \end{bmatrix} = \begin{bmatrix} 1 & U(z) \\ 0 & 1 \end{bmatrix} \begin{bmatrix} 1 & 0 \\ -P(z) & 1 \end{bmatrix} \quad (2.23)$$

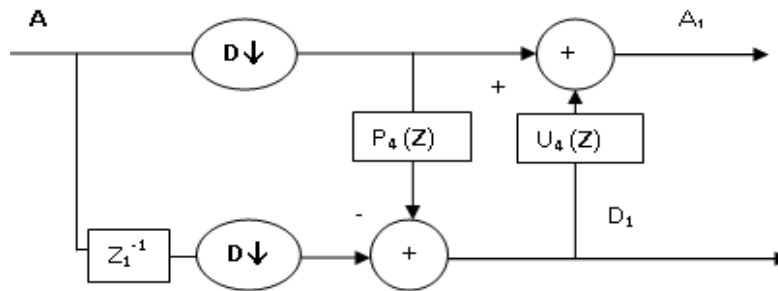
The corresponding synthesis matrix is given by

$$R'(z) = \begin{bmatrix} H_e & H_o \\ G_e & G_o \end{bmatrix} = \begin{bmatrix} 1 & 0 \\ P(z) & 1 \end{bmatrix} \begin{bmatrix} 1 & -U(z) \\ 0 & 1 \end{bmatrix} \quad (2.24)$$

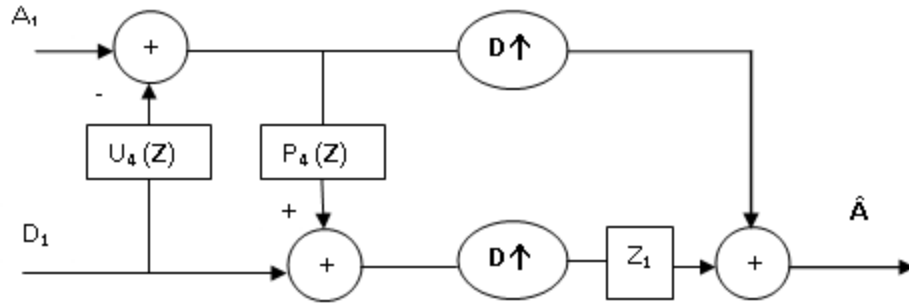
Where  $\overline{H}$  and  $\overline{G}$  are the analysis filter banks and  $H$  and  $G$  are the synthesis filter banks.

Lifting scheme is PR by construction, regardless of the specific choice of the update  $U(z)$  or predicts  $P(z)$  steps.

By using multiple such update and predict steps, with different  $P(z)$  and  $U(z)$  functions, a Quincunx filter bank with higher order filters can be constructed. The lifting framework is shown in Figure 2.16.



(a) Analysis



(b) Synthesis

Figure 2.16: Lifting Structure for Quincunx filter Bank in (a)-Analysis and (b)-Synthesis. The symbols ' $A$ ', ' $A_1$ ', ' $D_1$ ' and ' $\hat{A}$ ' represent input signal, approximation signal at next scale, detail signal at next scale and reconstructed signal respectively. The symbols ' $P_4$ ' and ' $U_4$ ' represent fourth order predict and update filters respectively.

## Chapter 3 Denoising Of 2DGE Images

### 3.1 Introduction

The undesirable components of an image are termed as noise. The presence of noise in 2DGE images might lead to false detection and classification, which might reduce the accuracy of a computer aided diagnostic system. Hence, denoising is a vital part of dealing with 2D Gel images. Generally, the noises that affect images can be classified into additive and multiplicative. Additive noise includes Gaussian noise, salt & pepper noise and uniform noise. Multiplicative noise, such as non-isometric noise and shot noise, is a by-product of the stochastic nature of the image acquisition system. Additive noise is independent of the spatial and spectral distribution of the image, while, multiplicative noise is dependent on the image and is difficult to remove without impairing the image. Since the noise variation greatly depends on the intensity levels of the image pixels being corrupted, it is not easy to establish an appropriate statistical model for the noise simply by examining the corrupted image.

The nonlinearities in the gel formation and image acquisition process lead to distortions, overlapped protein spots, saturated spots, faint spots, non-linear intensity and uneven background in the gel images. As a result, pre-processing steps are important before image analysis. Denoising is one of the most important pre-processing steps, and the overall accuracy of protein spot detection and analysis depends crucially on how effectively the gel images have been denoised.

Since denoising is the first operation in pre-processing operations pipeline, if successful, it may greatly impact results of downstream steps in the following ways:

- It prevents over-estimation of the image background and helps extracting faint, yet significant, spots [42].
- It prevents the formation of misleading spots (artifacts), thus resulting in more truthful spot matching and more accurate determination of the significant spots which have to be further analyzed by mass spectrometry methods.
- It leads to a more accurate estimation of spot properties (e.g. spot volume) leading to an improved spot differential analysis which is key for reliable biomarkers identification [43].

In the image denoising process, a trade-off must be made between noise suppression and preservation of singularities in the image. In case of 2DGE images, we expect the denoising process to remove the following features without introducing any significant distortions in an image:

- Background unevenness
- High-frequency noise
- Salt and pepper noise introduced due to dust
- Horizontal and vertical streaks

In this chapter, we have compared the different available methods of denoising in order to find the one which suits best for the 2D gel electrophoresis images. We proposed the use of nonseparable wavelet in denoising methods.

### **3.2 Denoising Techniques**

Denoising techniques, in general, are quite mature and have attracted a lot of research. Noise is inherent in all image acquisition systems and needs to be removed for accurate analysis of

images. A thorough literature survey [44] shows currently available techniques for denoising images.

We have focused on wavelet domain denoising techniques. Most wavelet techniques exploit the close relationship between denoising and compression. Non-linear thresholding on wavelet coefficients is a standard way of denoising natural images. This technique is described in detail in the following section.

### **3.3 Wavelet Shrinkage Method**

Wavelet denoising must not be confused with smoothing; smoothing only removes the high frequencies and retains the lower ones. Wavelet shrinkage is a non-linear process and this is what distinguishes it from linear denoising techniques such as least squares. Wavelets are a very powerful tool for de-correlation and hence, compression. This property makes wavelets a suitable choice for denoising techniques.

#### **3.3.1 Motivation for Wavelet Shrinkage**

As shown in Figure 3.1(a) a signal with singularities is taken and corrupted by additive white Gaussian noise (AWGN) of SNR 20dB and is then decomposed with the 'db6' wavelet. A histogram of the magnitude of coefficients is shown in Figure 3.1(b). A few important conclusions can be drawn from the histogram, most of the coefficients are very small, or in other words, most significant information is represented by a very small number of coefficients (the tail of histogram). This sparse nature of wavelet coefficients suggests that even if we remove most of the small coefficients (by making them zero) below a certain threshold and take the inverse wavelet transform, then the reconstructed signal will retain most of the information and hence will be noise free.

To state more precisely, we are motivated to study this idea of wavelet coefficient shrinkage based on the following assumptions [45]:

- The de-correlating property of wavelet transform creates a sparse signal, i.e. most of the coefficients are very small (zero or close to zero).
- Noise is spread out equally along all coefficients.
- The noise level is not too high; hence we can distinguish the signal wavelet coefficients from the noisy ones.

As it turns out, this method is indeed effective and thresholding is a simple and efficient method for noise reduction. Further, inserting zeros creates more sparsity in the wavelet domain and here we see a link between wavelet denoising and compression which has been described in many sources such as [48].

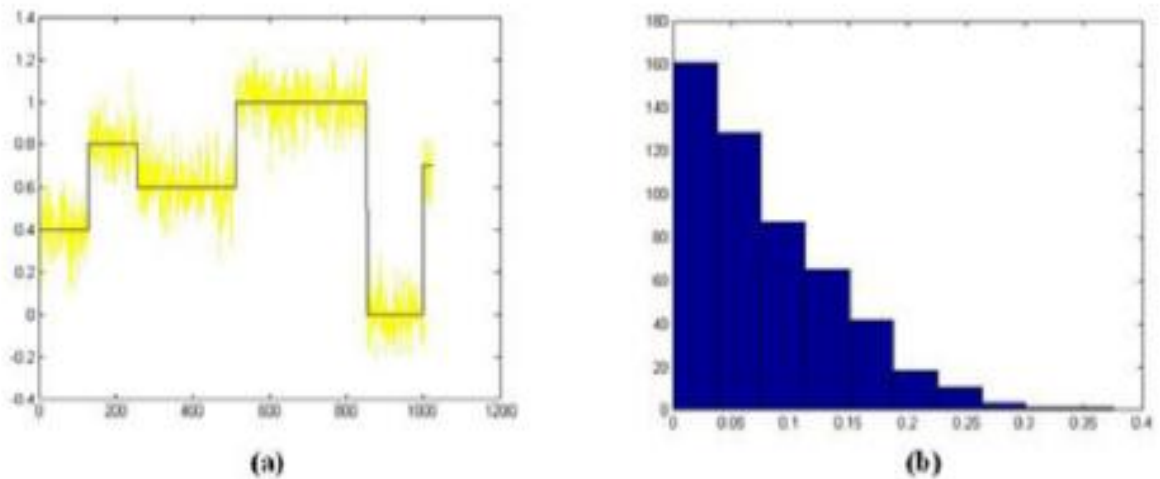


Figure 3.1: (a) Original signal with singularities (in black) and noisy signal (in yellow)  
(b) histogram of magnitude of 'db6' wavelet coefficients of noisy signal

### 3.3.2 Thresholding: Soft and Hard

As the name itself suggests, hard thresholding is 'keep or kill' procedure. If the magnitude of a wavelet coefficient is above a certain threshold  $\lambda$ , then keep the coefficient as it is. Otherwise, kill the coefficient by making it zero. Hard thresholding operator is defined as:

$$D(U, \lambda) = \begin{cases} U, & \text{if } |U| > \lambda \\ 0, & \text{else} \end{cases} \quad (3.1)$$

It is very simple and intuitive but has some problems associated with it. Sometimes noisy coefficients may pass through hard thresholding procedure and give unwanted artifacts in the denoised data. The answer to this problem is soft thresholding.

Soft thresholding operator is defined as:

$$D(U, \lambda) = \text{sgn}(U) \max(|U| - \lambda, 0) \quad (3.2)$$

Transfer functions for Hard and soft thresholding are shown in Figure 4.2(a) and (b) respectively. Contrary to hard thresholding, soft thresholding shrinks the coefficients above the threshold in absolute value by the same threshold. Soft thresholding has some advantages. It makes some algorithms mathematically more tractable [49].

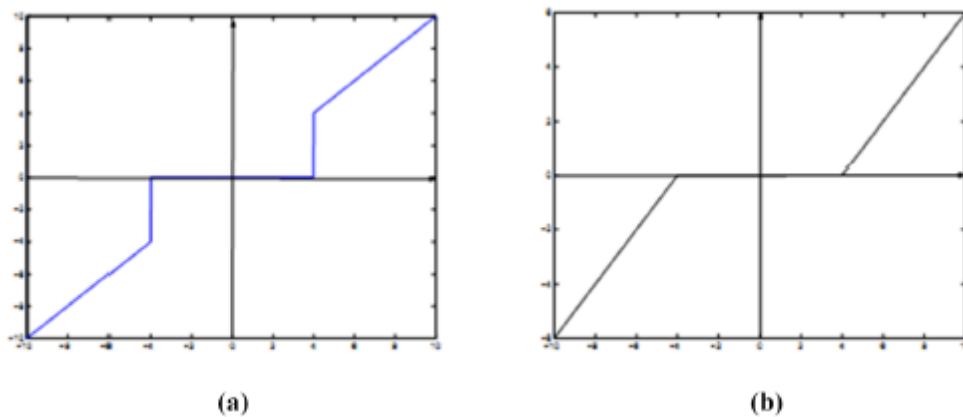


Figure 3.2: (a) Hard thresholding (b) Soft thresholding

### 3.3.3 Image Denoising Algorithm

The algorithm for image denoising using wavelet shrinkage is very simple and involves the following steps:

- Calculate the wavelet transform of the image
- Threshold the wavelet coefficients
- Compute the inverse wavelet transform to get the denoised image

### 3.3.4 Threshold Determination

It is very important to choose the threshold wisely for proper denoising. If we choose a very small threshold, we will get an output very close to the input image but it will still be noisy. On the other hand, if we choose a very large threshold, most of the wavelet coefficients will become zero, which might result in the killing of some significant image coefficients. This results in a smoothed image and leads to image distortion. Paying too much attention to smoothness will lead to a blurred image. In literature, there are various shrinkage methods to determine thresholds. We will investigate three of them, viz. VisuShrink, SUREshrink, BayesShrink.

#### 3.3.4.1 VisuShrink

VisuShrink is a thresholding technique which applies the universal threshold proposed by Donoho and Johnstone [46]. This threshold is given by  $\sigma\sqrt{2\log M}$  where  $M$  is the number of pixels in the image and  $\sigma$  is the noise variance estimated from the wavelet coefficients of diagonal details at the first level of decomposition by equation (3.3):

$$\sigma = \left(\frac{1}{.6745}\right) \text{median}(|C_{HH1}|) \quad (3.3)$$

It is proved [47] that the maximum of any  $M$  independent and identically distributed (iid) values distributed as  $N(0, \sigma^2)$  will be smaller than the universal threshold with high probability, with the probability approaching 1 as  $M$  increases. Thus, with high probability, a pure noise signal is estimated as being identically zero. However, for denoising images, VisuShrink is found to yield an overly smoothed estimate. This is because the universal threshold is derived under the constraint that with high probability the estimate should be at least as smooth as the signal. So, the universal threshold tends to be high for large values of  $M$ , killing many signal coefficients along with the noise. Thus, the threshold does not adapt well to discontinuities in the signal.

### 3.3.4.2 SUREshrink

Let  $\{\mu = \mu_i, i = 1, \dots, \dots, \dots, d\}$  be a  $d$ -dimensional vector, and let  $x = x_i$  (with  $x_i$  distributed as  $N(\mu_i, 1)$ ) be multivariate normal observations with mean vector  $\mu_i$ . Let  $\hat{\mu} = \hat{\mu}(x)$  be a fixed estimate of  $\mu$  based on the observations  $x$ . SURE (Stein's unbiased Risk Estimator) [46] is a method for estimating the coefficients by minimizing the loss  $\|\mu - \hat{\mu}\|^2$  in an unbiased fashion.

In our case  $\hat{\mu}$  is the soft threshold estimator  $\hat{\mu}_i^{(t)} = \eta_t(X_i)$ . We apply Stein's result to get an unbiased estimate of the risk  $\mathbb{E}\|\mu_t(x) - \hat{\mu}\|^2$ :

$$SURE(t; x) = d - 2 \cdot \# \{i: |x_i| < t\} + \sum_{i=1}^d \min(x_i, t)^2 \quad (3.4)$$

For an observed vector  $x$  (in our problem,  $x$  is the set of noisy wavelet coefficients in a sub-band), we want to find the threshold  $T$  that minimizes  $SURE(t; x)$  i.e.

$$T = \arg \min_t SURE(t; x) \quad (3.5)$$

### 3.3.4.3 BayesShrink

In BayesShrink [47], we determine the threshold for each sub-band assuming a Generalized Gaussian Distribution (GGD). It is a data dependent and sub-band adaptive threshold. Equations to calculate Bayesian threshold are given as follows:

$$\sigma = \frac{\text{median}(|Y_{ij}|)}{.6745}, \quad Y_{ij} \in \text{Subband } HH_1 \quad (3.6)$$

This is an adaptive thresholding procedure, so we need to calculate the threshold for every detail sub-band separately.

$$T = \frac{\sigma^2}{\sigma_s} \quad (3.7)$$

where,  $\sigma_s$  is calculated for each sub-band as given in equation (3.8).

$$\sigma_s = \sqrt{\max \left\{ \left( \frac{1}{n} \sum_{i,j=1}^n C_{ij}^2 - \sigma^2 \right), 0 \right\}} \quad (3.8)$$

Where  $C_{ij}$  are wavelet coefficients of the sub-band under consideration.

To demonstrate the working of this algorithm, an example is shown in Figure 3.3. Original image 'Lena' was taken and Gaussian noise with standard deviation 0.005 was added to it. Various shrinkage procedures were applied to the noisy image and the corresponding denoised images are shown in Figure 3.3. We have obtained good results with Bayes threshold.

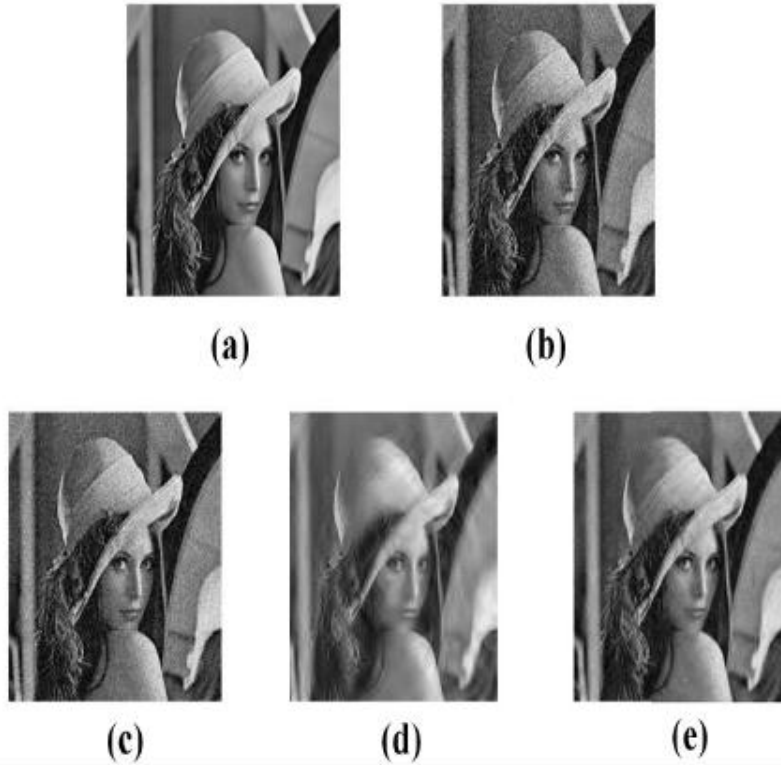


Figure 3.3: (a) Original Image (b) Corrupted by Gaussian noise (c) Denoised by VisuShrink (d) Denoised by SUREshrink (e) Denoised by BayesShrink

### 3.4 Image Denoising: A Wavelet Domain Modeling Approach

In the previous section, we discussed a non-parametric approach to denoise 2DGE images. In this section, we will discuss a denoising approach based on stochastic modelling of wavelet coefficients.

Accurate image modelling is a critical component of many image processing tasks. In [48], a simple yet effective, statistical and spatially adaptive wavelet image model was developed, which formed the basis of the state-of-the-art estimation quantization (EQ) compression algorithm. In [49], a closely related model for image wavelet coefficients has been developed and applied for denoising the images corrupted by additive white Gaussian noise (AWGN). In

this dissertation, we have first shown that 2DGE images fulfill the requirements for this model to be valid and then implemented this model in MATLAB using Quincunx wavelet.

There is a close relationship between image compression and image denoising. In fact, the use of lossy data compression itself was proposed for denoising with the intuition that a typically correlated signal is compressible but noise is not [50]. Using this model, this intimate relation between compression and denoising is exploited using state-of-the-art models for compression. This model significantly reduces the computational burden yet produces comparable results in terms of mean-squared error (MSE) and perceptual image quality. The key ingredient of the algorithm is the use of simple but efficient spatial adaptation techniques. This algorithm is based on DWT. The transform coefficients within sub-bands are modelled as independent identically distributed random variables with generalized Gaussian distribution (GGD).

This model takes an approach which exploits the local structure of the wavelet image coefficients. Also, it uses linear Minimum Mean Squared Error (MMSE) like estimation instead of coefficient thresholding.

### **3.4.1 Stochastic Model for Wavelet Coefficient**

Image wavelet coefficients are modelled as a realization of a doubly stochastic process. Specifically, the wavelet coefficients are assumed to be conditionally independent zero-mean Gaussian random variables, given their variances. These variances are modelled as identically distributed, highly correlated random variables. A stochastic prior is put on local variances. For estimation purposes, we approximate wavelet coefficients as locally i.i.d [49]. To verify the above stated model in 2D gel image as shown in Figure 3.5, we have taken the histogram of the original high band coefficients from the first scale, obtained by employing Daubechies-8

wavelets as shown in Figure 3.4(a). Figure 3.4(b) shows those coefficients normalized by their estimated standard deviations. Observe that the normalized histogram is well approximated by a zero-mean, unit variance Gaussian probability density function (p.d.f.).

It is assumed that image pixels are corrupted by AWGN of known variance. Let  $X(k)$  represent the orthonormal wavelet coefficients of the clean image. The wavelet coefficients of the noisy image are given by  $Y(k) = X(k) + n(k)$ , where  $n(k)$  is AWGN due to orthonormality of the chosen wavelet transform. The denoising algorithm operates in two steps. Initially, we perform an approximate maximum a posterior (MAP) estimation of the variance  $\sigma^2(k)$  for each coefficient using the observed noisy data in a local neighbourhood and a prior model for  $\sigma^2(k)$ . The estimate  $\hat{\sigma}^2(k)$  is then substituted for  $\sigma^2(k)$  in the expression for the Minimum Mean Squared Error (MMSE) estimator of  $X(k)$ . Both these steps are summarized in Figure 3.6(a) and described in more detail in further sections.

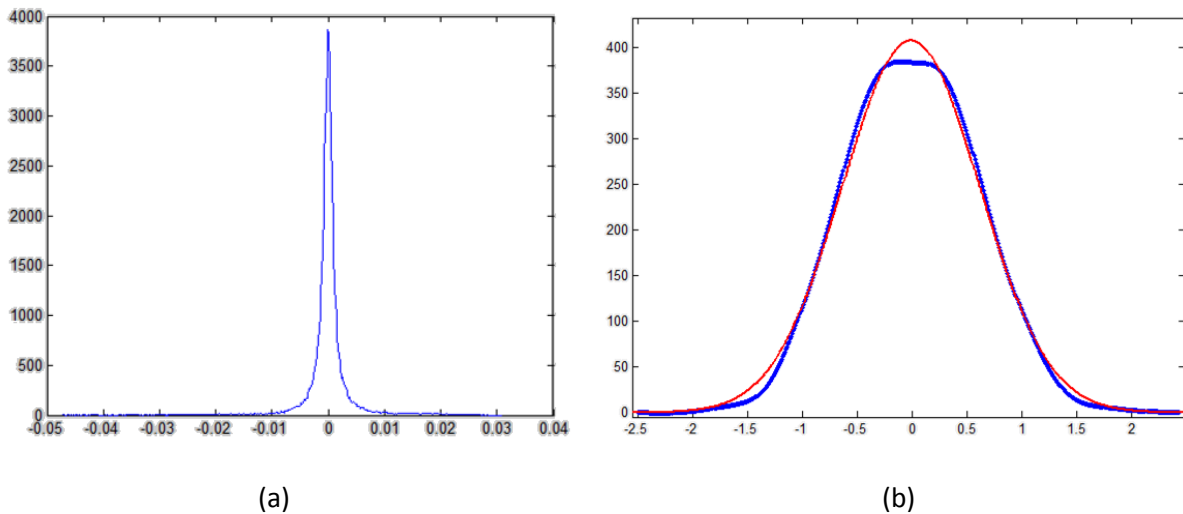


Figure 3.4: (a) Histogram of the high-band wavelet coefficients of gel Image (b) Blue line: histogram of the same coefficients scaled by estimated local standard deviations. Red line: unit-variance, zero-mean Gaussian pdf.

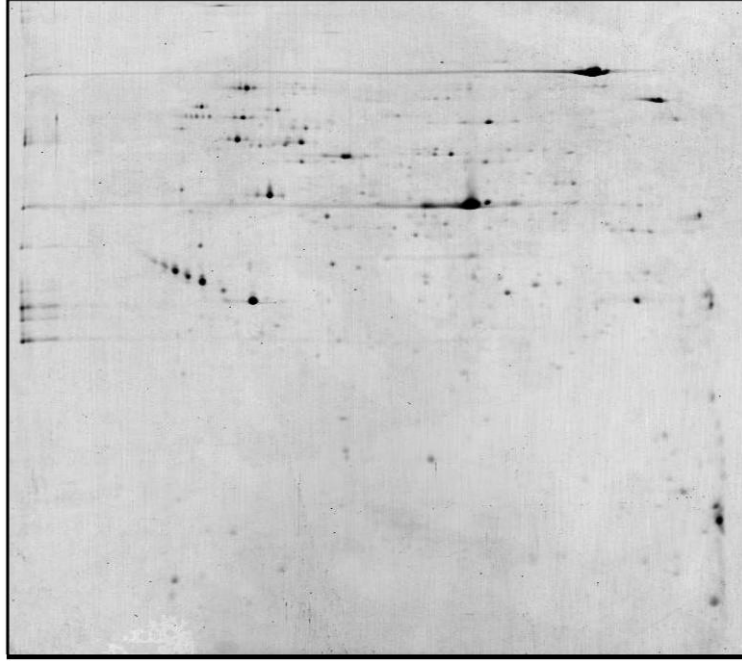


Figure 3.5: A 2DGE image from database [1]

### 3.4.1.1 Denoising Algorithm

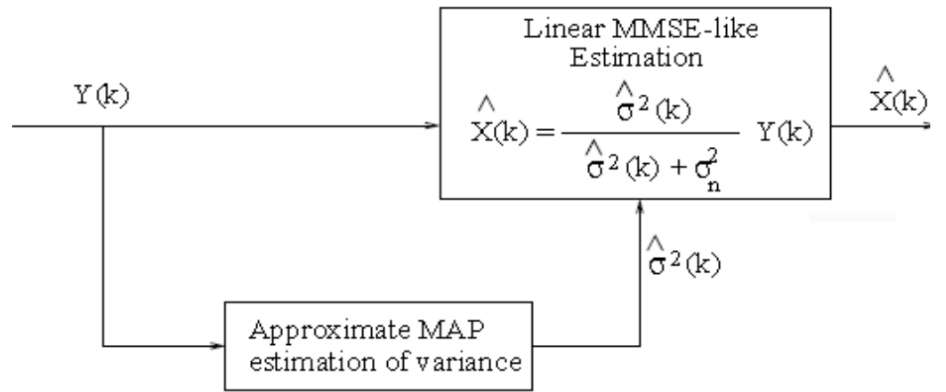
Given  $\sigma^2(k)$ , the wavelet coefficients  $X(k)$  are independent Gaussian variables, so the MMSE estimator for  $X(k)$  is given by:

$$\hat{X}(k) = \frac{\sigma^2(k)}{\sigma^2(k) + \sigma_n^2} Y(k) \quad (3.9)$$

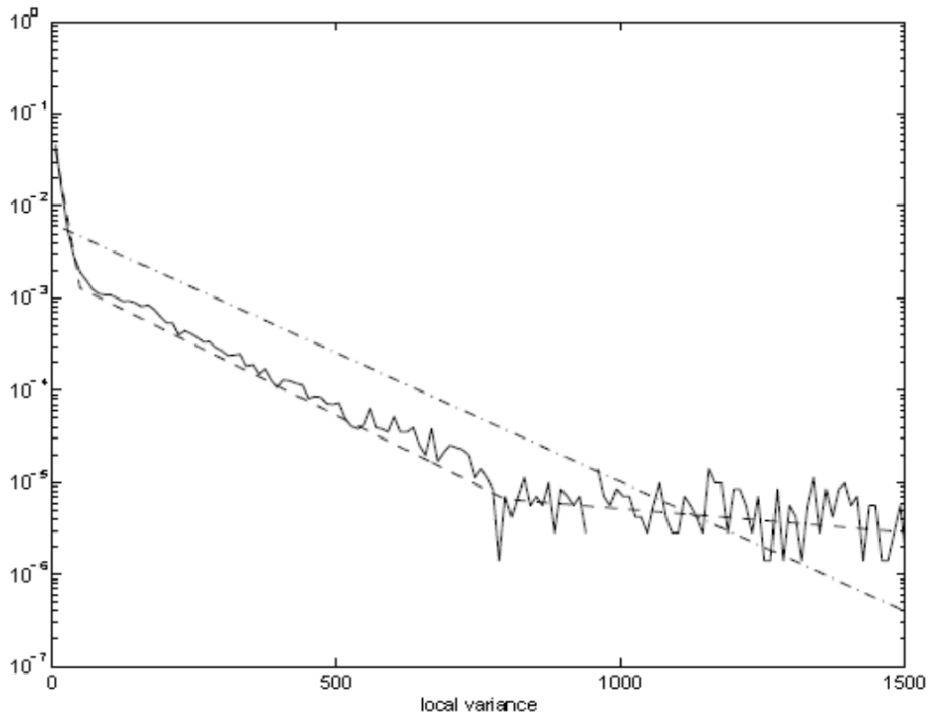
We emphasize that this assumes  $\sigma^2(k)$  is deterministic and known. But in fact,  $\sigma^2(k)$  is not known, so we construct a linear MMSE-like estimator.

$$\hat{X}(k) = \frac{\hat{\sigma}^2(k)}{\hat{\sigma}^2(k) + \sigma_n^2} Y(k) \quad (3.10)$$

where  $\hat{\sigma}^2(k)$  is an estimate for  $\sigma^2(k)$ . Results indicate that performance of the proposed approximate MMSE predictor is dependent, to a very large extent, on the quality of the estimator of  $\hat{\sigma}^2(k)$ .



(a)



(b)

Figure 3.6:(a) Block diagram of the denoising algorithm (b) Histogram of the estimated local variance of the coefficients (solid line) in wavelet image sub-band, approximated using a single exponential prior (dash-dotted line) and a mixture of exponentials that consists of three single exponentials in three non-overlapping regions (dashed line).

### 3.4.1.2 Estimation of Variance Field

The estimation of the variance field  $\sigma^2(k)$  is the crux of this denoising algorithm. For each data point  $Y(k)$ , an estimate of  $\sigma^2(k)$  is formed based on a local neighbourhood  $N(k)$ . We use a square window  $N(k)$  centered at  $Y(k)$ . Assuming the correlation between variances of neighbouring coefficients is high, we have  $\sigma^2(j) \approx \sigma^2(k)$  for all  $j \in N(k)$ . Then we compute an approximate Maximum Likelihood (ML) estimator.

$$\hat{\sigma}^2(k) = \underset{\sigma^2 \geq 0}{\operatorname{argmax}} \prod_{j \in N(k)} P(Y(j)|\sigma^2) = \max \left( 0, \frac{1}{M} \sum_{j \in N(k)} Y^2(j) - \sigma_n^2 \right) \quad (3.11)$$

where  $P(\cdot|\sigma^2)$  is the Gaussian distribution with zero mean and variance  $\sigma^2 + \sigma_n^2$  and  $M$  is the number of coefficients in the neighbourhood  $N(k)$ . Now, assume a prior marginal distribution  $f_\sigma(\sigma^2)$ . Then we obtain an approximate estimate of  $\sigma^2(k)$  as

$$\hat{\sigma}^2(k) = \underset{\sigma^2 \geq 0}{\operatorname{argmax}} \prod_{j \in N(k)} P(Y(j)|\sigma^2) f_\sigma(\sigma^2) \quad (3.12)$$

In Figure 3.6(b), we plot a histogram of the estimated local variances using equation (3.11) with a  $7 \times 7$  window for a typical high pass sub band of an image (solid line). The exponential prior

$$f_\sigma(\sigma^2) = \lambda e^{-\lambda \sigma^2} \quad (3.13)$$

shown by the dash-dotted line in Figure 3.6(b) is a reasonable candidate to fit the original histogram. The approximate MAP estimate for using an exponential prior is given by:

$$\hat{\sigma}^2(k) = \max \left( 0, \frac{M}{4\lambda} \left[ -1 + \sqrt{1 + \frac{8\lambda}{M^2} \sum_{j \in N(k)} Y^2(j)} \right] - \sigma_n^2 \right) \quad (3.14)$$

The authors of [49] verified that MAP estimate gives an improvement in denoising performance over ML estimate. They also experimentally found out that accurate modelling of

the histogram does not give any significant improvement as far as denoising is concerned. In this thesis, we have implemented both ML and MAP estimates and compared them.

### **3.5 Use of Nonseparable Wavelet**

We have implemented the wavelet shrinkage and stochastic methods in nonseparable quincunx wavelet domain and studied the results. We must note that quincunx wavelet transform has not been used previously for denoising of gel images. To verify whether we can apply the stochastic model to 2DGE images using Quincunx wavelets, we decomposed various 8-bit 2DGE images using Quincunx wavelets. We found that all sub-bands are approximately Gaussian with zero means. In Figure 3.7 (a), (b), (c) and (d), histograms of its various sub-bands are shown. It can be clearly seen that they are all approximately Gaussian. This is also a good reason for applying Bayes's threshold based wavelet shrinkage method.

### **3.6 Evaluation Methodology**

We have evaluated the performance of all the denoising algorithms described in sections 3.3 and 3.4 using 8-bit synthetic as well as real 2DGE images. We have generated a synthetic gel image using real 2DGE images by cutting out protein spots from them. We have tried to get all kinds of spots from real image: saturated spots, streaks, faint spots, overlapping spots etc. We put these spots on a white background using image editing tools. Further, we added white Gaussian noise of different variances: 30, 35 and 40 as well as salt and pepper noise. From now on, these will be referred to as clean image, noisy image-1 ( $\sigma = 30$ ), noisy image-2 ( $\sigma = 35$ ) and noisy image-3 ( $\sigma = 40$ ). These images are shown in Figure 3.8.

We have applied the denoising procedures on the noisy images and then calculated Peak Signal to Noise Ratio (PSNR) between denoised image and clean image. Higher the PSNR,

better the performance but this is not the only criteria which should be looked at. Since 2DGE images contain non-stationary noise and non-linear artifacts, only PSNR does not suffice. We have also looked into artifacts introduced by the denoising procedure. Lower artifacts imply better performance. Lastly, we compared the performance of various methods with that of the commercial software Delta2D.

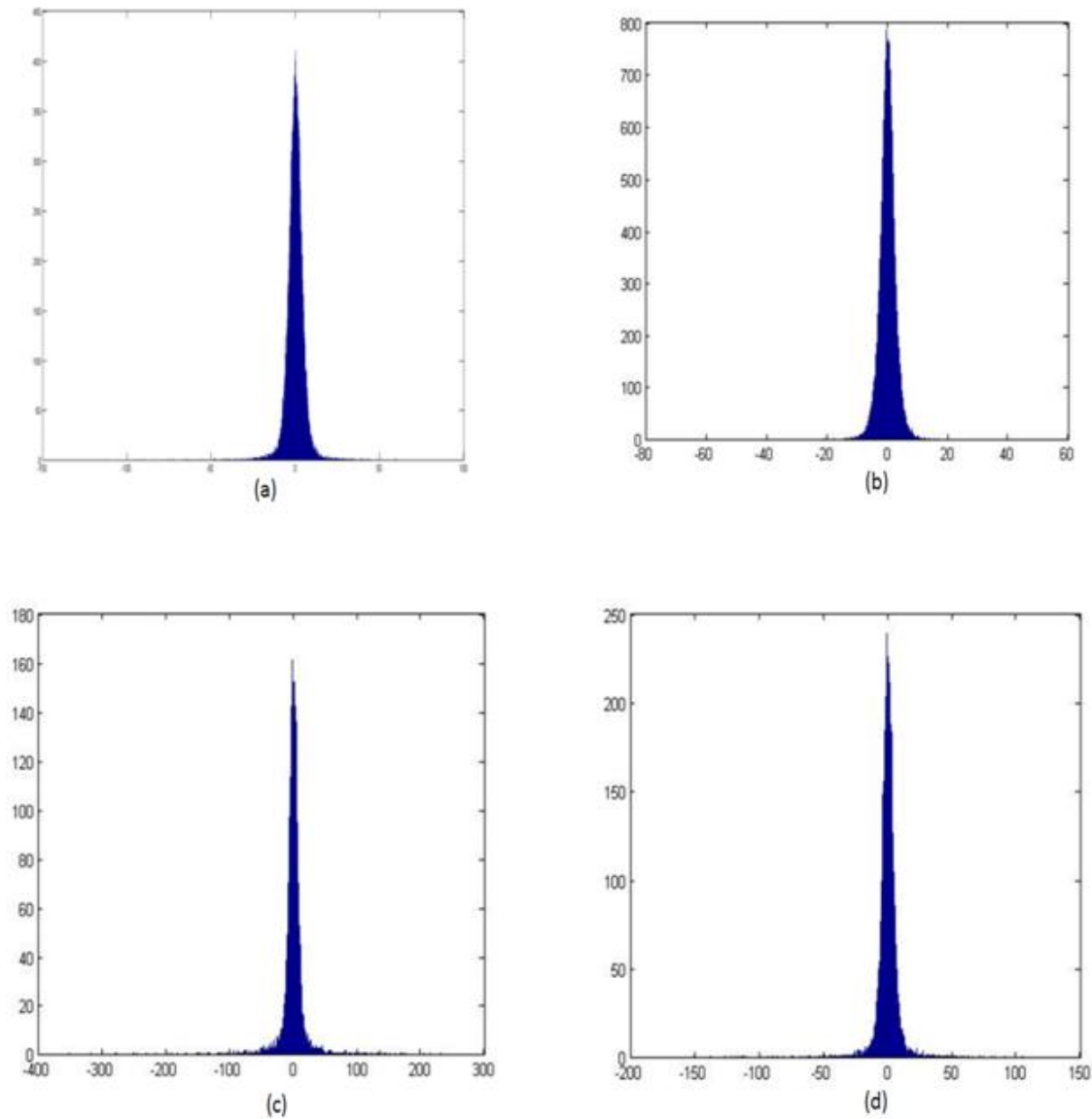


Figure 3.7: Histograms of Quincunx wavelet coefficients of various sub-bands of the 2DGE image in

Figure 3.5. (a) Level-1 Scale-1 (b) Level-1 Scale-2 (c) level-2 Scale-1(d) Level-2 Scale-2

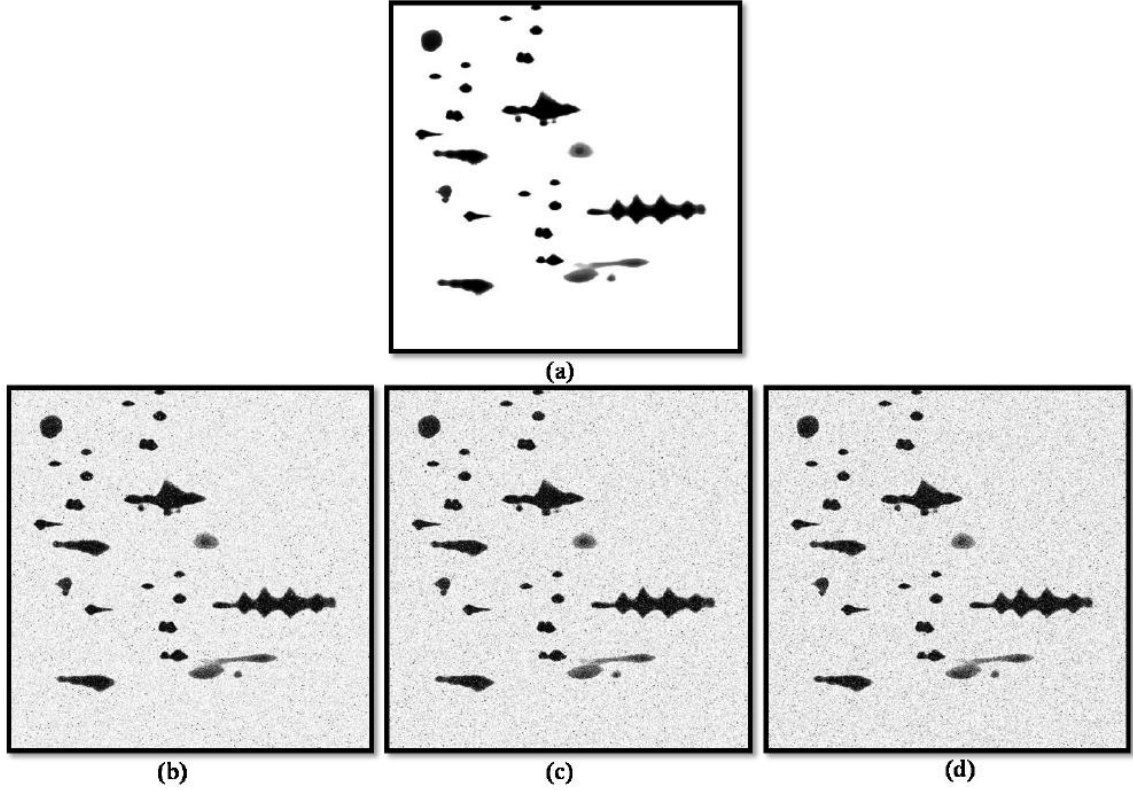


Figure 3.8: (a) Clean synthetic image (b) Noisy image-1 ( $\sigma=30$ ) (c) Noisy image-2 ( $\sigma=35$ ) (d) Noisy image-3 ( $\sigma=40$ ).

### 3.6.1 PSNR Based Analysis on Synthetic Images

Peak signal to noise ratio (PSNR) is a ratio between the maximum possible value of an image and the power of distorting noise that affects the quality of its representation.

Mathematically, PSNR is represented as:

$$PSNR = 20 \log_{10} \left( \frac{MAX_I}{\sqrt{MSE}} \right) \quad (3.15)$$

where MSE is

$$MSE = \frac{1}{mn} \sum_{i=0}^{m-1} \sum_{j=0}^{n-1} \|f(i,j) - g(i,j)\|^2 \quad (3.16)$$

where  $f$  is the original image,  $g$  is the noisy image and  $m, n$  are rows and columns of the image respectively.  $MAX_I$  is the maximum signal value of the original image.

On synthetic images we added Gaussian noise of  $\sigma = 30, 35, 40$  and salt & pepper noise. Denoising was performed using wavelet and known methods; the PSNR of denoised images w.r.t the original image was obtained for each method. Results are tabulated in Table 3.1-3.3. We observed that soft thresholding gives better performance than hard thresholding in all cases, as expected. Bayes threshold gives the best performance among all thresholds. In the Table 3.4, results are reported for Bayes threshold except for CWT for which bivariate shrinkage has been used as proposed in [50]. Denoised images for  $\sigma = 30$  are shown in Figure 3.9.

The PSNR values obtained from undecimated quincunx wavelet transform are better than the other methods. However, even though the PSNR values of the statistical modelling method are not high, the images obtained from them seem to be comparable to that of the complex wavelet transform. Hence, we have selected Quincunx wavelet transform, CWT and statistical modelling of Quincunx coefficients using MAP rule for the experiments.

The 3D view of original, noisy and denoised images are presented in Figure 3.10. The 3D view shows that the quincunx denoised image preserves more sharp features as compared to the coiflet denoised image while providing higher PSNR value [24]. Figure 3.11 presents the segmented results of the original gel image after denoising. This analysis shows that an image denoised with quincunx preserves more spots and sharp features and also provides high PSNR values.

**Table 3.1 Mean PSNR values for our set of synthetic images with noise variance 40**

Wavelet family	PSNR values				
	Noisy ( $\sigma = 40$ )	Uni <sup>U</sup> -Soft <sup>S</sup>	Uni <sup>U</sup> -Hard <sup>H</sup>	Bayes <sup>B</sup> -Soft <sup>S</sup>	Bayes <sup>B</sup> -Hard <sup>H</sup>
Haar	19.13	19.201	19.137	19.508	19.175
db1 <sup>D</sup>	19.13	19.201	19.137	19.508	19.175
db2 <sup>D</sup>	19.13	19.218	19.139	19.616	19.195
db3 <sup>D</sup>	19.13	19.225	19.139	19.696	19.196
db4 <sup>D</sup>	19.13	19.223	19.138	19.685	19.198
db5 <sup>D</sup>	19.13	19.22	19.139	19.66	19.223
db6 <sup>D</sup>	19.13	19.226	19.138	19.684	19.202
db7 <sup>D</sup>	19.13	19.231	19.138	19.739	19.202
db8 <sup>D</sup>	19.13	19.228	19.139	19.742	19.2
db9 <sup>D</sup>	19.13	19.23	19.138	19.743	19.218
db10 <sup>D</sup>	19.13	19.228	19.139	19.721	19.202
db11 <sup>D</sup>	19.13	19.225	19.138	19.701	19.19
db12 <sup>D</sup>	19.13	19.228	19.14	19.744	19.211
db13 <sup>D</sup>	19.13	19.225	19.138	19.687	19.196
db14 <sup>D</sup>	19.13	19.232	19.139	19.786	19.203
db15 <sup>D</sup>	19.13	19.229	19.141	19.764	19.204
coif1 <sup>C</sup>	19.13	19.228	19.142	19.707	19.211
coif2 <sup>C</sup>	19.13	19.225	19.14	19.686	19.209
coif3 <sup>C</sup>	19.13	19.23	19.138	19.75	19.207
coif4 <sup>C</sup>	19.13	19.228	19.139	19.731	19.202
coif5 <sup>C</sup>	19.13	19.23	19.138	19.745	19.201
undeci <sup>UN</sup> -coif	<b>19.13</b>	<b>18.92</b>	<b>19.13</b>	<b>24.726</b>	<b>21.726</b>
<b>quincunx</b>	<b>19.13</b>	<b>19.203</b>	<b>19.139</b>	<b>24.497</b>	<b>21.215</b>
<b>undeci<sup>UN</sup>-quincunx</b>	<b>19.13</b>	<b>19.29</b>	<b>19.145</b>	<b>24.498</b>	<b>22</b>

<sup>D</sup> refers to Daubachies wavelet family, <sup>C</sup> refers to coiflet wavelet family, <sup>UN</sup> refers to undecimated.

<sup>U</sup> refers to Universal threshold, <sup>H</sup> refers to hard thresholding, <sup>S</sup> refers to soft thresholding and <sup>B</sup> refers to Bayes threshold.

Table 3.2 Mean PSNR values for our set of synthetic images with noise variance 35

Wavelet family	PSNR values				
	Noisy ( $\sigma = 35$ )	Uni <sup>U</sup> -Soft <sup>S</sup>	Uni <sup>U</sup> -Hard <sup>H</sup>	Bayes <sup>B</sup> -Soft <sup>S</sup>	Bayes <sup>B</sup> -Hard <sup>H</sup>
haar	18.215	18.293	18.224	18.669	18.276
db1 <sup>D</sup>	18.215	18.293	18.224	18.669	18.276
db2 <sup>D</sup>	18.215	18.306	18.228	18.723	18.288
db3 <sup>D</sup>	18.215	18.309	18.226	18.78	18.285
db4 <sup>D</sup>	18.215	18.314	18.225	18.826	18.303
db5 <sup>D</sup>	18.215	18.313	18.227	18.795	18.29
db6 <sup>D</sup>	18.215	18.315	18.227	18.842	18.292
db7 <sup>D</sup>	18.215	18.314	18.224	18.812	18.289
db8 <sup>D</sup>	18.215	18.313	18.224	18.804	18.289
db9 <sup>D</sup>	18.215	18.315	18.225	18.839	18.294
db10 <sup>D</sup>	18.215	18.317	18.225	18.809	18.296
db11 <sup>D</sup>	18.215	18.317	18.226	18.863	18.305
db12 <sup>D</sup>	18.215	18.315	18.226	18.832	18.296
db13 <sup>D</sup>	18.215	18.318	18.224	18.877	18.301
db14 <sup>D</sup>	18.215	18.312	18.226	18.804	18.293
db15 <sup>D</sup>	18.215	18.317	18.225	18.856	18.329
coif1 <sup>C</sup>	18.215	18.312	18.224	18.799	18.288
coif2 <sup>C</sup>	18.215	18.312	18.225	18.794	18.286
coif3 <sup>C</sup>	18.215	18.322	18.228	18.912	18.315
coif4 <sup>C</sup>	18.215	18.314	18.226	18.825	18.297
coif5 <sup>C</sup>	18.215	18.319	18.224	18.844	18.3
undeci <sup>U</sup> -coif	<b>18.215</b>	<b>18.036</b>	<b>18.215</b>	<b>24.259</b>	<b>24.259</b>
<b>quincunx</b>	<b>18.215</b>	<b>18.042</b>	<b>18.217</b>	<b>25.994</b>	<b>25.994</b>
<b>undeci<sup>U</sup>-quincunx</b>	<b>18.215</b>	<b>18.132</b>	<b>18.215</b>	<b>25.996</b>	<b>25.994</b>

<sup>D</sup> refers to Daubachies wavelet family, <sup>C</sup> refers to coiflet wavelet family, <sup>UN</sup> refers to undecimated.

<sup>U</sup> refers to Universal threshold, <sup>H</sup> refers to hard thresholding, <sup>S</sup> refers to soft thresholding and <sup>B</sup> refers to Bayes threshold.

Table 3.3 Mean PSNR values for our set of synthetic images with noise variance 30

Wavelet family	PSNR values				
	Noisy ( $\sigma = 30$ )	Uni <sup>U</sup> -Soft <sup>S</sup>	Uni <sup>U</sup> -Hard <sup>H</sup>	Bayes <sup>B</sup> -Soft <sup>S</sup>	Bayes <sup>B</sup> -Hard <sup>H</sup>
haar	19.089	19.087	19.089	19.09	19.089
db1 <sup>D</sup>	19.089	19.087	19.089	19.09	19.089
db2 <sup>D</sup>	19.089	19.09	19.089	19.089	19.089
db3 <sup>D</sup>	19.089	19.088	19.089	19.092	19.089
db4 <sup>D</sup>	19.089	19.088	19.089	19.09	19.089
db5 <sup>D</sup>	19.089	19.089	19.089	19.089	19.089
db6 <sup>D</sup>	19.089	19.088	19.089	19.09	19.089
db7 <sup>D</sup>	19.089	19.088	19.089	19.09	19.089
db8 <sup>D</sup>	19.089	19.089	19.089	19.089	19.089
db9 <sup>D</sup>	19.089	19.088	19.089	19.09	19.089
db10 <sup>D</sup>	19.089	19.088	19.089	19.091	19.089
db11 <sup>D</sup>	19.089	19.088	19.089	19.091	19.089
db12 <sup>D</sup>	19.089	19.09	19.089	19.089	19.089
db13 <sup>D</sup>	19.089	19.093	19.089	19.09	19.089
db14 <sup>D</sup>	19.089	19.089	19.089	19.089	19.089
db15 <sup>D</sup>	19.089	19.088	19.089	19.09	19.089
coif1 <sup>C</sup>	19.089	19.088	19.089	19.09	19.089
coif2 <sup>C</sup>	19.089	19.089	19.089	19.089	19.089
coif3 <sup>C</sup>	19.089	19.088	19.089	19.09	19.089
coif4 <sup>C</sup>	19.089	19.088	19.089	19.09	19.089
coif5 <sup>C</sup>	19.089	19.092	19.089	19.09	19.089
undeci <sup>U</sup> -coif	<b>19.089</b>	<b>18.875</b>	<b>19.089</b>	<b>24.825</b>	<b>24.825</b>
<b>quincunx</b>	<b>19.089</b>	<b>18.896</b>	<b>19.091</b>	<b>26.727</b>	<b>26.727</b>
<b>undeci<sup>U</sup>-quincunx</b>	<b>19.089</b>	<b>18.742</b>	<b>19.099</b>	<b>26.779</b>	<b>26.779</b>

<sup>D</sup> refers to Daubachies wavelet family, <sup>C</sup> refers to coiflet wavelet family, <sup>UN</sup> refers to undecimated.

<sup>U</sup> refers to Universal threshold, <sup>H</sup> refers to hard thresholding, <sup>S</sup> refers to soft thresholding and <sup>B</sup> refers to Bayes threshold.

Table 3.4 Comparison of denoising methods for synthetic images

Denoising method	PSNR for $\sigma = 30$	PSNR for $\sigma = 35$	PSNR for $\sigma = 40$
Haar	19.09	18.669	19.508
Db4	19.09	18.826	19.685
Db8	19.089	18.224	19.742
Coif5	19.09	18.844	19.745
CWT	21.9117	20.5685	20.455
Stat model non-sep 3 ML	13.8198	11.8871	12.1289
Stat model non-sep 5 ML	13.234	13.0922	14.4185
Stat model non-sep 7 ML	15.2677	16.1639	17.6132
Stat model non-sep 3 MAP	13.6741	12.8589	13.93
Stat model non-sep 5 MAP	14.5517	14.9573	17.6191
Stat model non-sep 7 MAP	15.8101	18.0118	18.539
Stat model sep 3 ML	13.0538	13.6073	13.2114
Stat model sep 5 ML	12.9319	15.0316	15.1652
Stat model sep 7 ML	14.8654	15.634	18.7651
Stat model sep 3 MAP	13.7946	14.9153	16.5375
Stat model sep 5 MAP	14.3198	16.8008	17.5125
Stat model sep 7 MAP	16.1233	17.1369	17.5231
<b>quincunx</b>	<b>26.727</b>	<b>25.994</b>	<b>24.497</b>
<b>undeci-quincunx</b>	<b>26.779</b>	<b>25.996</b>	<b>24.498</b>

Stat Model refers to statistical model, non-sep refers to nonseparable, sep refers to separable, ML refers to Maximum

Likelihood, MAP refers to Maximum a posteriori probability and number N represents neighborhood (3x3, 5x5 etc).

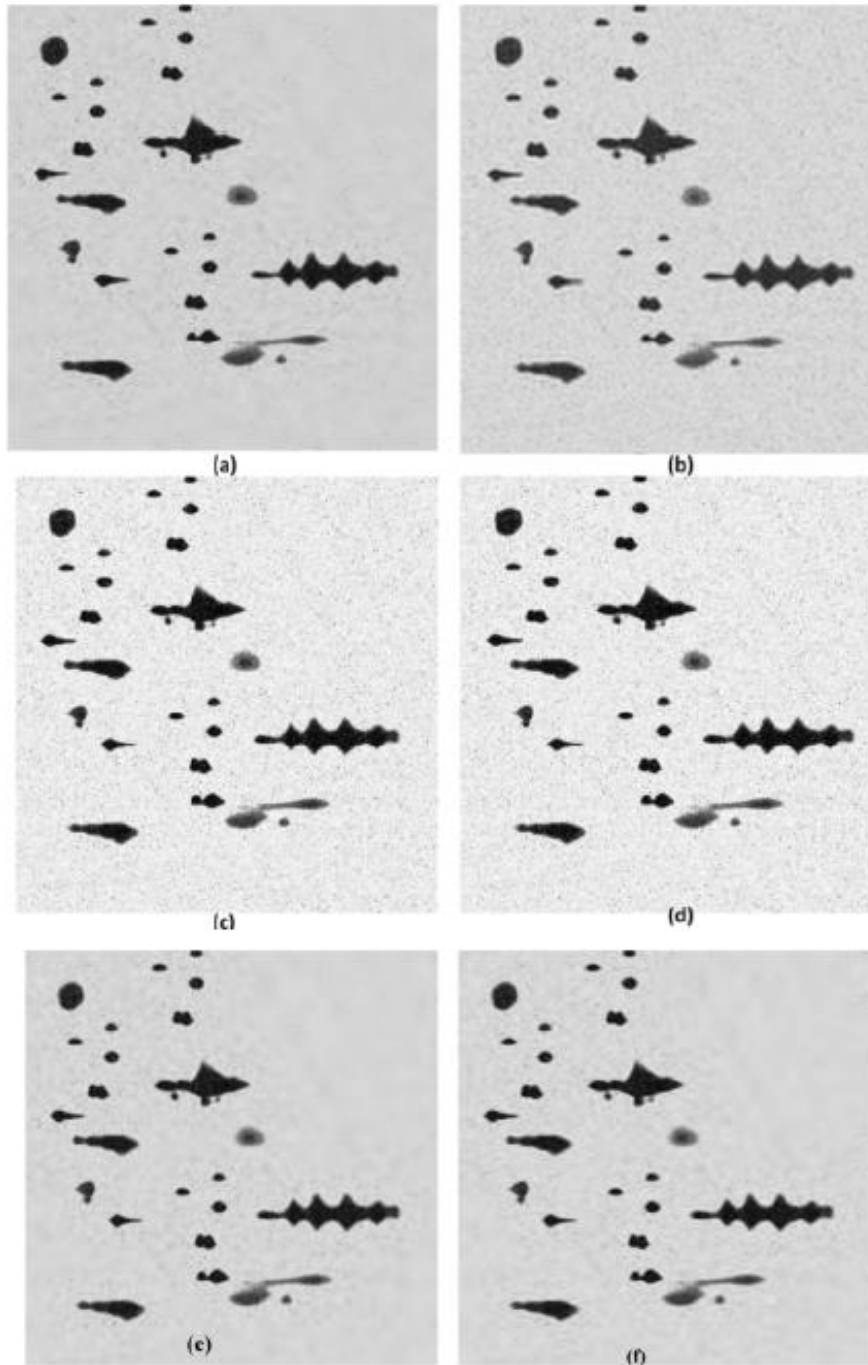


Figure 3.9: Denoised Synthetic Images using (a) CWT with BayesShrink (b) Quincunx with BayesShrink (c) Coif5 with BayesShrink (d) Db8 with BayesShrink (e) Statistical Model on Quincunx coefficients with 7x7 window (MAP rule) (f) Statistical Model on db8 coefficients with 7x7 window(MAP rule)

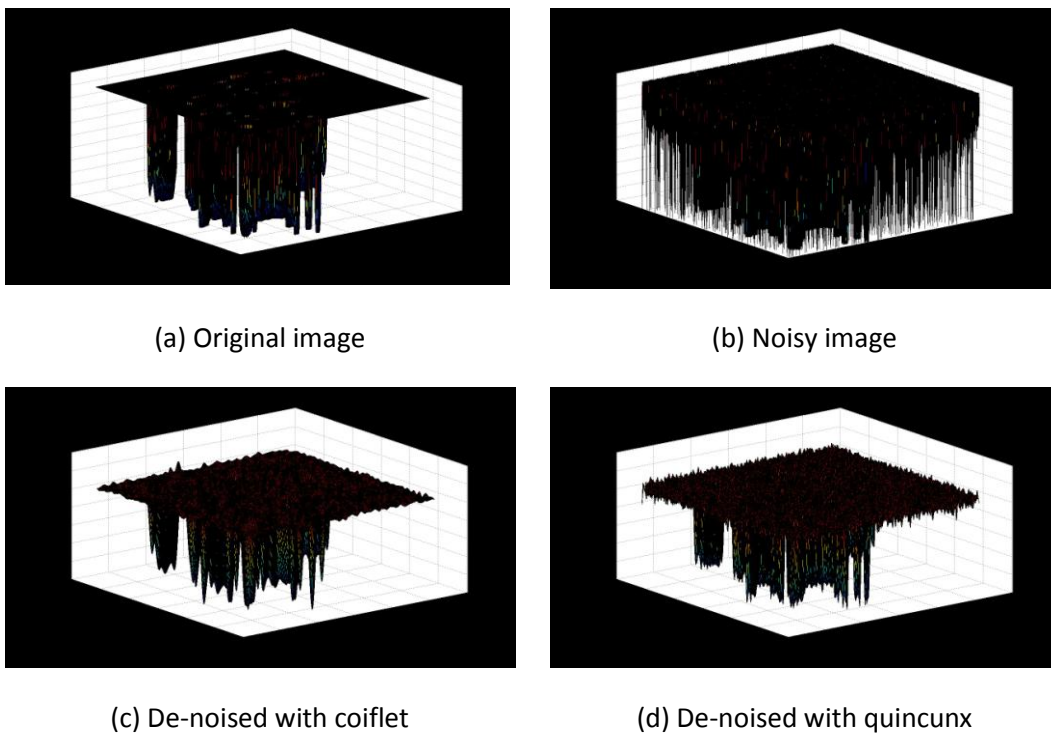


Figure 3.10: 3D view of synthetic images.

Image denoised with quincunx preserves more spots and sharp features

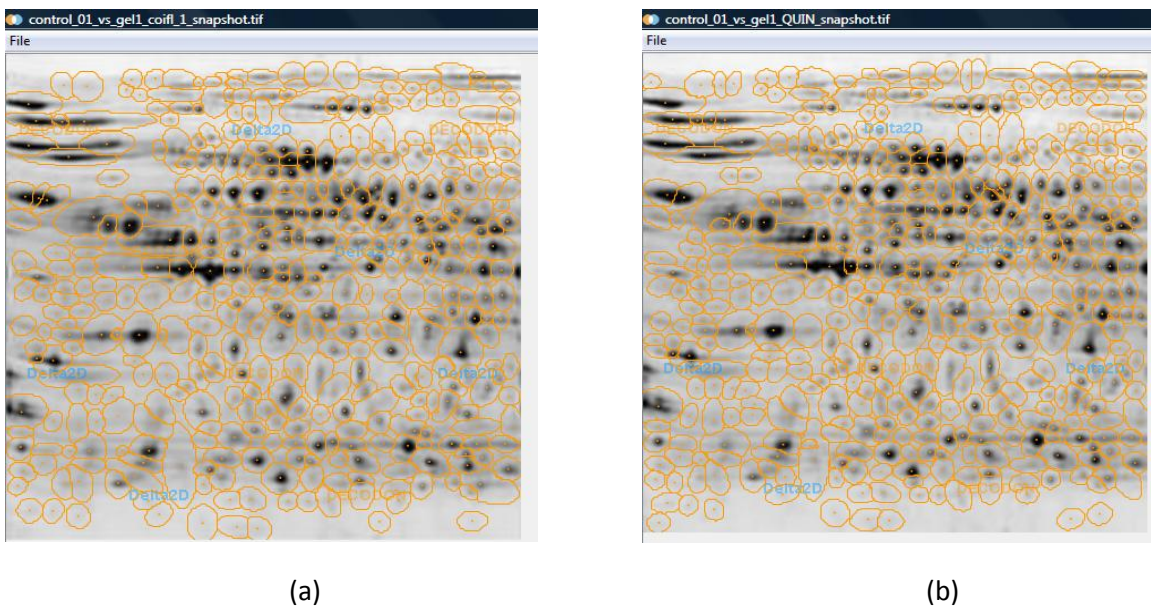


Figure 3.11: De-noised images are processed through Delta2D package. Segmented images are shown.

(a) image denoised by coiflet and processed. Total 412 spots are detected out of 457 true spots. (b)

image denoised by quincunx and processed. Total 446 spots are detected out of 457 true spots.

## Chapter 4 Segmentation of Low-resolution 2DGE Images

### 4.1 Introduction

Image segmentation is a fundamental and non-trivial task in image processing for high-level object analysis, object tracking, quantitative measurement and detection of a region of interest. For this purpose, the researchers have discovered several methods which can be broadly classified into two categories: discontinuity based methods and similarity based methods. Discontinuity based methods rely on the gradient information of the image and are thus more susceptible to noise. The similarity-based methods divide the image into different regions based on some predefined similarity criteria. These methods consider a large region in the calculation and are assumed to be less susceptible to the noise. Such methods are usually based on region growing approaches [51], fuzzy approaches [52]-[54], region-based active contours [55] [56] etc. In many applications, the objects usually consist of either darker or lighter regions of the image [51]-[57].

Image segmentation of 2D gel images is not a trivial task due to the presence of varying intensities in foreground and background regions. The presence of streaks, low-intensity spots and artifacts make the task quite challenging. The general purpose segmentation methods [51]-[57] usually fail to give satisfactory results. Therefore, researchers have devised many specific methods [6]-[21] [58]-[66] for extraction of protein spots from the 2D gel images. Some researchers conceptualized the idea of grouping of pixels through hierarchical thresholding [10], local variances [7], watershed [9] or combinations of it [10]. Active contour-based method [55] is also used in 2D gel image segmentation for finding accurate spot boundary at the cost of high computational complexity. The watershed-based approach described by Dos Anjos *et al.* [12] provides a more plausible segmentation of the spots, even when the spots are cluttered in a

limited area. The method is able to segment overlapping spots and produces very less number of artifacts. During our experiments, we found that this method is more robust to noise in comparison with other methods. Another advantage of this method is the relatively easier tuning of its parameters. Based on the literature review and our previous experiments, it can be argued that watershed transform is good to divide the image into homogenous regions while wavelet transform is good at detecting the singularities.

We have proposed a segmentation algorithm which combines properties of wavelet transform and watershed algorithm for getting better results. This segmentation algorithm finds the spots in each watershed region by studying singularities in that region. Even though this method outperforms the commercial software, it possesses some weaknesses. The scale of the image at which watershed transform is applied affects the result significantly. This segmentation method is described in section 4.2.

A second segmentation algorithm without watershed transform is devised to overcome weakness possessed by the first segmentation method. A novel interscale ratio between the wavelet coefficients is used to extract the protein spot regions from the background. Then, spot boundaries are found by applying an edge detector. This segmentation method is described in detail in section 4.3.

To summarize, the following segmentation methods have been proposed in this chapter:

1. Segmentation using Wavelet Transform and Watershed Transform
2. Segmentation using Wavelet Interscale Ratios

## 4.2 Method using Wavelet Transform and Watershed Transform

### 4.2.1 Watershed Transform and Problems

The watershed transform [9] is a powerful tool for medical image segmentation. It is a region growing algorithm that analyzes an image as a topographic surface. The gray level 'h' of a pixel (x, y) of the image becomes the elevation 'h' of a point (x, y, h). In this way, the image surface can be seen as full of mountains and valleys. Let us pierce a hole in all local minima and immerse it into a lake. Water will fill up the valley starting at these local minima, and at all points where water coming from two or more valleys meets, dams are built. As a result, the surface is partitioned into different regions separated by dams. The regions so formed are called catchment basins and the dams are called watershed lines. Numerous techniques have been proposed to compute the watershed [67] [68]. The advantage of the watershed approach is that it produces closed, adjacent and accurate contours. However, the watershed transform often leads to over-segmentation. There are two main approaches in the literature to overcome this problem. The first is region merging [67], i.e. merge the adjacent region according to some similarity criteria. Images containing large and nonlinear variations in intensities of pixels often lead to poor results due to the difficulty of choosing optimized and varying similarity criteria. Gel images are typical examples of non-stationary signals and the region merging approach does not yield satisfactory results on these gel images. Another approach to overcoming over-segmentation is the use of markers [68]. A marker is a connected component of an image. Internal markers are associated with the objects of interest and external markers are associated with the background. These markers are imposed as minima on the image and all other minima are suppressed. Then the watershed algorithm is applied to the image. The disadvantage of this method is that the accuracy of the result depends on upon the accurate placements of markers

and the number of markers. For a gel image containing irregular spots with varying intensities, it is mostly difficult to find out accurate markers.

#### 4.2.2 Proposed Segmentation Method

Spot characteristics have been analyzed in the watershed and wavelet domains. First, a watershed transform is applied on a low-resolution image of the same size and regional information is imposed onto the original image. The low-resolution image is used to reduce over-segmentation, which is also beneficial in reducing processing requirements. The resolution should not be too low as it causes problems in spot detection. The image is segmented into homogeneous regions called catchment basins (CB). Let  $\{m_k\}$  be the minima of image  $I$  and  $\{CB(m_k)\}$  be the associated catchment basins. Each catchment basin may contain spots as well as a background. We define two subsets within catchment basins as follows:

**Definition 1:** Let  $F$  and  $B$  be two subsets in a catchment basin  $CB(m_k)$  such that  $F \cap B = \emptyset$ . We say  $F$  is a set of pixels belonging to the spots of image  $I$ , if

- (1) For any  $(x_f, y_f) \in F$  and any  $(x_b, y_b) \in B$ ,

$$I(x_f, y_f) < I(x_b, y_b) \quad (4.1)$$

where  $I(x, y)$  denotes the gray value of pixel  $p(x, y)$  in the image  $I$ .

- (2) There exists an optimal 'h', such that threshold of  $I$  at level  $h$  is defined as

$$T_h(I) = \{p | I(p) < h\} \quad (4.2)$$

and

$$F = CB(m_k) \cap T_h(I) \quad (4.3)$$

It is clear from definition 1 that to distinguish F from other parts of the image I, we need to find out the optimum value of h.

Image I is further decomposed using the undecimated quincunx wavelet transform and detail coefficients  $W_j$  at scale j are given by

$$W_j(x, y) = I * \psi_j(x, y) \quad (4.4)$$

where  $\psi_j$  is a wavelet at scale j and \* denotes the convolution.

To de-correlate the noise across wavelet scales, we introduce the term “scale product” as follows:

**Definition 2:** The scale product  $P_{j,j+1}$  shows the correlation between wavelet coefficients of adjacent scales j and j+1 and is defined as

$$P_{j,j+1}(x, y) = W_j(x, y) \cdot W_{j+1}(x, y) \quad (4.5)$$

Watershed catchment basins are mapped onto  $P_{j,j+1}$  and corresponding to each  $CB(m_k)$ , coefficients of  $P_{j,j+1}$  are found and denoted as  $S_{j,j+1}(m_k)$ . Now connected maxima set for  $S_{j,j+1}(m_k)$  is defined as follows:

**Definition 3:** A connected maxima set  $CM_i(m_k)$  is a collection of those coefficients  $\{c_q\}$  of  $S_{j,j+1}(m_k)$  which satisfy any of the following criteria:

(1)

$$c_q = \{\max_j(c_j) | c_j \in (S_{j,j+1}(m_k) - \cup_{l \neq i} CM_l(m_k))\} \quad (4.6)$$

or

(2)  $c_q$  is in the neighborhood of  $CM_i(m_k)$  and it is the largest of its neighbors. Also,  $c_q$  has at least  $(k-2)$  neighbors having a value less than it (assuming  $k$ -neighborhood operation).

In the set  $S_{j,j+1}(m_k)$ , there may be more than one connected maxima set. Horizontal and vertical connected maxima sets are identified using the following definition.

**Definition 4:** A connected maxima set  $CM_i(m_k)$  is a horizontally connected maxima set  $HCM_i(m_k)$  if  $\exists \epsilon > 0$  such that  $\forall c_q \in CM_i(m_k)$  and  $\forall c_p \in CM_i(m_k)$ ,  $|y_{c_q} - y_{c_p}| < \epsilon$ . Similarly, a connected maxima set is a vertical connected maxima set  $VCM_i(m_k)$  if  $\exists \epsilon > 0$  such that  $\forall c_q \in CM_i(m_k)$  and  $\forall c_p \in CM_i(m_k)$ ,  $|x_{c_q} - x_{c_p}| < \epsilon$ , where  $(x_{c_q}, y_{c_q})$  is coordinate of  $c_q$  in  $P_{j,j+1}$ . (We are taking  $\epsilon = 1$  in our experiments.)

The vertical and horizontal connected maxima sets are less likely to be the features of a spot, therefore, these are neglected and the union of the connected maxima set is defined as follows:

$$UCM(m_k) = \cup_{\forall i} \{CM_i(m_k) | \forall j, CM_i(m_k) \neq HCM_j(m_k) \text{ and } CM_i(m_k) \neq VCM_j(m_k)\} \quad (4.7)$$

The coefficient  $c_{max}$  which has the maximum value among the coefficients of all connected maxima sets in  $UCM(m_k)$  is selected.

$$c_{max} = \max\{c_q | c_q \in UCM(m_k)\} \quad (4.8)$$

Let us denote the coordinates of  $c_{max}$  in  $P_{j,j+1}$  as  $(x_{c_{max}}, y_{c_{max}})$ . Now, the threshold of  $I$  at level 'h' introduced in definition 1 can be found out. A simple strategy is used for determining the optimal value of 'h' and it gives accurate results. The strategy is stated as follows:

$$h = \{I(x, y) | I(x, y) \in CB(m_k), x = x_{c_{max}}, y = y_{c_{max}}\} \quad (4.9)$$

After this, pixels can be clearly classified as a member of either F or B.

For any subset  $X \subseteq CB(m_k)$  in the image  $I$ , the corresponding scale product coefficients  $Coeff(X)$  are found as:

$$Coeff(X) = \{c_q | c_q \in S_{j,j+1}(m_k), c_q = P_{j,j+1}(x_{c_q}, y_{c_q}) \text{ and } I(x_{c_q}, y_{c_q}) \in X\} \quad (4.10)$$

where  $(x_{c_q}, y_{c_q})$  are the coordinates of the coefficient  $c_q$  in the scale product  $P_{j,j+1}$ .

The mean  $M(X)$  and the  $k^{\text{th}}$  order center moment  $\mu_k(X)$  of the wavelet coefficients corresponding to a subset  $X \subseteq CB(m_k)$  is calculated as follows:

$$M(X) = \frac{1}{\text{numel}(X)} \left[ \sum_i (Coeff_i(X)) \right] \quad (4.11)$$

$$\mu_k(X) = \frac{1}{\text{numel}(X)} \left[ \sum_i (Coeff_i(X) - M(X))^k \right] \quad (4.12)$$

Where  $\text{numel}(X)$  is the number of elements in the subset  $X$  and  $Coeff_i(X)$  is the  $i^{\text{th}}$  element of the set  $Coeff(X)$ .

To distinguish between artifacts and spots, a simple criterion based on the second and the third order center moments have been formulated. According to this, if the second and/or the third order moments of  $F$  are more distinguishable than that of  $B$ , then  $F$  can be considered as a true spot. The criterion has been successfully used in our experiments and can be stated as follows:

$$\text{Dist}(F, B) = \sqrt{\left[ (\mu_2(F) - \mu_2(B))^2 + (\mu_3(F) - \mu_3(B))^2 \right]} \quad (4.13)$$

For a catchment basin  $CB(m_k)$ , if  $\text{Dist}(F, B) > T$ , then  $F$  is considered as a spot, otherwise it is considered as an artifact (where  $T$  is a single threshold used for each catchment basin).

### 4.2.3 Experiments and Results

The methodology is depicted in Figure 4.1. The image is first denoised using the quincunx wavelet transform [24]. Then the quincunx wavelet transform is once again applied to the denoised image up to the decomposition level  $J=3$ . The low-resolution image at scale  $J$  is used for watershed segmentation and detail components of scale 2 and 3 are used for computing the scale product. The post-processing step involves morphological operations (erosion followed by dilation using a disk-shaped structure) to remove the remaining streaks and to improve the results. 8-bit gray level images of size 1024 x 1024 and of size 512 x 512 have been used. Segmentation results achieved by our method are more accurate than those obtained from popular commercial software like Delta2D. The segmentation result of a gel image is shown in Figure 4.2. The results of commercial software including Delta2D depend on three or more sensitivity parameters. As an advantage, our method uses a single threshold parameter. This method is also employed to detect faint spots but artifacts pose problems as they do when using commercial software. The number of artifacts (false spots) and missing spots has been found to be less as compared to Delta2D. Missing spots include the spots that are not detected at all or that are detected as a part of other spots. False spots are the artifacts detected by the software since they pass all conditions of the software/methods to prove themselves as spots. In Figure 4.3, a part of the gel image has been shown with missing spots and false spots. To compare our method with Delta2D, we define the ‘spot efficiency’ factor as follows:

$$\text{spot efficiency} = \frac{\text{Total spots detected} - \text{No. of False spots}}{\text{Total spots detected} + \text{No. of Missed spots}} \quad (4.14)$$

Clearly, if the number of false spots or missing spots is more, spot efficiency will be low. For a method, spot efficiency will be 1 (100%) if and only if no false spot is detected and no real spot is missed. Table 4.1 summarizes the results using the proposed method and using Delta2D.

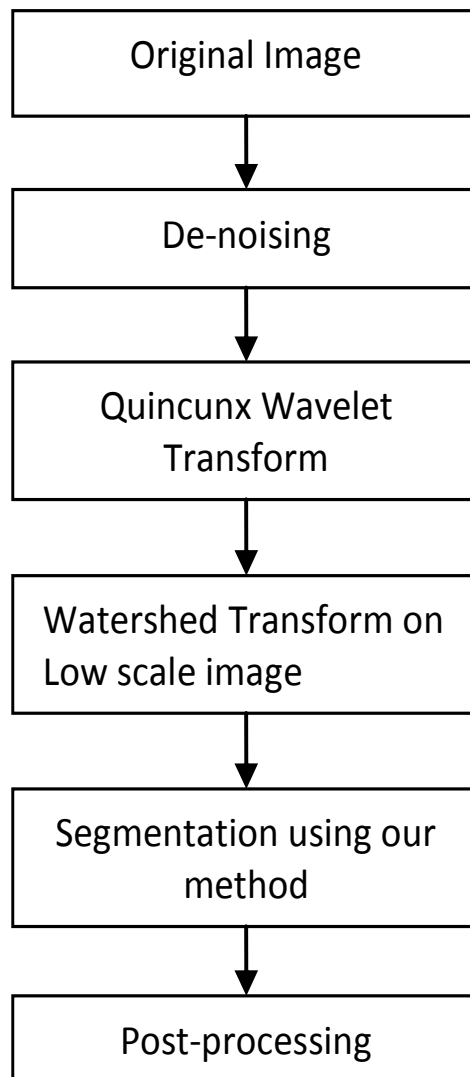
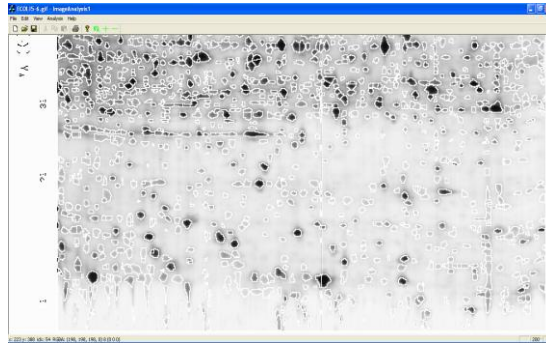
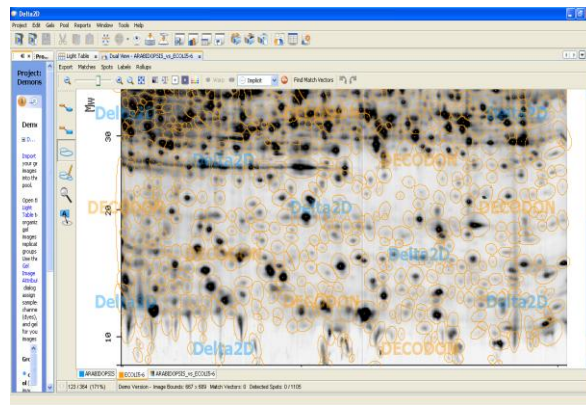


Figure 4.1: Block diagram of proposed segmentation approach



(a) Using the proposed method



(b) Using Delta2D

Figure 4.2: Segmented Spots

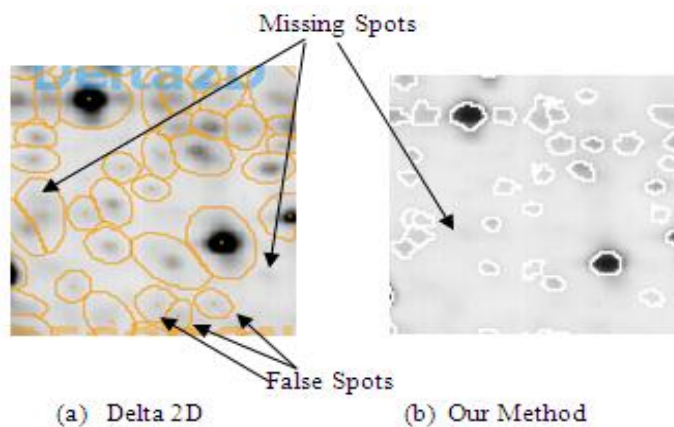


Figure 4.3: A part of gel image showing some missing spots and false spots using Delta2D and using the proposed method

**Table 4.1 Results in terms of ‘spot efficiency’**

	<b>Our Method</b>	<b>Delta2D</b>
Image1	96%	94%
Image2	94%	91%
Image3	96%	93%
Image4	91%	87%
Image5	97%	95%

### **4.3 Method using Wavelet Interscale Ratios**

In this section, we propose a second novel approach for segmentation of 2DGE images in the nonseparable wavelet domain. The discrimination power (DP) of each denoised wavelet coefficient is quantitatively measured at each scale for better detection of the faint spots. The proposed inter-scale relationship among the DPs provides sufficient information to characterize and to segment the image into its distinct components: the region of the spots, the background and the edges. The probability measure that describes the extent to which a wavelet coefficient belongs to the spot surface is calculated based upon the derived interscale relationship. A single threshold on the probability map is sufficient to extract the regions of the real spots. An energy distribution model has been used to remove the edges associated with artifacts without using any threshold. The oversaturated spots are difficult to analyze using the above method. Therefore, a separate algorithm is presented to detect all the oversaturated spots in the gray value image. Finally, the experimental results are presented and it is found that our method outperforms the commercial software and other available techniques.

### 4.3.1 Proposed Image Model

An observed gel image,  $I$ , contains the original noise-free image  $I'$  and noise  $n$ :

$$I = I' + n \quad (4.15)$$

The noise free image  $I'$  contains the edges and interiors of the protein spots. So, the image model in equation (4.15) becomes:

$$I = (t + e + b) + n \quad (4.16)$$

Here,  $t$  represents the interiors of all the spots and  $e$  represents the edges of all the spots present in the gel image and  $b$  represents image. The presented method in this chapter separates out each component of the image model. The gray scale image  $I$  is normalized between 0 and 1.

### 4.3.2 Image Decomposition

The 2DGE image is decomposed using a nonseparable wavelet [69] scheme. Based on the lifting scheme [70], the quincunx interpolating filter bank having two primal and two dual vanishing moments, designed by Kovacevic and Sweldens [70] has been used. The undecimated version of the transform is used here since the same size of the image is obtained at each scale and it is easy to analyze the inter-scale relationship. For the undecimated version, we remove the decimation operator from the quincunx lifting scheme [70] and the  $N$ -times quincunx upsampled versions of predict and update filters are used, where  $N$  represents the decomposition level. In this way for higher decomposition levels, the corresponding filter support widens.

### 4.3.3 LMMSE Based Denoising

To separate out the noise, denoising of the gel image is performed. Linear minimum mean squared error estimation (LMMSE) based noise filtering method [71] is applied to the wavelet

coefficients. When a nonseparable undecimated Quincunx wavelet transform is applied to the observed image  $I$ , all singularities due to image components and noise are captured.

$$WT(I) = WT(I') + WT(n) \quad (4.17)$$

The noise free wavelet coefficients are assumed to be conditionally independent zero mean Gaussian random variables, given their variances  $\sigma^2$  [71]. The noise is assumed to be additive white Gaussian noise with variance  $\sigma_n^2$ . Thus, the noise free wavelet coefficients can be calculated as follows:

$$\widehat{wt}_j^k = \frac{\hat{\sigma}^2(k)}{\hat{\sigma}^2(k) + \sigma_n^2} wt_j^k \quad (4.18)$$

Where  $\hat{\sigma}^2$  denotes the maximum likelihood (ML) estimate of the local variances  $\sigma^2$  and is computed from the observed wavelet coefficients as follows [34]:

$$\hat{\sigma}^2(k) = \max \left\{ 0, \frac{1}{\#\Omega_k} \sum_{\beta \in \Omega_k} (wt_j^\beta)^2 - \sigma_n^2 \right\} \quad (4.19)$$

Where  $wt_j^\beta$  represents the wavelet coefficients at scale  $j$  and location  $\beta$ ,  $\Omega_k$  represents the set of coefficients in the square neighborhood window centered at location  $k$  and  $\#$  denotes the number of the elements in the set. The standard deviation of noise  $\sigma_n$  can be estimated using the wavelet coefficients at the finest scale ( $j=1$ ) as follows:

$$\sigma_n = \frac{\text{median}(|wt_j^k|)}{0.6745}, \quad j = 1 \quad (4.20)$$

where  $|\cdot|$  denotes the absolute value.

### 4.3.4 Discrimination Power of the Wavelet Coefficients

The significant singularities in the images are captured by the wavelet domain coefficients [31]. These wavelet coefficients  $\{\widehat{wt}_j^k\}$  represent the singularities due to the protein spots and the background. The singularities due to the spots include the singularities due to the interior regions and the edges of the spots. The high valued and sparse wavelet coefficients at a scale mostly represent the edges of the spots along with the strong edges in the background, while the low valued coefficients may represent the singularities due to the interiors of the spot, the faint edges of the spots or the background. We term this “power” of the wavelet coefficients as ‘Discrimination Power’ (DP). Based upon the value of the wavelet coefficients, these different types of the singularities can be discriminated up to some extent. Thus, to measure the DP quantitatively, the distribution of the wavelet coefficients as shown in Figure 4.4 is utilized. By observing the area beneath the histogram curve ( $h(\cdot)$ ), the DP for an arbitrary wavelet coefficient ( $w$ ) is defined as:

$$DP(w) = \int_0^w h(u) du \quad (4.21)$$

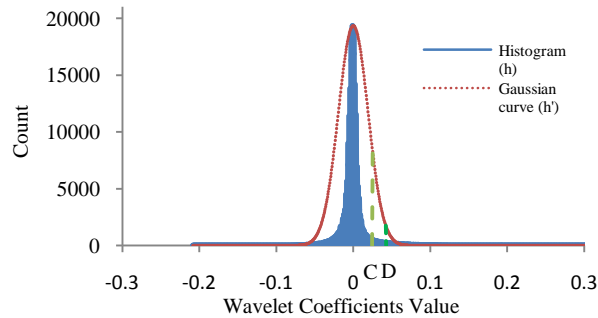


Figure 4.4: the histogram of the wavelet coefficients is plotted along with a Gaussian curve for comparison and measurement of DP values

The histogram of the wavelet coefficients has a sharp peak and is symmetric (see Figure 4.4). Therefore, each side of the histogram curve can be represented by  $h(\cdot)$ . Mallat [31] [33] experimentally found that the histogram curve can be estimated by:

$$h(u) = Ke^{-\left(\frac{u}{\alpha}\right)^\gamma} \quad (4.22)$$

where  $K$  is a normalization constant,  $\alpha$  measures the variance and  $\gamma$  models the decreasing rate of the peak. These parameters can be calculated as described by Mallat [28].

Discrimination among the low wavelet coefficients is still difficult using the above definition of DP. Since the DP is measured using the area beneath the curve  $h(\cdot)$ , two given wavelet coefficients such as C and D showed in Figure 4.4 would be better discriminated if the measuring curve is modified to have slower decay and broader peak. That said, the measuring curve will still be able to capture the trend of the distribution of the wavelet coefficients up to some extent. By assuming that the wavelet coefficients corresponding to the edges and interior region of the faint spots are normally distributed, the modified function in the simplified form can be written as:

$$h'(u) = Ke^{-u^2} \quad (4.23)$$

i.e.  $\alpha = 1$  and  $\gamma = 2$ . So, the DP of a wavelet coefficient can be written as follows:

$$DP(\widehat{wt}_j^k) = \int_0^{\widehat{wt}_j^k} h'(u) du = K \int_0^{\widehat{wt}_j^k} e^{-u^2} du \quad (4.24)$$

The constant  $K$  is set to  $2/\sqrt{\pi}$  to make  $\int h'(u) du = 1$ . Thus, the DP is measured by the error function *erf* as follows:

$$DP(\widehat{wt}_j^k) = \text{erf}(\widehat{wt}_j^k) \quad (4.25)$$

There are two main properties of the DP:

1) *Fixed Range*: The measured DP of any wavelet coefficient at any scale falls within the same range [-1, 1], so it can easily be compared across scales.

2) *Enhancement*: The *erf* function is a sigmoid shaped function. The measured DP slightly enhances the “power” of the low wavelet coefficients. Slight suppression of the power of the very large wavelet coefficients does not reduce the chance of getting them discriminated due to their sparse nature.

### 5.3.5 Discrimination among Spot Region, Edge and Background

Mallat [31] has found that the wavelet coefficients corresponding to significant singularities are evolved across scales when scale increases as follows:

$$\dots > \widehat{wt}_{j+1}^k > \widehat{wt}_j^k > \widehat{wt}_{j-1}^k \dots \dots > \widehat{wt}_1^k, \quad k \in K \quad (4.26)$$

where  $K$  is the set of locations of wavelet coefficients corresponding to the edges. From equation (4.24) and (4.25), it is obvious that the DP of the wavelet coefficients corresponding to the edges will also grow across scales while scale increases. Also, the DP of the wavelet coefficients corresponding to the interior of spots will decay across scales. Thus, to find consistent and complete discrimination information for the interior region of spots, the edges and the background, the evolution of the DP across scales is captured using their inter-scale ratios and is known as Inter-scale Discrimination Information (IDI).

$$IDI^k = \frac{1}{n - m + 1} \sum_{j=m}^n \frac{1 + DP_{j+2}^k}{1 + DP_j^k} \quad (4.27)$$

To get a better estimate of the IDI, alternate scales  $-j$  and  $j+2$  are used, since they represent the detail images at the same orientations for the quincunx wavelet decomposition.

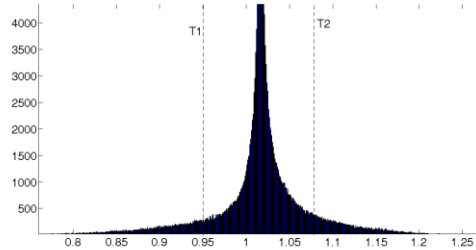


Figure 4.5: The pdf of IDI and two threshold levels T1 and T2.

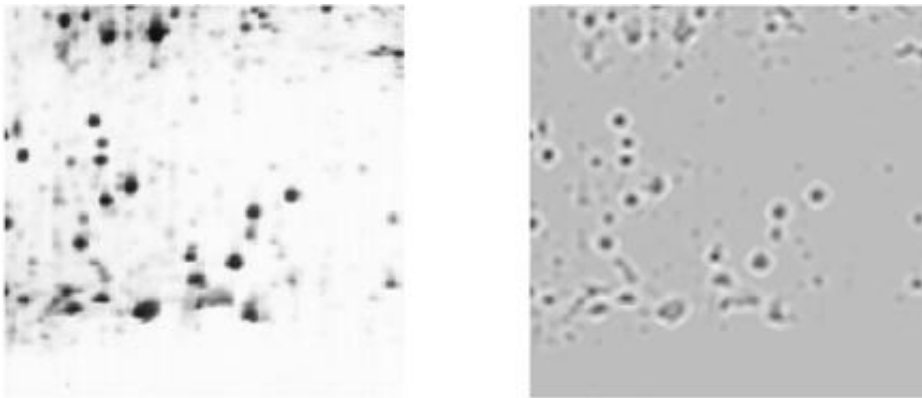


Figure 4.6: A real 2D gel image with protein spots (left) and corresponding IDI values (right). The dark colors indicate low values and bright colors indicate high values.

The probability density function (pdf) of the IDI for a real gel image is shown in Figure 4.5. In Figure 4.6, the protein spots from the gel image have been depicted along with its IDI. The pdf of the IDI has a sharp peak at the centre. Different parts of the pdf of the IDI reflect the different parts of the protein spot. The coefficients of IDI falling on the left side of the peak of the pdf denote the interiors of the spots. On the other hand, the coefficients of the IDI falling on the right side of the peak represent the edges and surrounding area of the edges of the spots. The part of the pdf of the IDI having values near its peak value represents the background area. The

two thresholds, as shown in Figure 4.5, are used to extract these different components of the image. For clear visibility, the tricolor image for different parts of the pdf of the IDI has also been presented in Figure 4.7. We have studied this nature of IDI on several 2D gel images and verified that it is a persistent pattern. Thus, we can conclude that the proposed IDI is able to distinguish between the different components of our image model in equation (4.16).

Some drawbacks of the IDI are: In the case of a single or overlapping oversaturated spots, almost all the center part of the object contains high IDI values as shown in Figure 4.8. Also, the edges are thick and not clearly distinct for cluttered regions of the spots (see Figure 4.9). Even having such drawbacks, the spots can be detected using the interior information provided by IDI as subsequently described.

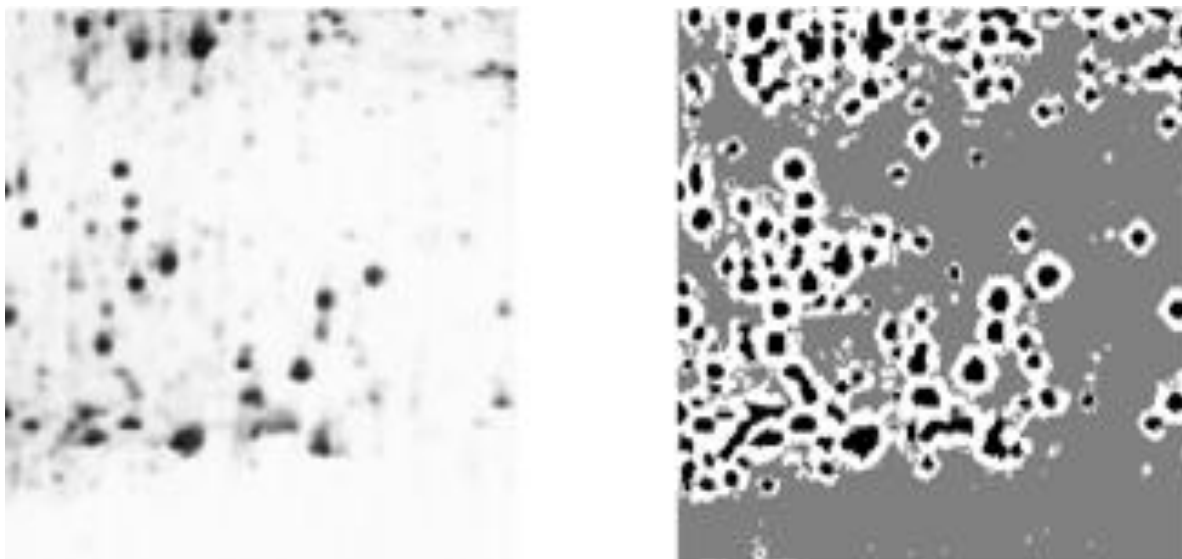


Figure 4.7: The tricolor image (right) of IDI values of protein spots and corresponding original image (left). Black colors indicates interiors ( $IDI < T1$ ), white color indicates edges ( $IDI > T2$ ) and gray color indicates background ( $T1 < IDI < T2$ ).

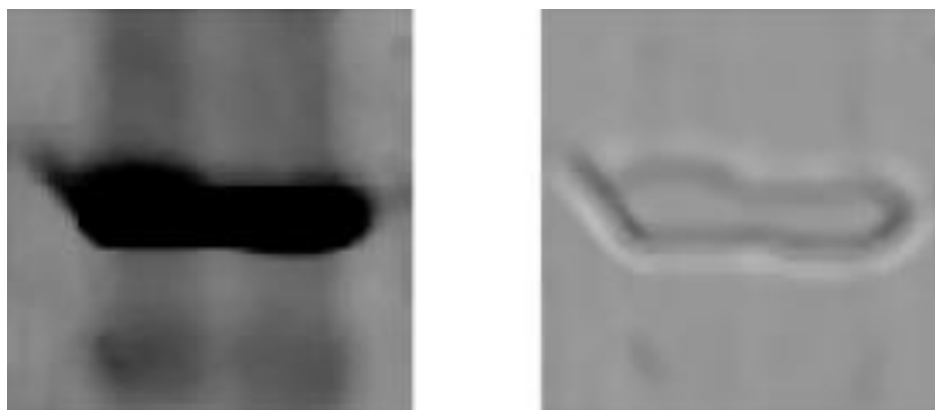


Figure 4.8: The oversaturated spots (left) and corresponding IDI values (right). In right image, bright color indicates high IDI values.

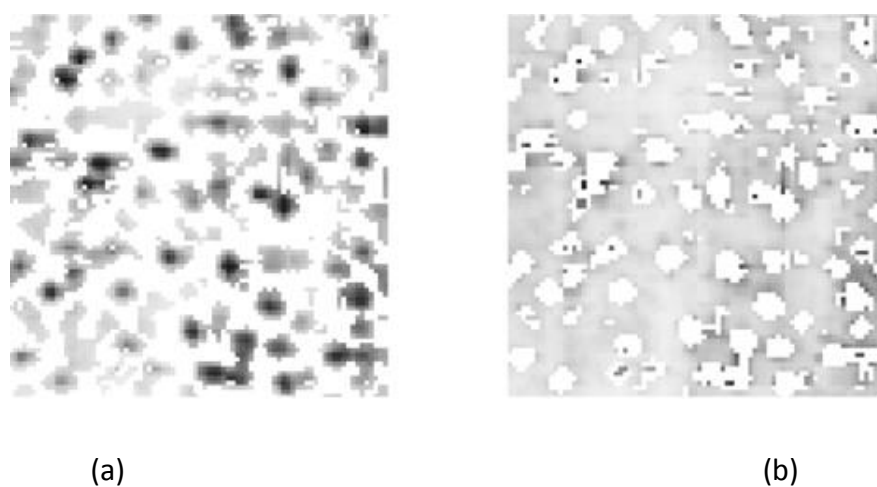


Figure 4.9: (a) The edge information from IDI ( $IDI > T_2$ ) is overlaid on the corresponding part of the real gel image. (b) The interior information ( $IDI < T_1$ ) is overlaid on the same part of the real gel image.

#### 4.3.6 Texture Characterization and Spot Detection

The part on the left of the peak of the pdf of IDI represents the interior information. The coefficient at a larger distance from the peak and on the left side of the peak has a larger probability of being a good candidate to carry interior information of the spots. In wavelet

domain, texture is usually characterized using  $L^1$  norm or  $L^2$  norm of the wavelet coefficients. The local texture at a location can be defined as the sum of the  $L^1$  norm or  $L^2$  norm of wavelet coefficients in a local window. Here, we define the local texture as a summation of IDI coefficients in a local window. The probability  $itp(k)$  of the  $k^{\text{th}}$  IDI coefficient being a good candidate to carry texture information of the spots is called ‘Inter-scale Texture Probability’ (*ITP*) and defined as follows:

$$itp(k) = \frac{1}{\#\Omega_k} \sum_{\beta \in \Omega_k} p\left(1 - \frac{IDI^\beta}{mean(IDI)}\right) \quad (4.28)$$

where,

$$p(\xi) = \begin{cases} median(\xi) & \text{if } \xi \geq 0 \\ 0 & \text{otherwise} \end{cases} \quad (4.29)$$

$\Omega_k$  denotes the neighborhood of  $k^{\text{th}}$  IDI coefficient and  $\beta$  denotes a member of  $\Omega_k$ .  $mean(IDI)$  denotes the mean value of all IDI coefficients. Negative probability has no meaning, and all negative probabilities are replaced with a value zero using  $p(\xi)$ . The median operator on  $p(\xi)$  within  $3 \times 3$  neighborhoods is used to cope with the erroneous very high or very low values in the IDI. A real 2D gel image and its corresponding ITP have been depicted in Figure 4.10. All the spot regions in the ITP can be easily extracted using a global threshold,  $ITP_{MIN}$ . This threshold ( $ITP_{MIN}$ ) indicates the minimum acceptable probability for the spots in a probability map.  $ITP_{MIN}$  should be selected carefully. A low value of  $ITP_{MIN}$  will include many background pixels and a high value of  $ITP_{MIN}$  may exclude many foreground pixels. Based upon the experiment on our set of images, 2% i.e. 0.02 is set as the default value for most of cases considered in this thesis.

The binary image built by thresholding its ITP by  $ITP_{MIN}$  is also depicted in Figure 4.10. It can easily be observed that this binary image consists of the region of all the spots of the gel

image. For comparison, the gray value original image is also thresholded using a popular global threshold method called 2D Otsu [13]. As shown in Figure 4.10, the binary image formed by 2D Otsu threshold contains a lot of the background area. The binary image formed by thresholding ITP contains fewer background pixels and contains all the spot regions. Also, it can be noted that the image which is given in Figure 4.10(a) cannot be correctly segmented with any gray level threshold value. If the threshold value is reduced, less number of background pixels will be included but many foreground pixels will also be lost. Figure 4.11 depicts this situation. Thus, for a 2D gel image containing inhomogeneous background, our method gives precise and fairly accurate information. Since the single global threshold  $ITP_{MIN}$  is used to discriminate the foreground regions from the inhomogeneous background, it clearly indicates that the ITP representation overcomes the inhomogeneity of the 2D gel image up to a very large extent. Also, this threshold does not vary across the different sets of gel images used in our experiments.

The boundary of the faint spots as well as other spots can easily be found either using the directional local maxima of the first derivative of the ITP or using the zero-crossing of a second derivative detector such as Laplacian of Gaussian (LoG). In either case, thresholds are not used to remove irrelevant edges. Since a few regional maxima of backgrounds may have high ITP values, spurious edges around the corresponding regions may be found. These spurious edges will be eliminated using a non-threshold based method presented in the next subsection. The region enclosed by an edge need not necessarily belong to a single spot. It may belong to multiple overlapped spots. In the case of multiple overlapped spots, multiple regional maxima may occur in the region. As the 3D profile of ITP for a spot is bell-shaped or mountain shaped (see Figure 4.12), the inverse profile of the ITP will look like valleys, where each spot belongs to

separate valleys. Therefore, the watershed method [9] is applied to the gradient image of the ITP. The obtained watershed line will define the border between the individual spots.

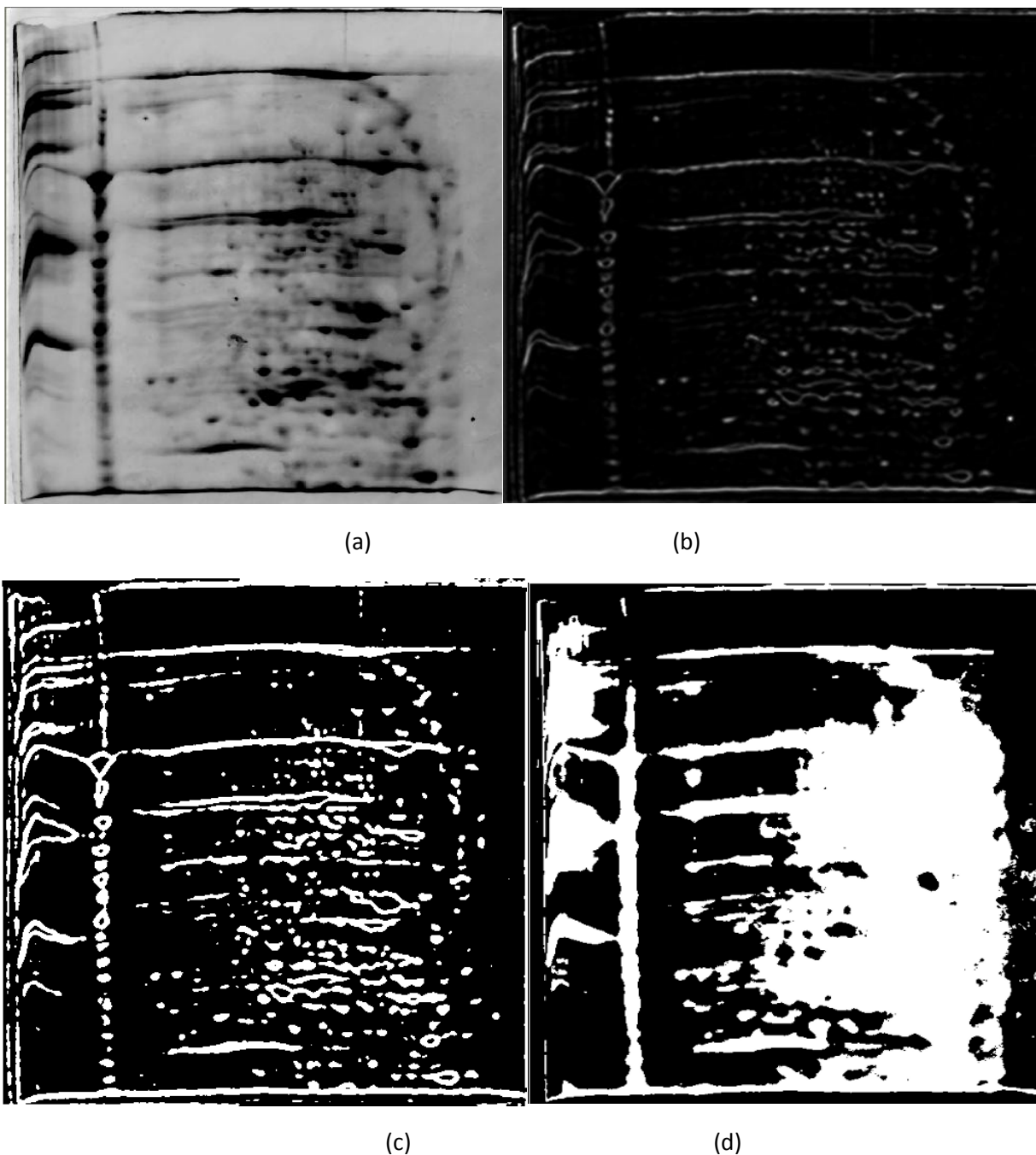


Figure 4.10: (a) An original 2D gel image with (b) its ITP, (c) its binary image made by  $ITP \geq 0.02$  and (d) its binary image obtained using global 2D Otsu threshold on gray value image.

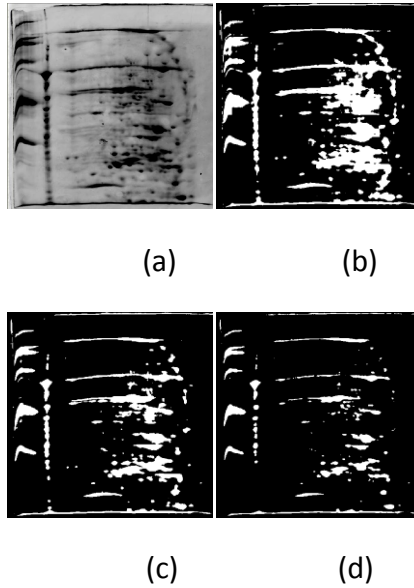


Figure 4.11: (a) A 2D gel image. (b), (c) and (d) its binary images obtained through applying different gray value thresholds (b) 100 (c) 75 and (d) 25 respectively.

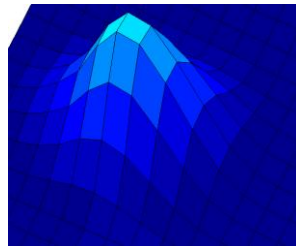


Figure 4.12: 3D profile of ITP of a typical faint spot

### 4.3.7 Energy Distribution Model

The 2DGE method is used to separate out the proteins of a sample based on their molecular weights and isoelectric points. An electric force is applied in one dimension to separate the proteins based on their isoelectric points. Then, another electric force is applied in a perpendicular direction to separate the proteins based upon their molecular weights. For the purpose of simulation, we assume that both forces act simultaneously. In this process, the proteins move to separate out until their charges are neutralized. After attaining this stable state,

they lose most of their energy and possess minimum energy. Thus, the energy in the 2DGE is distributed in such a way that the protein spots have minimum energy as compared to their surroundings. We assume that the energy variables are independent and identically distributed random variables following the Gaussian distribution. The ITP is a good tool to describe a 2DGE image, so based upon it, a weighted Gaussian model for describing the energy distribution in the 2D gel is derived as follows:

$$E(k) = \frac{1}{\sqrt{2\pi}\sigma_k} \exp\left(-\sum_{\beta \in \Omega_k} W_k(\beta) \frac{(itp(\beta) - \mu_k)^2}{2\sigma_k^2}\right) \quad (4.30)$$

The local mean  $\mu_k$  and local variance  $\sigma_k^2$  for the  $k^{\text{th}}$  coefficient of ITP is calculated within neighborhoods  $\Omega_k$ .  $W_k$  is an adaptive weighting function which depends upon the local behavior of ITP at location  $k$ . The weighting function  $W_k$  makes the energy function more robust against the background variations that have remained. The weighting function  $W_k$  is defined as a zero mean Gaussian as follows:

$$W_k(\theta) = \frac{1}{\sqrt{2\pi}\lambda_k} \exp\left(-\frac{\theta^2}{2\lambda_k^2}\right) \quad (4.31)$$

The size of the neighborhood  $\Omega_k$  in equation (4.30) depends upon the maximum spread of the weighting function  $W_k$ . Since  $W_k$  is chosen to be a Gaussian, the size of the neighborhood  $\Omega_k$  is chosen as  $4*\lambda_k+1$ .  $\lambda_k$  is selected in such a way that it makes the uneven area smoother and at the same time, avoids smoothing on the edges. So, if  $\sigma_k$  is high,  $\lambda_k$  should be low, and when  $\sigma_k$  is low,  $\lambda_k$  should be high. Thus, these are inversely related to each other. Moreover, the value of  $\lambda_k$  should fall sharply in comparison with  $\sigma_k$  to avoid smoothing on faint edges. The  $\lambda_k$  and  $\sigma_k$  can be related as:

$$\lambda_k = \lambda_{max} \exp\left(-\frac{\widehat{\sigma}_k^2}{\widehat{\sigma}_{max}^2}\right) \quad (4.32)$$

where

$$\widehat{\sigma}_{max} = \max\{\widehat{\sigma}_k\}, \quad \forall k \quad (4.33)$$

$$\lambda_{max} = \rho \widehat{\sigma}_{max} \quad (4.34)$$

where the constant  $\rho$  is experimentally determined for 2D gel images. The estimated value of variance  $\widehat{\sigma}_k$  is calculated using a 3 x 3 neighborhood of ITP.

After calculating the energy distribution  $E(\cdot)$ , the location of the spots can be found out by detecting the local minimum of  $E$ , i.e. by finding the energy region for which

$$\partial^2 E / \partial k^2 > 0 \quad (4.35)$$

The spurious edges detected in the previous subsection can be removed since they do not fall into the minimum energy region. Only the edges which either completely or partially fall into the minimum energy regions are preserved.

#### 4.3.8 Oversaturated Spots

The oversaturated spots have a high concentration of proteins throughout their surface and this result in minima plateaus in the image. Overlapping oversaturated spots remain a problem for detection using the methods available in the literature, mostly due to lack of separate regional minima for each spot. A separate method is needed to detect and separate them. Our proposed method from the previous subsections is also not sufficient for overlapped oversaturated spots since multiple regional maxima of ITP occur around the boundary as shown in Figure 4.13(a).

These high contrast oversaturated spots can easily be detected in the gray value image using a region growing method.

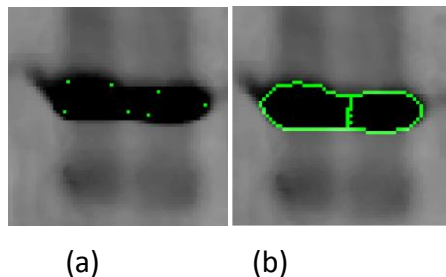


Figure 4.13: (a) An oversaturated spot with multiple regional maxima of ITP on its boundary. (b) The segmentation of the overlapped oversaturated spots.

The regional minima of the gray scale image are calculated. Oversaturated spots will occur on minima plateaus. All regional minima having a size less than a minimum (say  $S_{min}$ ) and gray value higher than a threshold ( $Th_{high}$ ) are discarded to make sure we get the minima plateaus of the oversaturated spots. The parameter  $S_{min}$  is experimentally determined as 9, which is less than or equal to the minimum spot size in the gel image. The threshold  $Th_{high}$  is required to avoid background minima plateaus. Remaining minima plateaus represent the initial spot regions  $\{R_i\}$  for oversaturated spots. In the region growing method, a pixel  $p$  in the neighborhood of  $R_i$  is added to the region  $R_i$ , if the value of gradient at  $p$  is not less than the value of gradient at any nearest pixel of  $R_i$ . In this way, the oversaturated spots are extracted from the gray value image.

To calculate the value of threshold  $Th_{high}$ , it is assumed that there are only a small number of oversaturated spots in the image. It is further assumed that oversaturated spots will not usually cover usually more than 2% area of gel image. An image containing many large oversaturated spots is usually considered a difficult image for analysis in the literature. Therefore, our assumption is not very far from the reality and  $Th_{high}$  can be calculated as

$$Th_{high} = \max\{ g \mid count(I < g) \leq OPC \} \quad (4.36)$$

where  $count(I < g)$  gives the count of total pixels in the image having gray value less than  $g$  and  $OPC$  (oversaturated pixel count) is 2% of total pixels in the image. The  $OPC$  is not a very sensitive parameter in spot detection. It only determines which spots can be categorized as oversaturated spots. Experimentally, it can be shown that a low value of  $OPC$  (less than 2% of total number of pixels) may miss the detection of a few oversaturated spots, but a high  $OPC$  value (such as 2% of total number of pixels) can detect all oversaturated spots and also many other spots which are already detected using our wavelet based method described above in this chapter. Therefore, a high  $OPC$  value changes only categorization of already detected spots and declares them as oversaturated spots. Since categorization of spots does not matter in the final segmentation result, a high  $OPC$  value fulfills our segmentation's purpose. It can also be observed that a very high  $OPC$  value (more than 10% of total number of pixels) may detect background minima plateau as oversaturated spot regions and diminish its purpose.

The oversaturated spots detected in the above step may be overlapped. Therefore, the separation of the overlapped spots is the next necessary step. In the absence of any intensity variation in the oversaturated spots, the Euclidian distance transform is a good choice. The distance transform is applied to the binary image formed by the detected oversaturated spots as foreground. The regional maxima of the distance transform is considered as the centroid of the objects in the binary image and an object having more than one centroid needs to be separated into individual subsets (spots). The watershed method is applied on the inverse of the distance transform to find out the boundary between overlapped spots. Figure 4.13(b) shows the boundary between overlapped oversaturated spots.

Only the spots, for which corresponding ITP values are less than  $ITP_{MIN}$ , are required to be preserved. In this manner, the oversaturated spots are extracted from the gray value image and processed separately and efficiently.

#### **4.3.9 Overall Strategy**

In the previous subsections, we have presented a method to detect the protein spots from 2D gel images. The presented wavelet based scheme is able to detect the faint spots. Based on the presented work so far, the overall algorithm for the segmentation of a 2D gel image can be described using the following steps:

- 1) Decompose the normalized gray value gel image  $I$  using the undecimated quincunx wavelet.
- 2) Do LMMSE based denoising on the wavelet coefficients as described in Section 4.3.3.
- 3) Calculate the ITP using equation (4.28).
- 4) Perform edge detection on ITP.
- 5) Separate the overlapped spots and discard the regions pertaining to thin streaks and noise using morphological opening operation using a disk shaped structuring element having a diameter similar to the estimated diameter of the smallest spot in the image.
- 6) Find out the minimum energy regions in the gel image using equations (4.30) and (4.35).
- 7) Discard those edges which do not fall partially or completely in the detected minimum energy region.

- 8) Detect the oversaturated spots in the original gel image using the method described in Section 4.3.8.
- 9) Merge both the results of step 7 and step 8 by discarding the regional maxima and the edges that fall into the spatial coordinate regions of the oversaturated spots. This gives us the final segmentation result.

## **4.3.10 Experimental Results and Discussions**

### **4.3.10.1 Data Set**

To evaluate the performance of the method presented in this paper, several experiments were conducted on 8-bit real and synthetic 2D gel images of size 512 x 512. The high-resolution images are resized to 512 x 512 to reduce computational time. The ground truth of 2DGE images is difficult to find and depends on the consensus of the subjective evolution by expert biologists. Therefore, for quantitative and qualitative evaluation, we created some synthetic images and also used the real 2DGE images available in the public database.

### **4.3.10.2 Parameter Settings**

The parameters in the proposed method have been determined once and remain the same throughout the experiments. The neighborhoods in equation (4.19) are found out using a 3 x 3 window. To calculate inter-scale discrimination information in equation (4.27), the scale parameters  $m$  and  $n$  are set as 2 and 3, respectively. These values of  $m$  and  $n$  will cover the scale range 2 to 5 in equation (4.27). The noise predominates at the scale 1 therefore, it is omitted while on the other hand, at a higher scale, the support of the wavelet becomes very large and poses problems in the discrimination of nearby singularities in our set of images. The scale

ranges 2 to 5 seem appropriate for our set of images. A larger scale range is required in high-resolution images since wavelet support should match the minimum spot size at lower scales and the maximum spot size at higher scales. This restriction is required to capture the properties of the whole region of the spot. But the larger scale range will increase the computational complexity, therefore, it is advised to apply the method to the image of reduced size and then map the result back to the high-resolution image. For mapping, the segmented binary result can be resized to the full size of the original image and then using the resized binary image can be used to mark the spot region. For better accuracy, a marker-controlled watershed can be applied to extract the boundary of spots.

The minimum probability of the ITP,  $ITP_{MIN}$ , is an important parameter which affects the accuracy of the segmentation results. Figure 4.14 depicts the final segmentation result with the different values of  $ITP_{MIN}$  on a real gel image taken from the public database. A low value of  $ITP_{MIN}$  includes more background pixels as depicted in Figure 4.14. Therefore, to include minimum background pixels, an optimal value of  $ITP_{MIN}$  can be found for each image. We have found that in the majority of cases, a value  $ITP_{MIN} = 2\%$  (i.e. .02) gives satisfactory results. Therefore, in all our experiment (including the image shown in Figure 4.14), this value is used and we have found that it is able to cover all the regions corresponding to the faint spots. The value of the constant  $\rho$  in equation (4.34) is experimentally determined as 10. The values of the parameters related to the detection of the oversaturated spots are already discussed along with the method in Section 4.3.8.

### 4.3.10.3 Results and Comparisons

The method proposed in this chapter has been applied on the gel images of our data set. For a comparative analysis, our method is compared with popular commercial software ImageMaster 7 (also known as ImageMaster 7) and a published method in the literature by dos Anjos et al. [12]. The parameters of the proposed approach have been kept constant throughout the experiments while the parameters of the commercial software and the method by dos Anjos et al. [12] were adjusted for each image in order to maximize the detection of the true spots. The author implementation of the method by dos Anjos et al. [12] – named “SCIMO” is used in our experiment.

A real gel image and its segmentation results have been depicted in Figure 4.15. SCIMO method paints the border of spots with yellow color, which is not clearly visible in Figure 4.15. Therefore, a part of the same gel image and corresponding results are selected and zoomed for better visibility (see Figure 4.16). It can be observed that ImageMaster 7 seems to include more background pixels within the spot boundaries while boundaries produced by SCIMO seem to be more rectangular. The proposed method produces more plausible spot boundaries. For quantitative analysis, ten synthetic images were created. Since most of the spots in real gel images can be modeled using 2D Gaussian or 2D flat Gaussian, the synthetic images contain several 2D Gaussian spots along with 2D flat Gaussian spots in inhomogeneous background extracted from real gel images using a large size (typically, 50 x 50) mean operator. Some synthetic images also contain several spots with tails and small streaks. Figure 4.17 and Figure 4.18 show the segmentation results of two synthetic images. It can clearly be observed that our method produces more plausible spot boundaries.

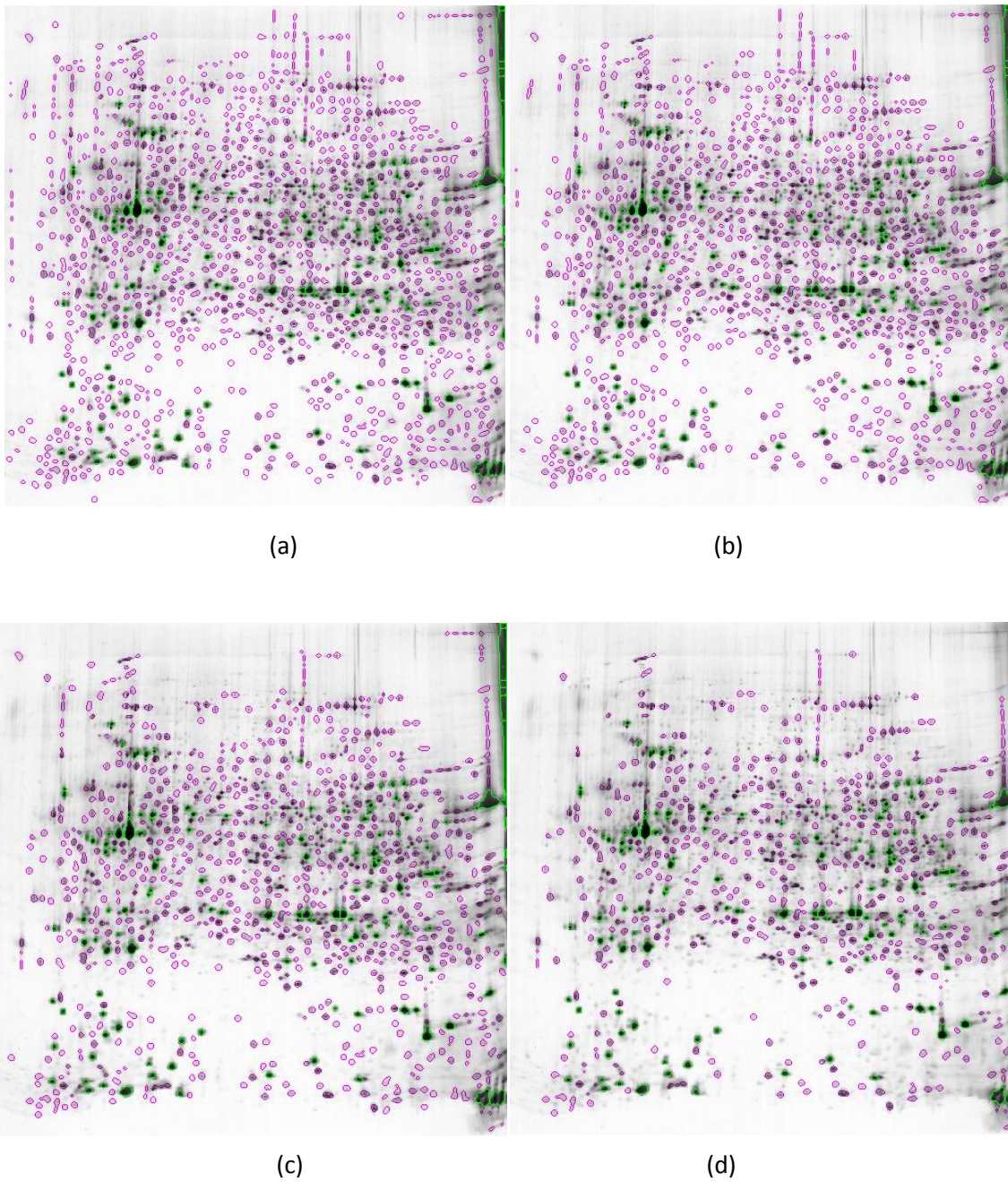
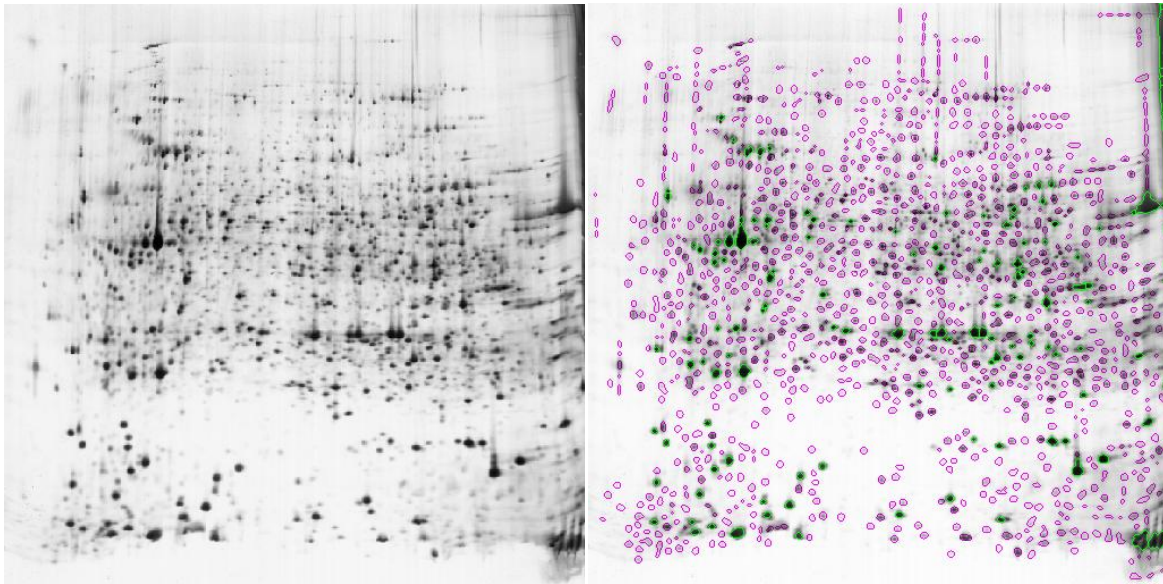


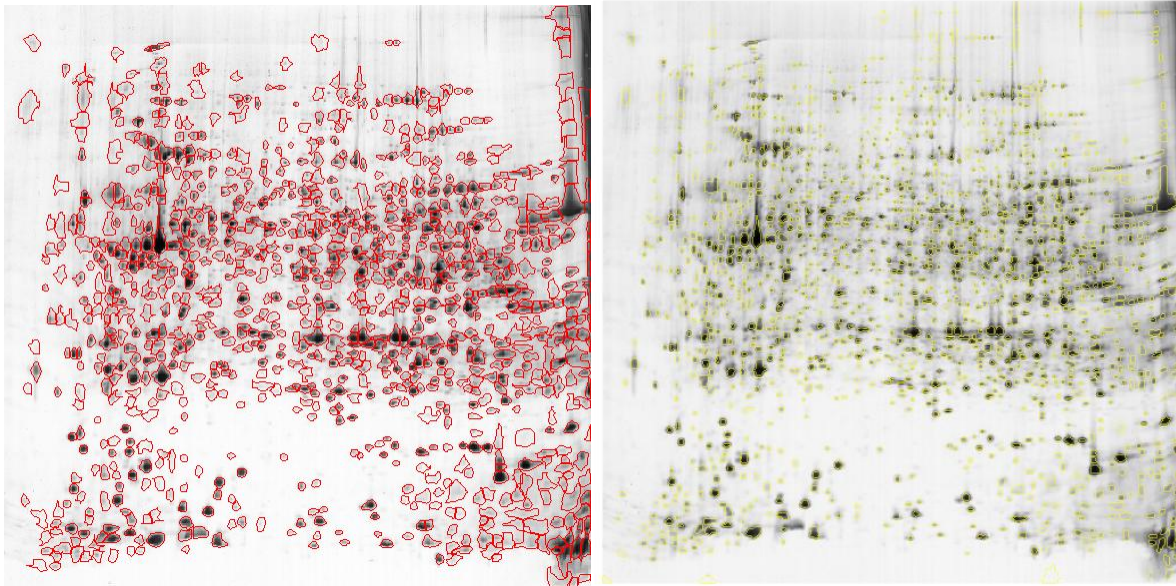
Figure 4.14: Effect of different values of  $ITP_{MIN}$  on the segmentation result of a real gel image. (a)

$ITP_{MIN} = 1\%$  (b)  $ITP_{MIN} = 2\%$  (c)  $ITP_{MIN} = 5\%$  and (d)  $ITP_{MIN} = 10\%$ . Spots identified as the oversaturated spots are depicted with green border and the rest of the spots are depicted with a pink border.



(a)

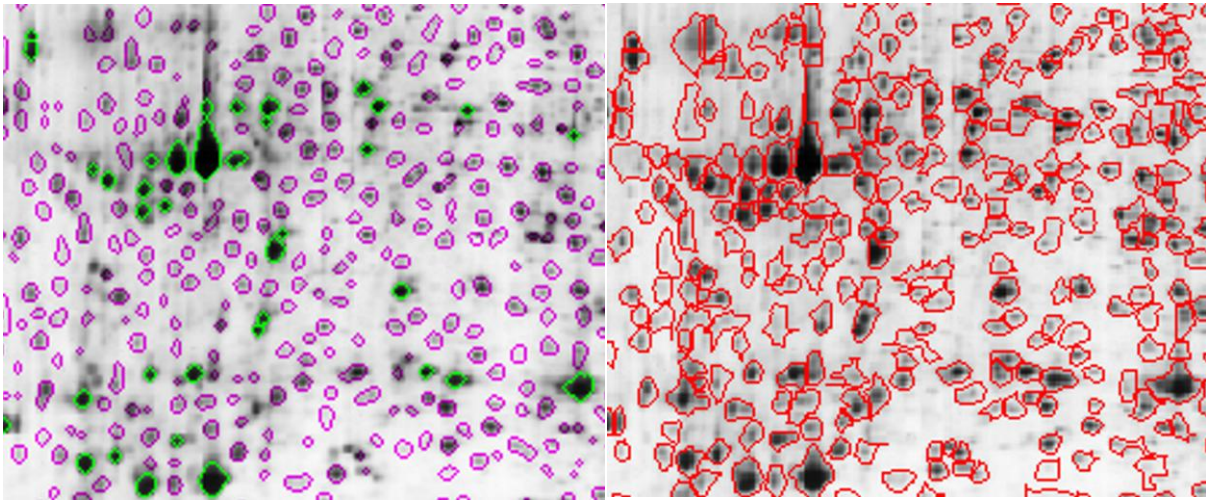
(b)



(c)

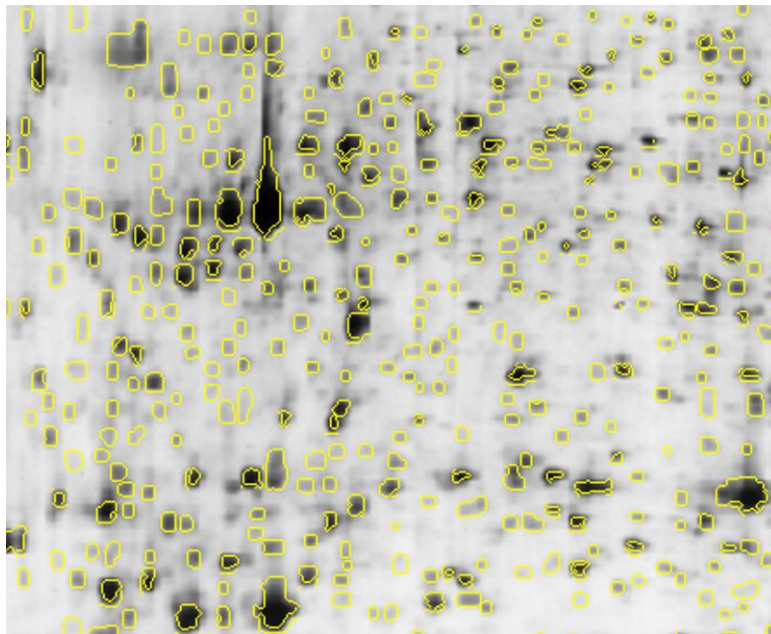
(d)

Figure 4.15: (a) a real gel image from public dataset [77] and segmentation results using (b) Proposed method (c) ImageMaster 7 and (d) SCIMO.



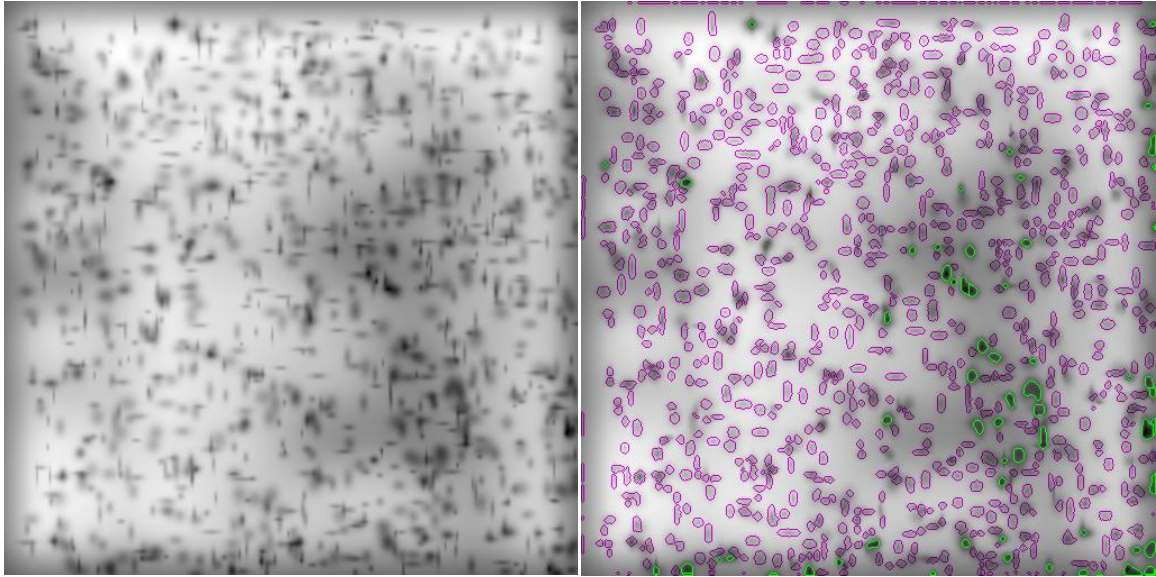
(a)

(b)



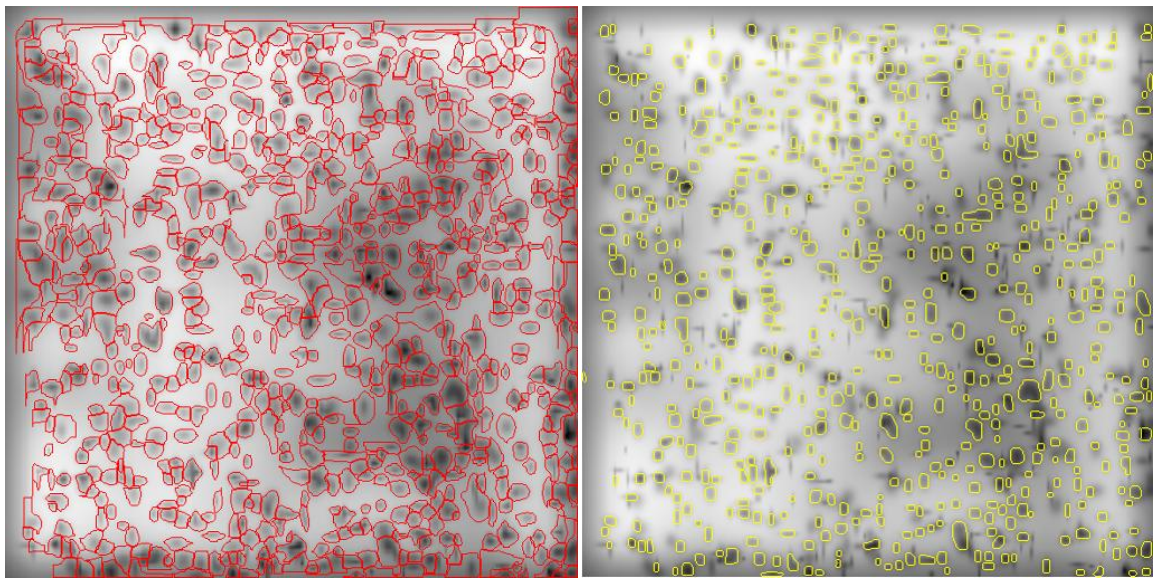
(c)

Figure 4.16: A part of the image and results shown in Figure 5.15(b, c, d) is selected and zoomed for better visibility. (a) Result by Proposed method (b) Result by ImageMaster 7 and (c) Result by SCIMO.



(a)

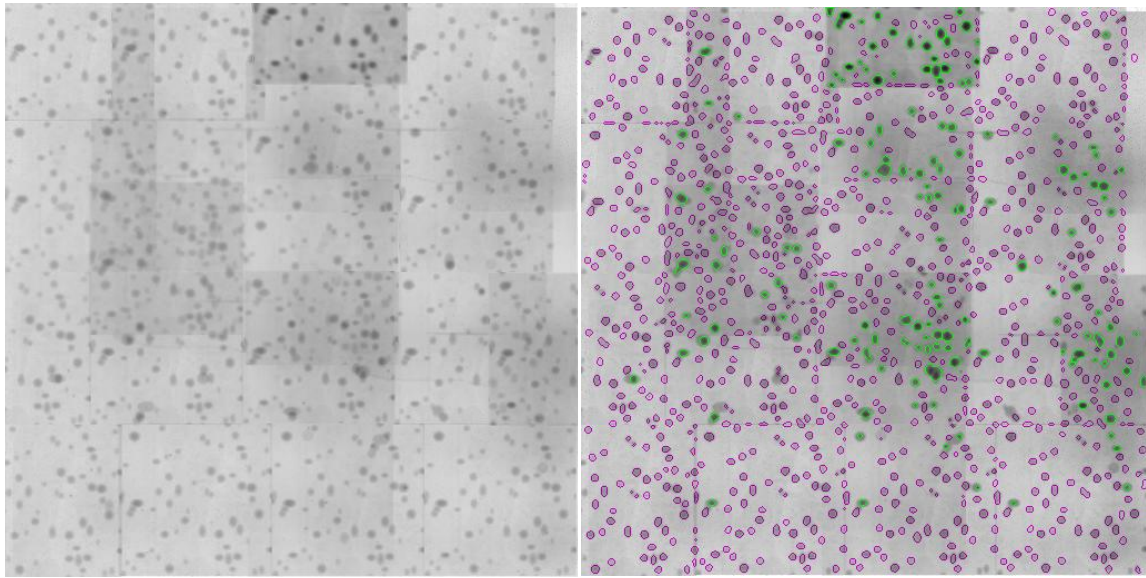
(b)



(c)

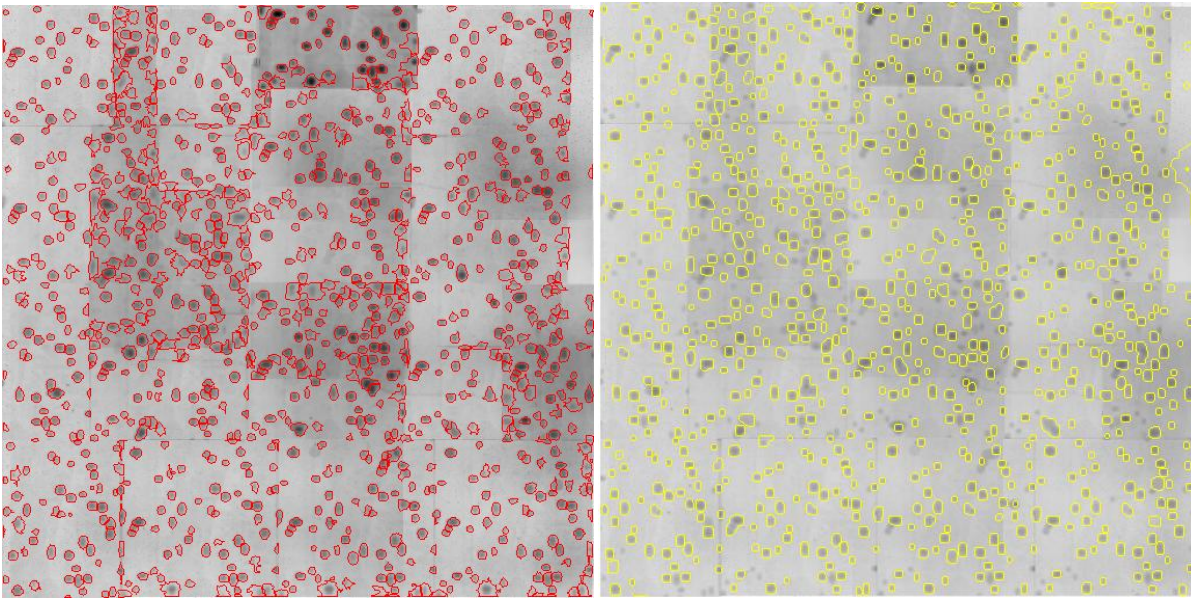
(d)

Figure 4.17: (a) A synthetic image and its segmentation using (b) Proposed method (c) ImageMaster 7 and (d) SCIMO.



(a)

(b)



(c)

(d)

Figure 4.18: (a) A synthetic image and its segmentation results using (b) Proposed method (c) ImageMaster 7 and (d) SCIMO.

While generating synthetic images, their ground truth images have also been carefully generated. To compare the segmentation results, a measure of foreground pixels overlap between ground truth and the result can be a good parameter for evaluation. Each detected spot area is compared with its ground truth spot area and mean error in spot area for all spots is measured as:

$$Err = \frac{1}{N} \sum_{i=1}^N \frac{|DSA_i - GSA_i|}{\max(DSA_i, GSA_i)} \quad (4.37)$$

Where  $DSA_i$  represents the “detected spot area” for an  $i^{th}$  spot in the result,  $GSA_i$  represents “ground-truth spot area” for the  $i^{th}$  spot in the ground truth image and  $N$  represents the cardinality of the set  $GT_f \cup R_f$ .  $GT_f$  indicates the set of foreground regions in ground truth image.  $R_f$  shows the set of foreground regions in the obtained segmented result. The operator  $|\cdot|$  represents the absolute value. A zero error will indicate three facts: (1) all spots are segmented (i.e. there is no spot for which the whole spot area in the result is categorized as background), (2) all spots are correctly segmented as depicted in the ground truth image and (3) no background region has been detected as a whole spot. The average of the results of all synthetic images is plotted in Figure 4.19. The proposed method surpasses the other methods in terms of  $Err$  (%). The SCIMO method results in the highest error since it fails to mark many foreground pixels as spot regions and thus these spot regions are part of the background in the SCIMO result. ImageMaster 7 detects more background pixels as spot regions and produces almost double the error as compared to the proposed method. The proposed approach is more conservative in the inclusion of background regions and provides more accurate results.

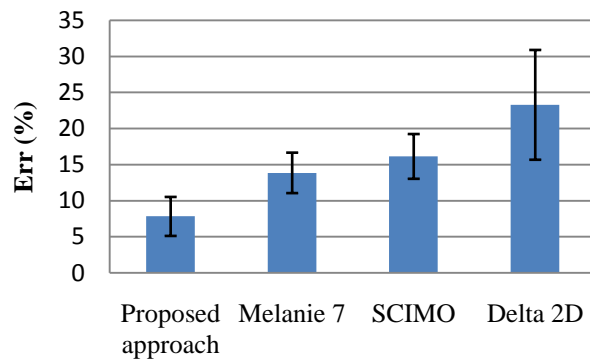


Figure 4.19: Mean error in spot area overlap between the segmentation method and ground truth. The error bar indicates the standard deviation of the corresponding measure (%) across images in the dataset.

The stability of the proposed method under different amounts of noise is also studied in this section. The 2D gel images are produced and acquired using different technological setups or instruments. While acquiring the image using different setups, different amount of noise may get introduced in the images. The Segmentation method should be robust to these little noise variations. Different amount of Gaussian noise (with standard deviations = 1, 2, 3, 4, 5 and 10) have been introduced in the synthetic images which are then segmented using all the different methods (the proposed approach, Delta2D, ImageMaster 7 and SCIMO). The parameters of the proposed approach are kept same throughout the experiment. A change in the parameters of ImageMaster 7 and SCIMO is always required for correct and optimum results. Here, our purpose is to visualize the variability among the outputs of a method at different amounts of noise. Figure 4.20 represents the findings for a synthetic image shown in Figure 4.17 (a). The Delta2D detects more spots with increasing amount of noise. This may be due to lack of smoothing parameter in its spot detection module. The proposed approach and SCIMO seem to

have limited variability while the output of ImageMaster 7 seems to be severely affected by noise.

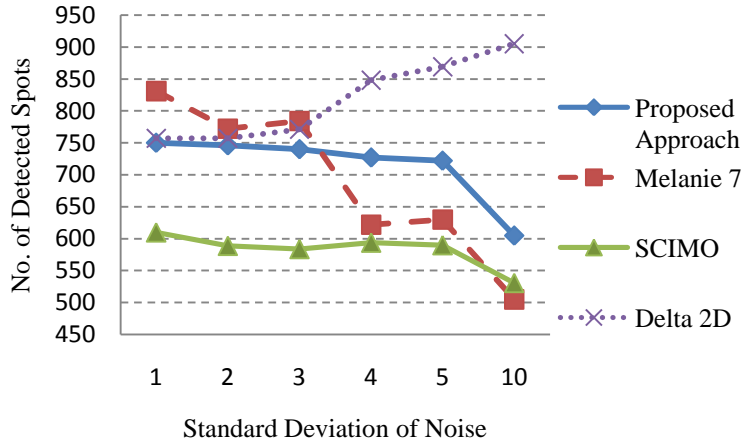


Figure 4.20: Effect of different amounts of Gaussian noise on the segmentation results of the

#### 4.3.10.4 Time Complexity Analysis

The proposed method is based on the undecimated nonseparable wavelet transform. The time complexity of the decomposition of the wavelet transform is  $O(N)$ , where  $N$  is the number of pixels in the image. For an Intel ~2 GHz quad-core, 2 GB RAM computer with Windows XP, the decomposition of the undecimated quincunx transform up to 5 scales takes around 3.5 seconds for a 512 x 512 image.

The maximum size of the neighborhood in equation (4.30) was found to be equal to or less than 9 x 9 for all gel images during the experiments. Thus, the execution of equation (4.30) takes less time than the time taken in a convolution operation using a 9 x 9 filter (i.e. less than one second). The overall execution time of the proposed approach is averaged out to be 12 seconds which is more than the average time taken by ImageMaster 7 (1 second) and SCIMO (8 seconds). Taking a little more time than the commercial software does not matter to the

biologists since they are more interested in the overall accuracy of the result which saves them a significant amount of time which goes into the manual editing of the results. It should also be noted that manual parameter tuning is required in both ImageMaster 7 and SCIMO for producing optimum results from these methods. The time for tuning the parameters may be a few minutes to several minutes, while the proposed method either does not require the parameter tuning at all or requires only a few iterations for selection of the most optimum value of  $ITP_{MIN}$ . Therefore, in the proposed method, only one parameter (or no parameter at all) requires to be tuned which is easier than tuning three or more parameters (as in the case of ImageMaster 7 and SCIMO).

## **Chapter 5 Segmentation of High-resolution 2DGE Images**

### **5.1 Introduction**

Segmentation methods discussed in chapter 4, work well for low-resolution images, but fail to give a satisfactory performance for high-resolution images. High-resolution images require decomposing the image into a large number of scales using these methods, which increases computational complexities. Thus, second segmentation method needs to be modified, so that decomposition into a large number of scales can be avoided for high-resolution image. Based upon the observations of the second segmentation method and the spots' singularities in the wavelet domain, it is found out that the sign of wavelet coefficient can play an important role when the used wavelet is the second derivative of a smoothing function. To cope with the irrelevant singularities, we proposed the use of kernel density estimator (KDE) at each scale of the wavelet transform. The advantage of the proposed method is that the number of scales does not anymore depend upon the resolution or the spot size of the image. The segmentation method evolved so far still outperforms the other methods and gives satisfactory results.

### **5.2 Method using Wavelet and Kernel Density Estimation (KDE)**

In this work, a novel scheme based on the nonseparable quincunx wavelet transform [69] [70] is devised to extract all blob regions from the noisy uneven background. A quincunx wavelet that is the second derivative of a smoothing function provides a multiscale decomposition of an image, where the sign of the wavelet coefficients are used in a novel fashion using kernel density estimation technique to categorize the image pixels into darker and brighter regions. Such formulation brings forward several interesting features which make it distinguishable from other available methods used for blob segmentation. It can be described as

the simplest non-iterative, non-parametric approach which segments out the connected set of pixels belonging to darker or brighter regions, without relying on any specific initialization method such as placement of seed points, initial contours and cluster centers. This multiscale formulation uses a fixed set of scales irrespective of the size and the shape of the blobs. It also does not depend on the intensity of the blob and can extract even low contrast regions. However, it is not so effective in the presence of low-contrast noise. In this work, a global threshold is employed to neglect the low contrast regions. A refinement method consisting of k-means clustering and region merging is developed to improve the segmentation accuracy of the blob regions. The performance of the proposed approach is evaluated on synthetic and real images. The synthetic as well as real 2D gel images are used to demonstrate a possible application of the proposed segmentation approach in the scientific field. The 2D gel images may contain overlapping spots and therefore, a method for separation of the overlapping spots is also devised in this thesis. Experimental results prove that the proposed method is effective for segmenting the images containing objects of various intensities and shapes.

### 5.2.1 Foundation

In this section, an image is assumed to consist of blob objects of various sizes, shapes and intensities in a noisy background (as shown in Figure 5.1). The image segmentation problem is formulated as the detection and extraction of blob regions from the image.

Let  $I_\sigma$  represent the image  $I : \mathbb{R}^2 \rightarrow \mathbb{R}$  at scale  $\sigma$ . In scale-space representation,  $I_\sigma$  is obtained through the convolution of image  $I$  with a Gaussian kernel  $G_\sigma$ .

$$G_\sigma(x, y) = \frac{1}{\sqrt{2\pi}\sigma} \exp\left(-\frac{x^2 + y^2}{2\sigma^2}\right) \quad (5.1)$$

$$I_\sigma(x, y) = G_\sigma(x, y) * I(x, y), \quad (x, y) \in \mathbb{R}^2 \quad (5.2)$$

The symbol ‘\*’ denotes convolution.

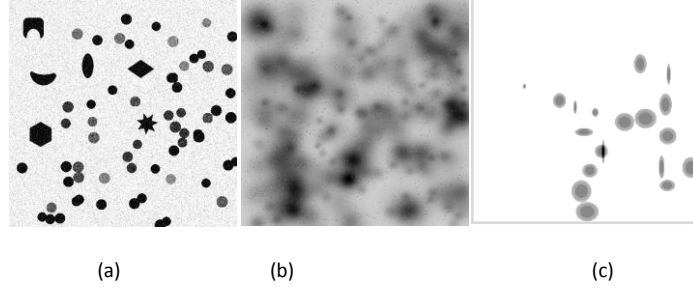


Figure 5.1: (a) A synthetic image of flat objects. (b) A synthetic 2D Gaussian blob image. (c) A noise free synthetic dark flat top Gaussian blob image.

When a second derivative operator such as Laplacian is applied on an image  $I_\sigma$ , it produces zero crossing edges. The darker and brighter sides can be differentiated through different signs of the coefficients of the response.

$$\nabla^2 I_\sigma(x, y) = L(x, y) * G_\sigma(x, y) * I(x, y) \quad (5.3)$$

where L is a Laplacian operator (e.g.  $\begin{bmatrix} 0 & 1 & 0 \\ 1 & -4 & 1 \\ 0 & 1 & 0 \end{bmatrix}$ ) and the right-hand side of the equation

represents the second derivative of the image I at scale  $\sigma$ . Although, the detection of zero-crossing edges is a good method to extract the blob regions, the sensitivity of the operator to noise worsens the situation by producing several false edges and breaking true edges. Practitioners generally use a threshold to discard noisy edges; however, they find it difficult to specify a fixed criterion for choosing the threshold in a given set of images. It is a well known fact that the darker and brighter sides can be differentiated through different signs of the coefficients of the response of a second derivative operator. Figure 5.2 depicts the positive signed response of Laplacian operator, which usually occurs on the darker side of the zero-crossings. For the noisy image, there are several false regions which are detected as darker

regions. Careful investigation reveals that the density of pixels is more in true blob regions adjacent to zero-crossings, and this can be used to distinguish true regions from the rest. This observation is clearly visible at coarser scales (see Figure 5.2).

In another technique usually known as blob detection, the Laplacian of Gaussian (LoG) operator is applied on the image for a predefined scale range and its response is measured across the scales. By analyzing maximum response behavior across scale space, blob centre and corresponding scales are determined [72].

The Hessian matrix for image  $I$  is defined as

$$H(x, y; \sigma) = \begin{bmatrix} \frac{\partial^2 I_\sigma(x, y)}{\partial x^2} & \frac{\partial^2 I_\sigma(x, y)}{\partial x \partial y} \\ \frac{\partial^2 I_\sigma(x, y)}{\partial x \partial y} & \frac{\partial^2 I_\sigma(x, y)}{\partial y^2} \end{bmatrix} \quad (5.4)$$

The determinant of the Hessian matrix,  $\det(H)$  and the trace of the Hessian matrix,  $\text{trace}(H)$  have been useful to determine the image feature.

$$\text{trace}(H(x, y; \sigma)) = \frac{\partial^2 I_\sigma(x, y)}{\partial x^2} + \frac{\partial^2 I_\sigma(x, y)}{\partial y^2} \quad (5.5)$$

$$= \nabla^2 I_\sigma(x, y) \quad (5.6)$$

Thus, the trace is simply the response of the second derivative operator on the image.

The darker and brighter blobs usually result in minima and maxima regions respectively in the gray value image. The minima and maxima of any function can be calculated using Hessian analysis. If  $\det(H(x, y; \sigma)) > 0$  and  $\text{trace}(H(x, y; \sigma)) > 0$  then  $(x, y)$  is a local minimum of image at scale  $\sigma$ . If  $\det(H(x, y; \sigma)) > 0$  and  $\text{trace}(H(x, y; \sigma)) < 0$ , then  $(x, y)$  is a local maximum of image at

scale  $\sigma$ . If  $\det(H(x,y; \sigma)) < 0$ , then  $(x,y)$  are saddle points are represented. If  $\det(H(x,y; \sigma)) = 0$ , any conclusion cannot be drawn with regard to  $(x,y)$  being a stationary point. Figure 5.2 represents the minima in Hessian analysis for a darker blob image. When the scale matches the size of the blob, the region of the blob can be estimated by checking the determinant and trace of the Hessian matrix. Although, using this technique some false regions are obtained and all the obtained regions are not exact. Therefore, the obtained regions need to be refined further for extraction of accurate information (see Figure 5.3). By studying only the trace of the Hessian or response of the second derivative operator, regions fulfilling the condition of positive trace (i.e.  $\text{trace}(H(x,y; \sigma)) > 0$ ) are extracted and depicted in Figure 5.2. These regions include minimum points as well as saddle points. These regions contain more connected pixels than the regions obtained using the condition ' $\det(H(x,y; \sigma)) > 0$  and  $\text{trace}(H(x,y; \sigma)) > 0$ '. The extraneous pixels in these regions can be removed in post-processing based on neighborhood region based operations (similar to the one presented in this chapter). The advantage of this approach is that not all scales are to be searched and studied for the segmentation of the image containing blobs of various sizes. Also, it does not require Hessian analysis for blobs at their corresponding scales. The second derivative operator is applied to the image at some predetermined scale and its response is studied. ' $\text{trace}(H(x,y; \sigma)) > 0$ ' represents the positive coefficients of the response of the second derivative operator at the scale  $\sigma$ . After this, the region is obtained by filtering the positive coefficients which needs to be post-processed to refine the segmentation.

Since the second derivative operator is sensitive to noise, a region obtained using Hessian analysis is severely affected by the noises (see Figure 5.2 and Figure 5.3). A close observation reveals that the density of pixels in the obtained Hessian minima regions is more for true blob

regions in comparison with a noisy background. This finding shows that a density based analysis may improve the obtained result.

Motivated by these observations, in this study, we use a multiscale approach where kernel density estimation (KDE) [73] technique is applied on each scale to obtain information about blob regions. Since a wavelet transform is a nonparametric multiscale tool, we use the quincunx wavelet transform up to a predetermined scale (6 is used in our all experiments). The quincunx wavelet decomposes the image by a scale of  $\sqrt{2}$ . Therefore, a fixed number of decomposition of images is used to analyze all the images in our experiment. The images contain small as well as large sized blobs. Figure 5.3 shows the obtained blob regions from a noisy image using the proposed method.

### **5.2.2 Wavelet and Blob Regions**

When a wavelet is the second derivative of a smoothing function, the zero crossings of the wavelet transform indicate the points of sharper variation at each scale [74]. The completeness and stability of different wavelet zero crossing representations have been studied extensively in [74]-[75]. Zero-crossings in 2D image define a number of connected regions of coefficients sharing the same sign in the neighborhood. Cvetkovic and Vetterli [75] utilized this information to build a 2D wavelet zero-crossing representation which was used to reconstruct the image. Supported by the Hessian analysis in section 5.2.1, the aim of this section is to provide a blob segmentation method based on the information of the connected regions of coefficients sharing the same sign.

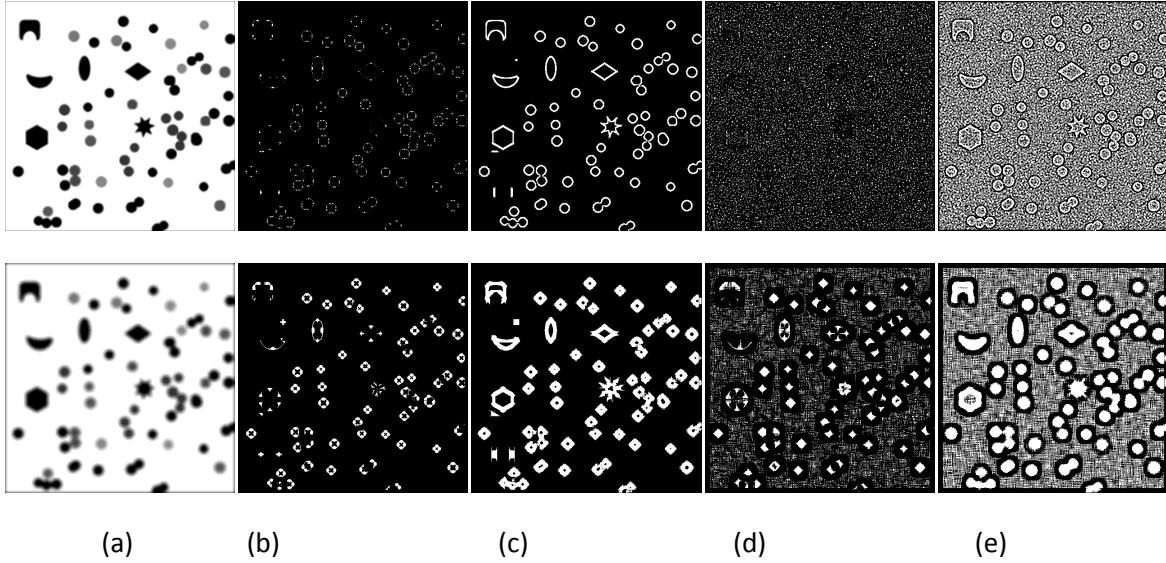


Figure 5.2: Hessian Analysis of a noise free and noisy synthetic image at different scales:  $\sigma=2$  (first row) and  $\sigma = 6$  (second row). (a) Noise free image at specified resolution (b) Hessian minima (regions satisfying condition:  $\det(H(x,y; \sigma)) > 0$  and  $\text{trace}(H(x,y; \sigma)) > 0$ ) for noise-free image (c) positive Hessian trace (regions satisfying condition:  $\text{trace}(H(x,y; \sigma)) > 0$ ) for noise-free image (d) Hessian minima for noisy image (e) positive Hessian trace for noisy image.

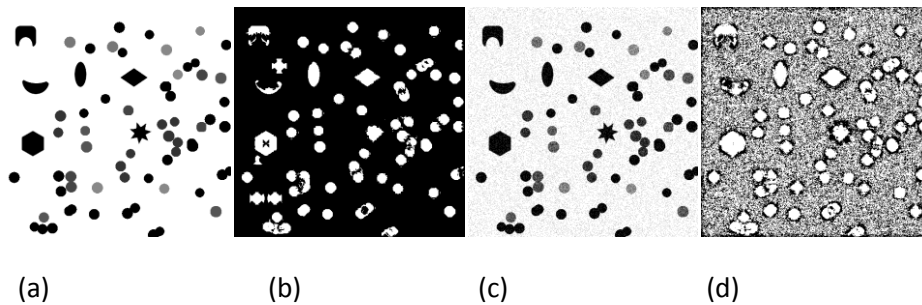


Figure 5.3: Blob regions obtained using Hessian Analysis at different scales for the noise free and noisy synthetic image. The region of each blob is obtained at its corresponding scale by searching in the scale range of  $\sigma = 2$  to  $\sigma = 16$  in step of 0.5. (a) Original noise-free synthetic image and (b) blob regions obtained for noise-free image (c) noisy synthetic image and (d) blob regions obtained for the noisy image.

The zero-crossings of the discrete wavelet transform can result from the singularities of either the original signal or the wavelet itself. A regular wavelet will suppress many zero-crossings while an irregular wavelet will produce many false zero-crossings due to the wavelet itself. False zero-crossings can be discarded by either neglecting the edges in a low variance area or using a region based refinement approach similar to the one employed in this section. Cvetkovic and Vetterli [75] have used a tensor product of one-dimensional regular biorthogonal wavelet, which favors singularity detection in limited directions (horizontal, vertical and diagonal). A 2D nonseparable wavelet functions better as a multi-dimensional tool as it captures the singularities in all directions [34] [35]. The quincunx decomposition being the simplest 2D nonseparable wavelet is implemented using a lifting scheme [70] for this work. The quincunx transform has another advantage over separable wavelets in that it provides finer decompositions of the image by a scale of  $\sqrt{2}$  instead of 2. The undecimated version of quincunx transform is used to provide the details of the same size as of the image which is required in our analysis.

The lifting framework for undecimated quincunx wavelet is depicted in Figure 5.4. In the undecimated version of the lifting scheme, instead of subsampling, the predict (P) and update (U) filters are up-sampled by a dilation matrix  $D = \begin{bmatrix} 1 & 1 \\ 1 & -1 \end{bmatrix}$  in each stage. The scheme with second order filters has two primal and two dual vanishing moments [70]. The detail part at a lower branch of the lifting scheme is obtained by subtracting the predicted value from the original sample (see Figure 5.4). This operation is slightly different from the traditional second derivative operator (as used in section 5.2.1), where the original sample (centre value) is subtracted from the predicted value (i.e. weighted sum of neighborhood values). This leads to a sign change. This also leads to a change in the Hessian condition used to find out region of blobs. Now,  $trace(H(x,y; \sigma)) < 0$  indicates the minimum (or saddle point) at point  $(x,y)$  when the second

derivative operator is quincunx wavelet. Thus, regions of darker blobs along with some saddle points can be obtained using the negative signed response of the quincunx wavelet scheme.

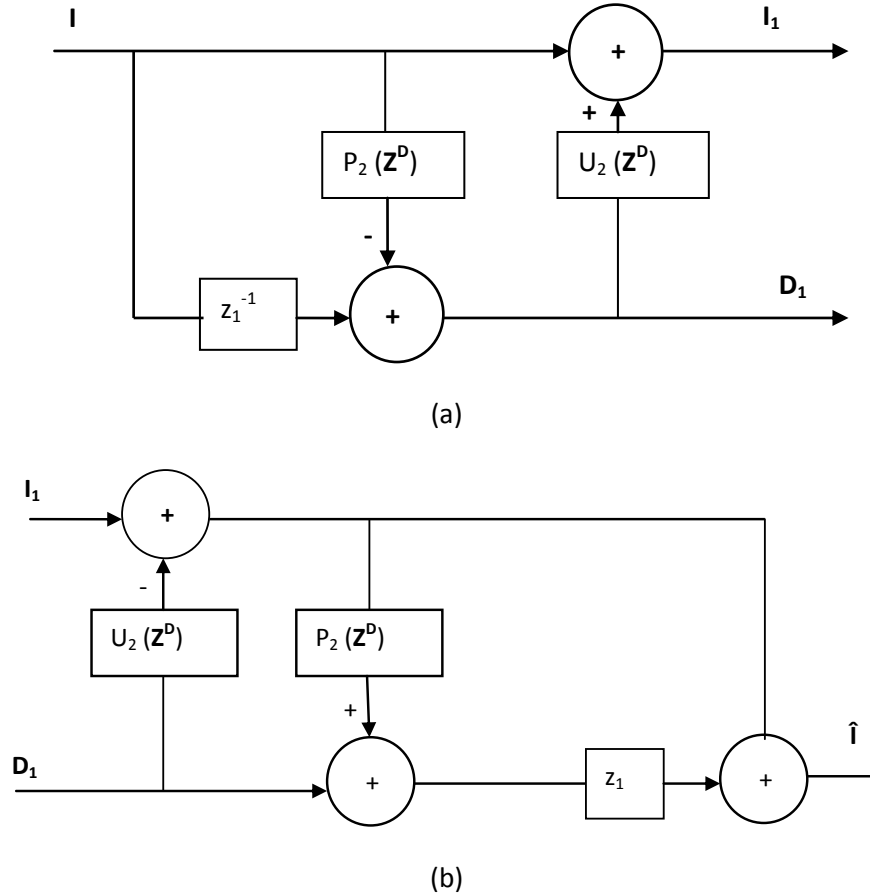


Figure 5.4: Lifting scheme for undecimated quincunx wavelet: (a) analysis and (b) synthesis. Predict (P) and update (U) filters are upsampled by dilation matrix  $\mathbf{D}$ .  $\mathbf{I}_1$  and  $\mathbf{D}_1$  represent the approximation and detail part of the next scale and  $\hat{\mathbf{I}}$  represents the reconstructed image.  $P_2$  and  $U_2$  denote the second order filters that are used [70].

### 5.2.3 Proposed Method

The image is decomposed using the undecimated quincunx wavelet transform up to a predetermined scale  $J$ . In the presence of noise, there will be several zero crossings, several

negative and positive wavelet coefficients at each scale. Consequently, detection of the true zero-crossing edges will be a difficult task. In this case, one solution is to utilize the underlying distribution of positive and negative coefficients in the neighborhood of each pixel. We assume that if the density of negative (positive) signed coefficients is high at a location  $(x,y)$ , then it is more probable that the noise-free wavelet coefficient is negative (positive) at this location. Assuming sign of a wavelet coefficient to be an independent and identical distributed random variable, the underlying density of negative coefficients at a location  $(x,y)$  and scale  $j$  can be given by using the KDE technique [73] as follows:

$$p_j^-(x, y) = \frac{1}{N} \sum_{i=1}^N K_h(x - x_i, y - y_i) \text{sign}^-(wt_j^{(x_i, y_i)}) \quad (5.7)$$

Where

$$K_h(x', y') = \frac{1}{h^d} K(x'/h, y'/h) \quad (5.8)$$

$$\text{sign}^-(wt_{j,(x_i, y_i)}) = \begin{cases} 1 & \text{if } wt_j^{(x_i, y_i)} < 0 \\ 0 & \text{otherwise} \end{cases} \quad (5.9)$$

The symbol  $(x_i, y_i)$  denotes the location of the  $i^{\text{th}}$  neighbor of the wavelet coefficient  $wt_j^{(x_i, y_i)}$  at scale  $j$ . The symbol  $N$  denotes total number of pixels in the image. The  $\text{sign}^-$  function ensures that only negative coefficients are weighted according to their spatial distance in the density estimation. The kernel function  $K(\cdot)$  is defined in two-dimensional subspace (i.e.,  $d = 2$ ) and the scalar  $h$  is the kernel bandwidth. The most popular choice is the Gaussian kernel due to its well known properties of approximations, differentiability, continuity and locality [73]. The two-dimensional Gaussian kernel with predefined support is written as in equation (5.10).

$$K(x, y) = \begin{cases} 0 & \text{if } \sqrt{x^2 + y^2} > h \\ (2\pi)^{-d/2} \exp\left(-\frac{1}{2}(x^2 + y^2)\right) & \text{otherwise} \end{cases} \quad (5.10)$$

As assumed, the  $p_j^-(x, y)$  will represent the probability that the location  $(x, y)$  belongs to the spot region. There are two main properties of the wavelet transform: decorrelation of noise across scales and persistence of significant singularities [28] [31]. The noise has a tendency to decorrelate itself across scales, while significant singularities have the tendency to propagate through scales in the wavelet domain. The edges of the spots will produce significant singularities which may be captured by low wavelet coefficients. For a darker region, high density of negative wavelet coefficients should be present at all scales near the edges of the spots, while noise is not supposed to exhibit such type of consistent behavior. Taking the product of densities across scales will emphasize the consistent behavior across scales and diminish the effect of noise. Therefore, a multiscale density of the sign of wavelet coefficients at a location  $(x, y)$  can be constructed from the product of scale-wise densities as given in equation (5.11).

$$p^-(x, y) = \prod_{j=1}^J p_j^-(x, y) \quad (5.11)$$

Similarly, the multiscale density of positive sign of the wavelet coefficients at location  $(x, y)$  can be calculated using the same kernel as follows

$$p^+(x, y) = \prod_{j=1}^J p_j^+(x, y) \quad (5.12)$$

Where

$$p_j^+(x, y) = \frac{1}{N} \sum_{i=1}^N K_h(x - x_i, y - y_i) \text{sign}^+(wt_{j,(x_i,y_i)}) \quad (5.13)$$

And

$$\text{sign}^+(wt_{j,(x_i,y_i)}) = \begin{cases} 1 & \text{if } wt_{j,(x_i,y_i)} > 0 \\ 0 & \text{otherwise} \end{cases} \quad (5.14)$$

Clearly, a pixel at location  $(x, y)$  has a higher probability to be darker if  $p^-(x, y) > p^+(x, y)$  or has a greater chance to be lighter if  $p^+(x, y) > p^-(x, y)$ . The plateau region in the image will have  $p^-(x, y) = p^+(x, y) = 0$ . Such plateau regions may be merged into the regions just enclosing them. This way the image can be classified into two distinct groups: lighter and darker. Suppose the objects are darker than the background then a foreground binary image ( $B$ ) is formed as

$$B(x, y) = \begin{cases} 1 & \text{if } p^-(x, y) > p^+(x, y) \\ 0 & \text{otherwise} \end{cases} \quad (5.15)$$

Based on prior knowledge,  $B$  can be modified further. In the case of 2D gel images, the image  $B$  is further modified by removing small noisy regions using a morphological opening operation. A disk shaped structuring element ( $SE_{R_{small}}$ ) of radius ( $R_{small}$ ) equivalent to the radius of the smallest spot to be detected is used for this purpose. Figure 5.5 shows the corresponding binary image of a noisy synthetic image.

#### 5.2.4 Region Refinement

The foreground binary image  $B$  is the resulting segmented image containing just the protein spots. The contents of  $B$  depend on the kernel bandwidth  $h$  that determines the number of details to be smoothed out. A low value of  $h$  will preserve frequent sign changes caused by noise while a large value of  $h$  may overlook the desired details (see Figure 5.5). The value of  $h$  is

experimentally determined in the experimental section of this thesis. To reduce the chances of inclusion of extraneous pixels or exclusion of any relevant object pixel in segmentation, the image  $B$  is further refined using a region merging and splitting strategy. The pseudo code of our algorithm has been given in Figure 5.6.

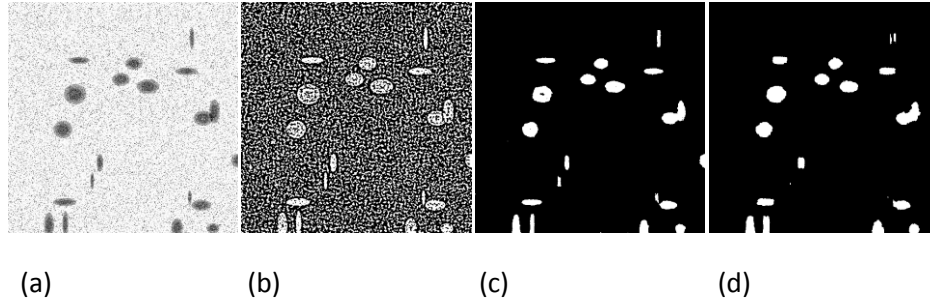


Figure 5.5: Effect of selection of kernel bandwidth on the obtained binary region. (a) Original synthetic images and obtained binary regions using proposed method at following kernel bandwidths: (b)  $h = 1$  (c)  $h = 6$  and (d)  $h = 10$ .

For each connected region in  $B$ , its neighborhood up to a distance ( $R_n$ ) is merged to make an extended region. This extended region now includes both lighter and darker pixels. To separate them out, each extended region is divided into two parts using k-means clustering. We employ k-means for region splitting because it is a simple, unsupervised and fast technique. If mean gray values of these two parts are separated by a threshold  $Th$ , then only the part having low mean gray value (in the case of the darker object) is included in final segmented binary image  $B_f$ . This step will exclude any extraneous pixels, if present. The threshold  $Th$  is required because all detected regions may not be of interest and thus, regions showing significant contrast from the background need to be selected. The pixels that are not included in  $B_f$  form the background region  $B_g$ . The connected regions in  $B_g$  are found out and added to any adjacent object region of  $B_f$  if the difference between the mean gray value of the adjacent object region in  $B_f$  and the mean

gray value of the region in  $B_g$  is less than  $Th$ . This way, any excluded object region will be added back into the final segmented binary image  $B_f$ .

The k-means method is simple and does not incorporate any spatial information with image intensities. In the presence of noise, it may result in segmentation with scattered pixels. A morphological opening operation (erosion followed by dilation) is required to overcome this drawback up to some extent. For the morphological opening, a disk-shaped structuring element ( $SE_1$ ) of radius 1 is used. In Figure 5.6, the symbol ' $\ominus$ ' denotes erosion and the symbol ' $\oplus$ ' denotes dilation.

#### 5.2.4.1 Separation of Overlapped Spots in 2D Gel Images

The final binary image  $B_f$  obtained from above method contains only the foreground pixels. Some blobs in the image may be overlapped and may be detected as single blob region. These overlapped blobs may be separated depending upon their structures or features [11] [61] [66]. In this thesis, we concentrate on the separation of blobs in case of 2D gel images. Several strategies such as Euclidian distance, regional minima in large neighborhoods and spot modeling have been employed by researchers. The modeling of spots is a time consuming task due to the presence of several spots in 2D gel images. The Euclidian distance based method results in over-segmentation of irregularly shaped spots, while the method depending upon regional minima results in over-segmentation of noisy spots due to the presence of several false regional minima. To improve the situation, both Euclidian distance and regional minima are utilized together to split the overlapped spots. The pseudo code of the algorithm has been depicted in Figure 5.7. The spot centers are estimated by finding the local maxima of the Euclidian distance transform (EDT) applied on the binary image  $B_f$ . The false adjacent local maxima are merged into one large region

using the morphological dilation operator. The dilation operator is applied using the disk-based structuring element ( $SE_{R_{small}}$ ) of radius  $R_{small}$ . The spot centers are also estimated by finding the regional minima in median filtered gray value image. The disk-shaped neighborhood of radius  $R_{small}$  is used to find out the regional minima. To reduce the false regional minima due to noise, the median filtered image is used. To remove the false minima that may occur near spot edges, the binary image  $B_f$  is eroded using the disk-shaped structure  $SE_{R_{small}}$ . The regional minima that fall in the foreground region of the eroded binary image are kept as estimated spot centers. The adjacent false regional minima are merged together into one large region by applying the morphological dilation operator using the disk-shaped structuring element  $SE_{R_{small}}$ . If a dilated region of a regional minimum of median filtered gray value image overlaps with dilated local maxima of Euclidian transform, the dilated region of the regional minimum is considered as a valid spot center (step 6 in Figure 5.7). Such spot centers are imposed as minima markers in the gradient of the binary image  $B_f$  and the watershed transform is applied to find out the common boundary between the overlapped spots. Figure 5.8 depicts the separation of overlapped spots. The proposed approach results in better separation of spots and is more robust to multiple regional minima and irregular shape of spots.

---

1. *for each connected region  $C_i$  in  $B$*
2.      $C_{i-extended} = C_i \cup Neighbors_{upto\_distance\_R_N}$
3.      $[darker_{mean}, darker_{region}, brighter_{mean}] = split_{kmeans}(C_{i-extended})$
4.     *if  $(brighter_{mean} - darker_{mean}) > Th$  then*
5.          $B_f = B_f \cup darker_{region}$
6.     *end if*
- 7.*end for*
8.  $B_g = B - B_f$
- 9.*for each connected region  $D_i$  in  $B_g$*
10.    *find all foreground regions  $F_i \in B_f$ , that are adjacent to  $D_i$*
11.    *for each  $F_i$  adjacent to  $D_i$*
12.        *if  $|meangrayvalue(F_i) - meangrayvalue(D_i)| < Th$  then*
13.             $F_i = F_i \cup D_i$
14.        *end if*
15.    *end for*
16.    *update  $B_f$  with modified  $F_i$*
17. *end for*
18.  $B_f = (B_f \ominus SE_1) \oplus SE_1$

---

Figure 5.6: Pseudo code of the Region Refinement method.

---

//Estimating the spot center using Euclidian distance

1.  $E_1 = localmaxima ( EDT(B_f) )$

2.  $E_1^D = E_1 \oplus SE_{R_{small}}$

//Estimating the spot centers using regional minima of gray value image

3.  $E_2 = regionalminima_{R_{small}} ( median ( I ) )$

4.  $E_2' = E_2 \cap ( B_f \ominus SE_{R_{small}} )$

5.  $E_2^D = E_2' \oplus SE_{R_{small}}$

6.  $valid\ spot\ centers = \{ p \in E_2^D \mid q \in (E_2^D \cap E_1^D) \text{ and } q \subseteq p \}$

7.  $G = gradient(B_f)$

// Mark valid spot centers as minima marker by assigning them minimum value

8.  $G(valid\ spot\ centers) = -Infinity$

9.  $L = watershed(G)$

//L is the final segmented image.

---

Figure 5.7 Pseudo code for separation of overlapped spots in 2D gel image.

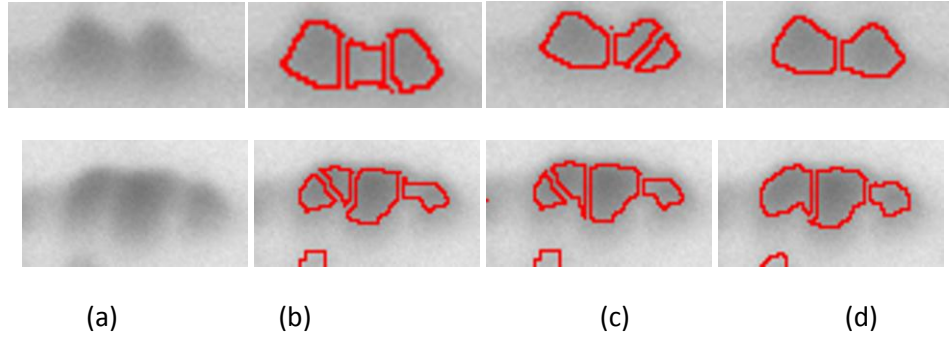


Figure 5.8: (a) Protein spots from real image and separation of overlapped spots after segmentation, using (b) Euclidian distance, (c) regional minima and (d) proposed approach.

### 5.2.5 Experimental Results and Discussion

The performance of the proposed method is demonstrated using the following different types of images: (1) synthetic images containing flat objects of different shapes and sizes, (2) synthetic images containing 2D Gaussian blobs, (3) real 2D gel images and (4) other biological images. Only synthetic images are used to measure the performance quantitatively. An example of them is shown in Figure 5.1. To measure the accuracy of segmentation of synthetic images, Jaccard Distance (JD) error metric is used and defined as  $JD(S, G) = (1 - |S \cap G| / |S \cup G|)$ , where  $S$  is the segmented result and  $G$  is ground truth reference. The operator  $|\cdot|$  denotes the number of elements (pixels) in the set. To find the percentage of correctly classified pixels in the image, a metric called ‘segmentation accuracy index’ is also defined as  $(S, G) = (|S \cap G| + |S^B \cap G^B|) / (image\ size)$ . The symbols  $S^B$  and  $G^B$  denote the set of background pixels in the segmented result and ground truth reference respectively. Both JD and SA vary between 0 and 1. For correct segmentation, JD should be low and SA should be high. For the real 2D gel images, the ground truth is generally difficult to find out and can be estimated using the consensus of expert biologists. Still, the variability in different manual segmentations for the same image cannot be ignored [76]. The relative comparisons between the obtained segmentation results

using different methods for the 2D gel images is qualitatively studied using close observations done by human experts.

### **Parameter Determination**

The parameters used in the proposed methods are number of scales  $J$ , kernel bandwidth,  $h$ , neighborhood distance,  $R_N$  and threshold,  $Th$ . The number of scales  $J = 6$  is found to be sufficient to capture the entire information in an image. In quincunx domain, a scale  $J = 6$  corresponds to scale 3 of the separable wavelet, since quincunx wavelet decomposes the image by a scale factor of  $\sqrt{2}$  instead of 2. The neighborhood distance,  $R_N$ , defines the locality of the blob region. A high value of  $R_N$  indicates that the nature of segmentation is more global while a low value of  $R_N$  indicates that the nature of segmentation is more local. Based on the study of synthetic and real images (see Figure 5.9),  $R_N = 2$  stands for the most obvious choice.

The threshold  $Th$  defines the contrast of the blob object to be detected. For the images containing low contrast blob objects, this value should be small. For the images containing only high contrast blob objects, this value should be large. Our synthetic and gel images contain blob objects of various intensities in a noisy or inhomogeneous background. We choose  $Th = 6$  for these types of images. For other types of biological images, the set of suitable parameters is obtained by experimenting on a few images. After that, the parameters remain fixed for that set of images.

The kernel bandwidth  $h$  depends upon the details to be extracted out and thus, depends on the size of blobs and amount of noise. For the images containing very low amount of noise, this value can be as low as  $h = 1$ . For images containing high amount of noise or inhomogeneous background, this value should be sufficient to cope with the noise or inhomogeneity. Although,

when blob size is small, a large value of  $h$  may smooth out small blobs and may fail to detect them (see Figure 5.4). For our set of synthetic images, we plot the segmentation accuracy index SA for each choice of the value of  $h$  (see Figure 5.10). It is clearly visible that  $h = 6$  is a good choice for these types of images. Since spots in the real gel images are usually modeled using 2D Gaussian or flat 2D Gaussian, the real gel images may be assumed to be similar to our synthetic images of Gaussian blobs. Therefore, the value of  $h$  is chosen as 6 real images too. The real 2D gel images available on public databases (e.g. [77]) are of low-resolution and contain several blobs of small sizes. A high value of kernel bandwidth  $h = 6$  may overlook many small sized spots. Therefore, for such images, a low value of  $h$  ( $h = 1$ ) is used to detect blobs. The images in the last set are noise-free, therefore, a low value of  $h$  ( $h = 1$ ) is preferred.

### **Quantitative and Qualitative Analysis**

The proposed method is applied on the synthetic image shown in Figure 5.1(a) and a set of other biological images (see Figure 5.11). The fluorescence microscopic cell image (shown in Figure 5.11(b)) contains several blobs of the same size [79]. The LoG method [72] is generally used to find the centers of the blobs. The region of blobs can be segmented using the proposed approach. For the red blood cell images infected with malaria parasites, the detection and segmentation of the dark structures [78] is important. With a low value of threshold  $Th$ , the proposed approach can detect all cells along with dark cells. To detect only dark cells, the threshold  $Th$  is increased from 6 to 45. Figure 5.11(c) depicts the segmentation results obtained using proposed approach.

Due to the presence of an uneven background, the general purpose methods are not sufficient to segment the synthetic images consisting of 2D Gaussian blobs and real 2D gel images (see

Figure 5.9 (f)). Therefore, application specific methods available in the literature, as described in section 5.1, need to be compared with our methods. The methods based on watershed [12] and Otsu's threshold [13] has been used to compare our results. The proposed method is also compared with two commercial software packages (Delta2D and ImageMaster 7) for 2D gel image analysis. The parameters of the watershed method [12] have been adjusted for each image. The parameters of Otsu's threshold method [13] have been selected as mentioned in the paper [13]. The parameters of the commercial software have been adjusted for each image. The parameters of the proposed method for 2D gel images are selected as described in section 5.2 and are kept constant throughout the experiment.

All synthetic Gaussian blob images have been subjected to a small amount of Gaussian (with a standard deviation between 1 and 5) and salt and pepper (1%-3%) noise to simulate the noise in original gel images. The segmentation results of a synthetic Gaussian blob image are shown in Figure 5.12. Watershed method [12] does not cope well enough with salt and pepper noise; therefore the image is filtered using a 3 x 3 median filter before applying this method. Delta2D has a manual preprocessing operation for removing white and black speckles which has been utilized for obtaining a better result. By observing Figure 5.12, it can easily be concluded that the boundary produced by our method is more compact and contains only a few background pixels. The ground truth image has been formed by assuming the spot boundaries at a distance of two standard deviations from the spot's center and is depicted in Figure 5.13. This assumption is normal in our case since most of the methods developed for 2D gel images produce large spot regions in the segmentation for the most of the spots (see Figure 5.12 and Figure 5.15). A total of 90 true spots are present in this image (see Figure 5.12(a) and Figure 5.13).

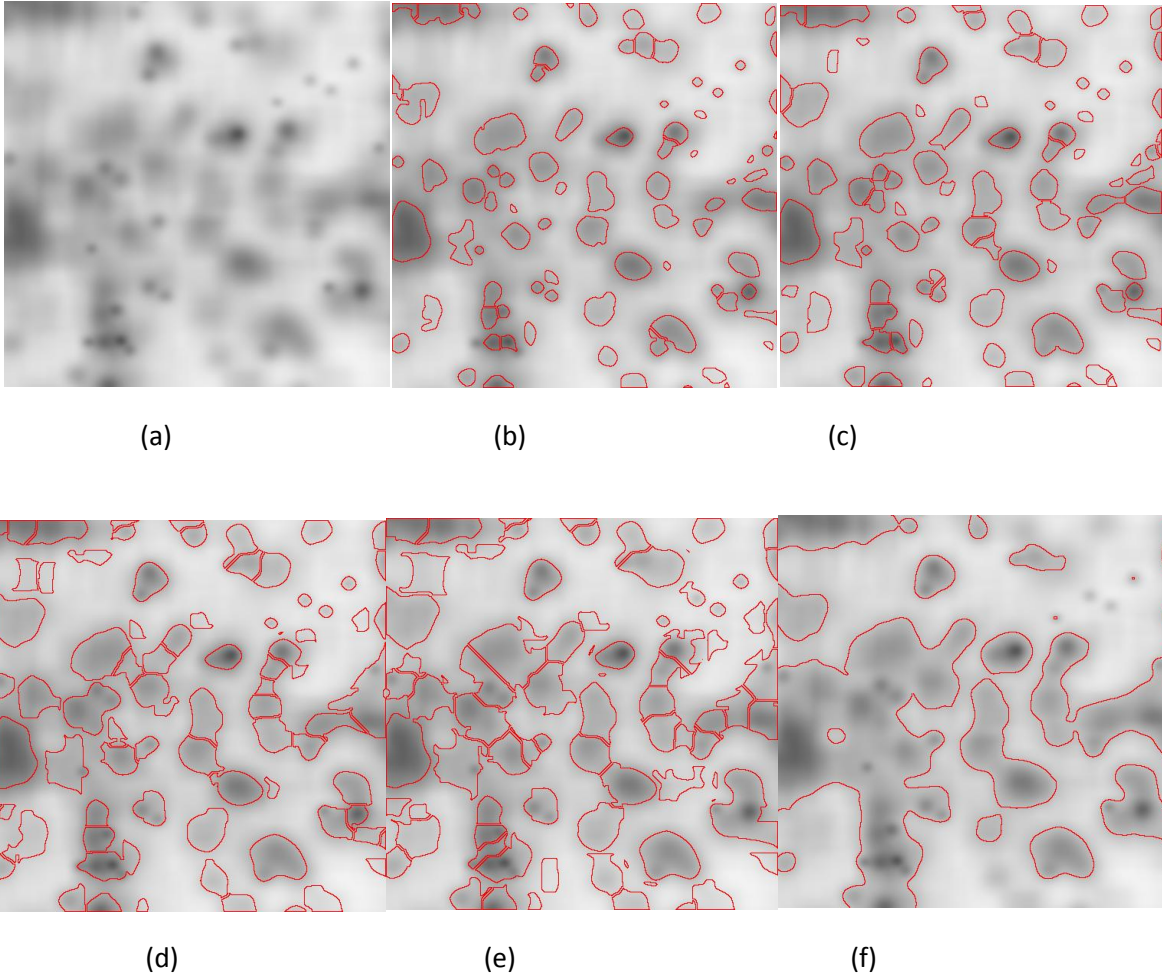


Figure 5.9: Effect of the parameter  $R_N$  on the final segmentation. (a) A 2D gel image and (b)-(e) segmented results using our method when  $R_N$  was set to 2, 5, 10 and 15 respectively. As value of  $R_N$  increases, region of blobs spreads out and may merge nearby blobs. It leads to more global segmentation. (f) Segmentation by a global method – active contour [7].

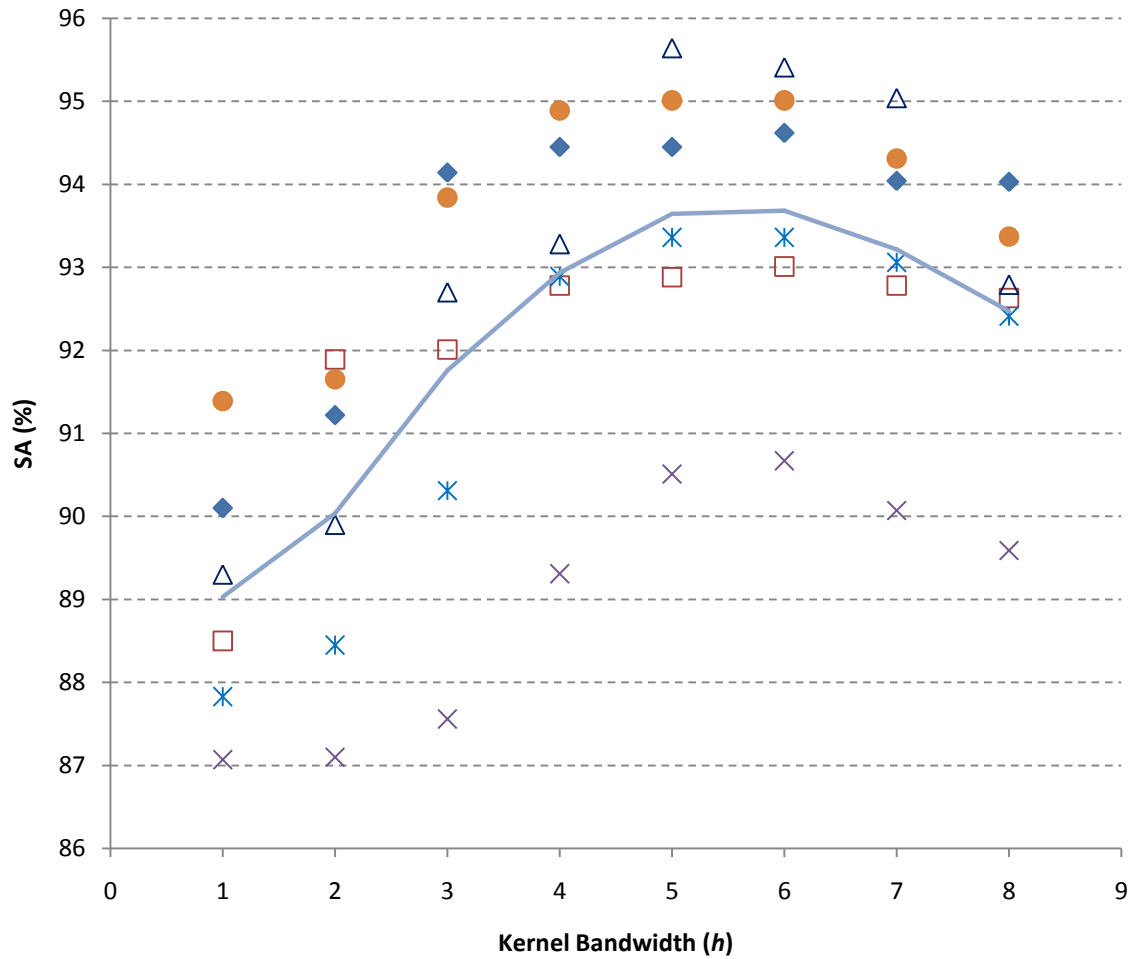


Figure 5.10: Plot of kernel bandwidth ( $h$ ) vs. average segmentation accuracy SA (%) for six synthetic images. Images are corrupted with Gaussian noise (with a standard deviation between 1 and 5) and salt and pepper (1%-3%). Example of synthetic images containing 2D Gaussian blobs is shown in

Figure 5.21(b). Solid line represents average SA for all images.

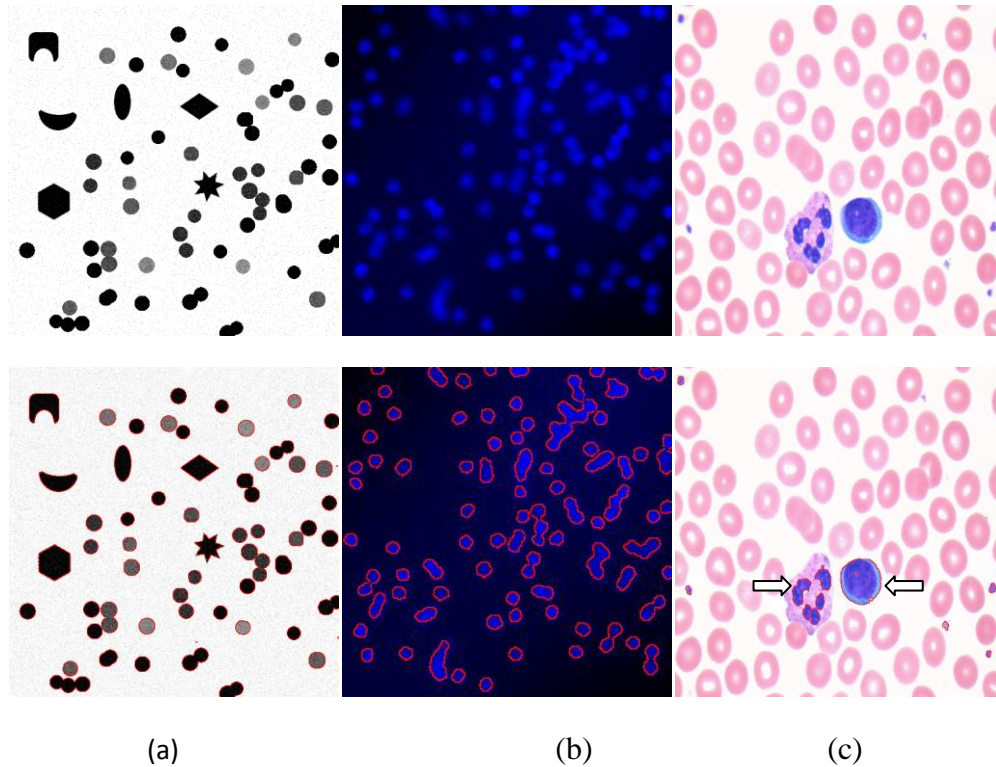


Figure 5.11: Original synthetic/ real images (first row) and segmentation results obtained using proposed approach ( second row).

To provide an in-depth analysis, the total number of detected spots along with the number of artifacts and the number of missed spots is also considered for result comparison. The proposed method detects total 93 spots along with 4 artifacts (background region detected as a spot). It also fails to detect one true spot. The watershed method [12] and Otsu's threshold method [13] miss more spot regions (15 and 10 spot regions respectively) and detect more number of artifacts too (11 and 12 false spot regions respectively). Total 86 spots are detected by the watershed method [12]. Otsu's threshold method [13] detects total 89 spots with 2 overlapped and 4 over-segmented spot regions. Many regions are over-segmented by Delta2D due to the presence of noise. It also fails to detect 3 true spots. Image Master 7 detects total 88 spots with 4 artifacts and 5 overlapped spot regions. One spot is over-segmented too. Both, the proposed approach and

ImageMaster 7 detect less number of artifacts and miss less number of spots in comparison with the others. The boundaries produced by ImageMaster 7 are much further away from the actual spot boundaries. Overall, the proposed method produces the least segmentation error and detects the most number of true spots for the synthetic Gaussian blob images (see Figure 5.14).). The terms ‘JD (%) – Worst’ and ‘SA (%) – Worst’ used in Figure 5.14 (a) denote the metrics JD and SA respectively for the segmentation of such images. Since the segmentation of the synthetic Gaussian blob images presents a challenging situation for the commercial software packages, the segmentation analysis of another type of synthetic images is necessary. The best case may be a noise free image consisting of dark flat top Gaussian blobs with distinct boundaries (see Figure 5.11(c)). The segmentation of such images is easy and can also be easily carried out with any known methods [51] [53] [55]. The segmentation of such images presents an ‘easy case’ or a ‘best case’ scenario for our experiments. All the methods produce accurate segmentations for such images. The terms ‘JD (%) – Best’ and ‘SA (%) – Best’ used in Figure 5.15 (a) denote the metrics JD and SA respectively for the segmentation of such images. Since all the spots are correctly detected in the ‘best case’ scenario, the Figure 5.15 (b) represents only the case of segmentation of synthetic Gaussian blobs (‘worst case’ scenario). The proposed method produces the least difference between best case and worst case segmentation scenarios among all the methods (see Figure 5.14(a)). In terms of number of segmented spots, the performance of the proposed method is comparable with the commercial software packages (see Figure 5.14 (b)). In brief, the proposed method produces the least segmentation error, detects a smaller number of artifacts and misses a smaller number of spots as compared to commercial software.

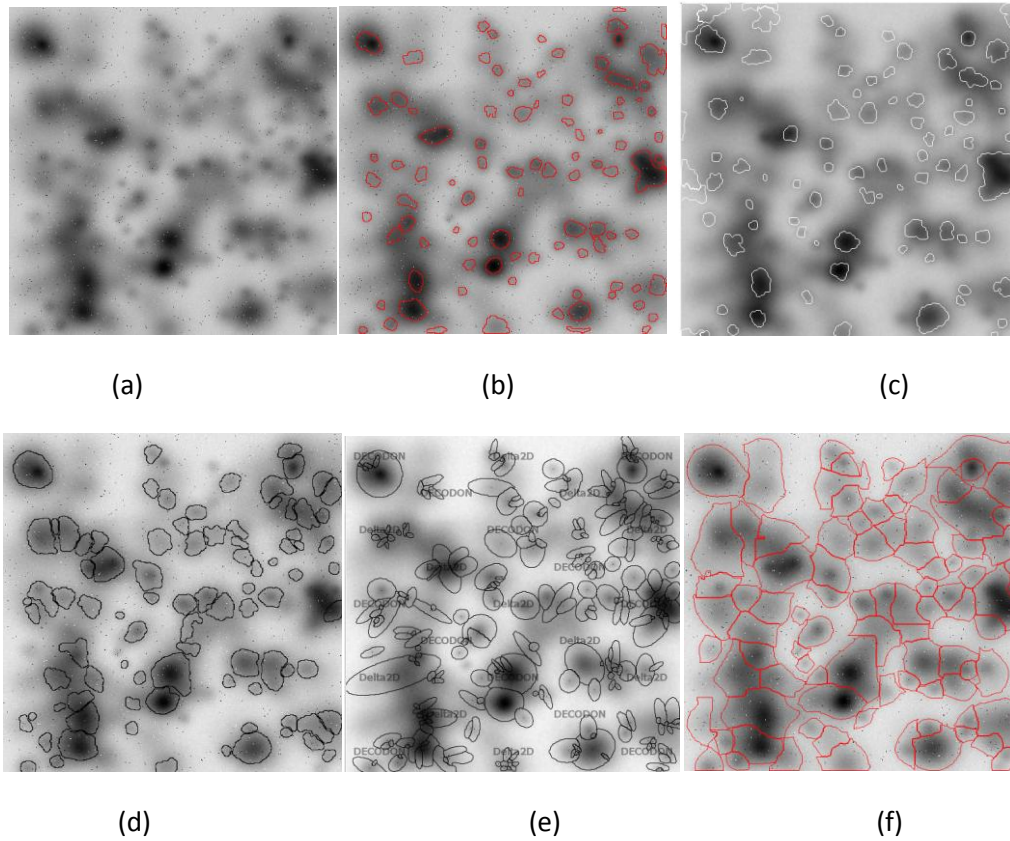


Figure 5.12: (a) A synthetic image consisting 2D Gaussian blobs and its segmentation results using (b) the proposed approach, (c) watershed method, (d) Otsu's threshold, (e) Delta2D and (f) Image

Master 7.

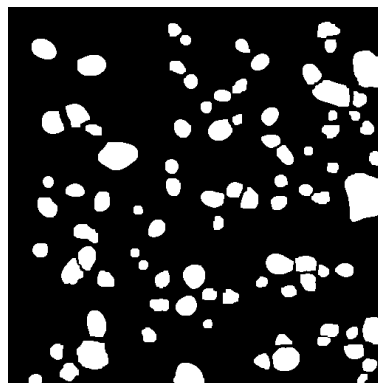
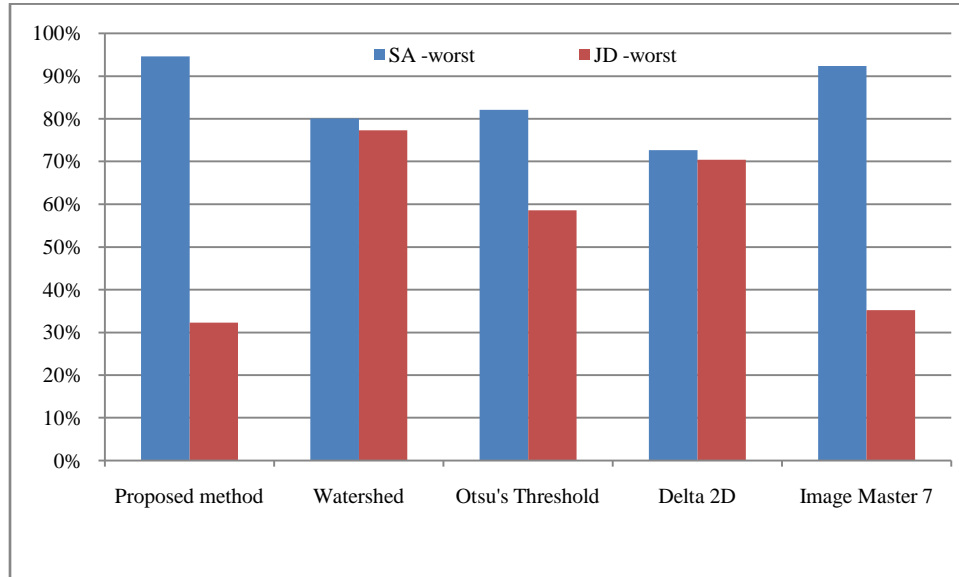


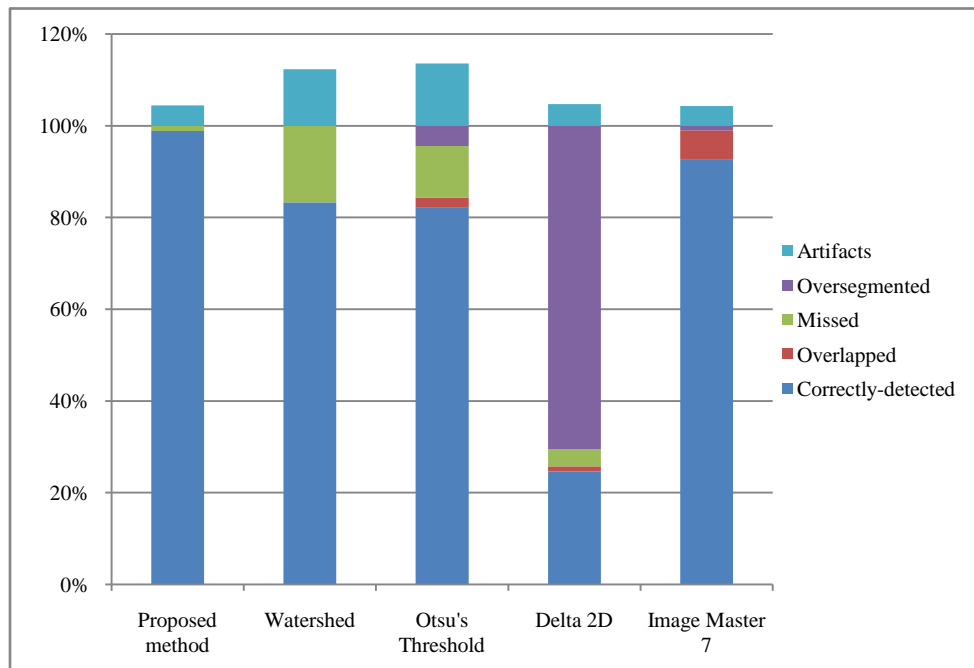
Figure 5.13: Boundaries of the spots are assumed at a distance of two standard deviations from their center.

Figure 5.15 and Figure 5.16 depict the segmentation results of real 2D gel sub-images. The proposed method provides more plausible boundaries of the spots. The proposed method also seems to produce less number of artifacts caused due to streaks and background intensity variations. The Otsu's threshold [13] detects several implausible spots for the sub-image shown in Figure 5.16. Delta2D and ImageMaster 7 seem to detect more number of implausible spots on the streaks than the proposed method for the sub-image shown in Figure 5.16. The boundary produced by ImageMaster 7 is less accurate than the proposed method.

The source code of the proposed method can be downloaded from <http://www.mathworks.com/matlabcentral/fileexchange/48610-wavelet-based-noise-robust-image-segmentation>. The proposed approach is planned to be implemented in the advanced version of our spot picker robot system.

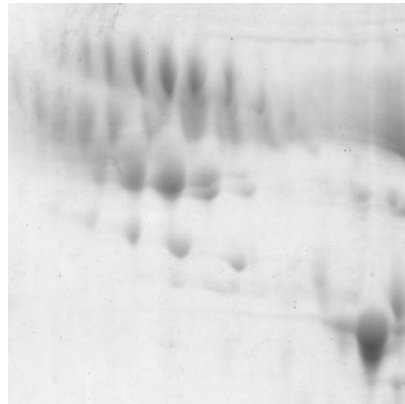


(a)

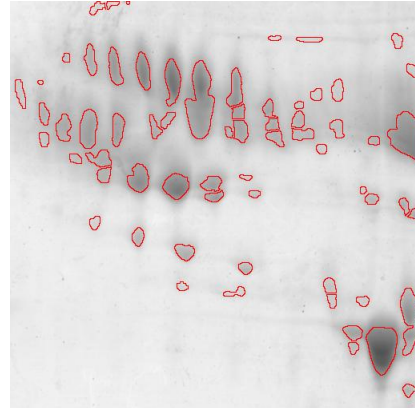


(b)

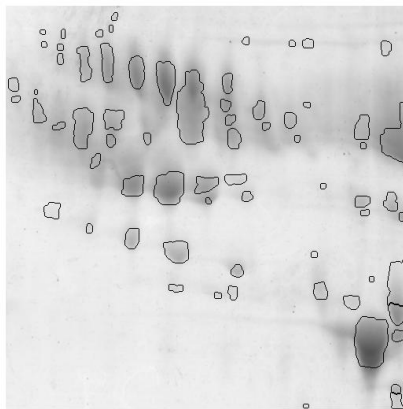
Figure 5.14: Comparison of different segmentation methods for synthetic Gaussian blob images. (a) The segmented spot regions are evaluated using the terms JD and SA. (b) The number of segmented spots is evaluated as a fraction of the total number of true spots in ground truth.



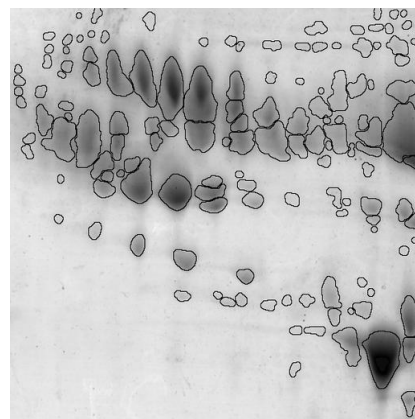
(a)



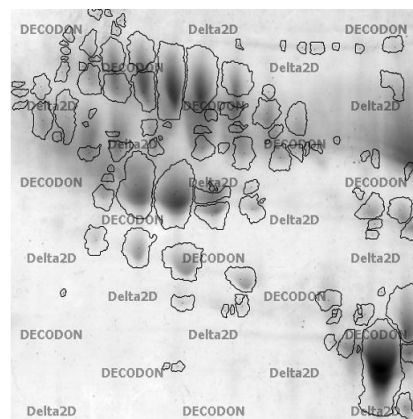
(b)



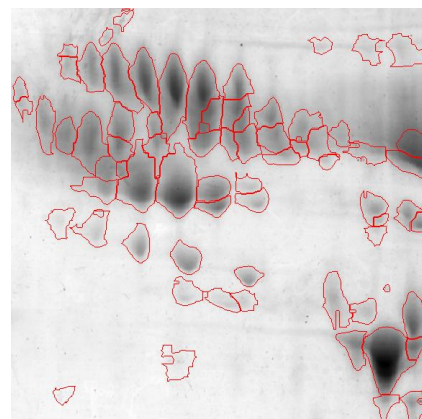
(c)



(d)

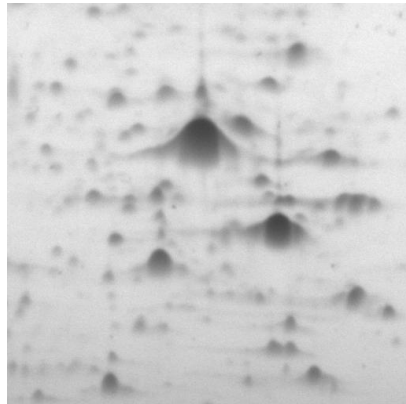


(e)

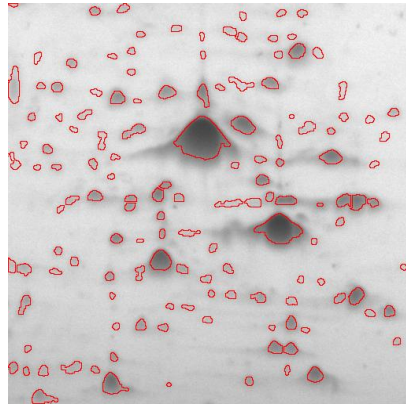


(f)

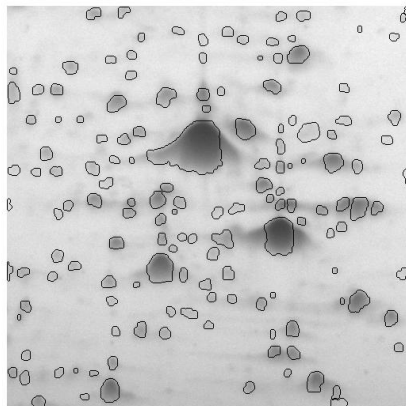
Figure 5.15: (a) Real 2D gel sub-image and segmentation results using (b) proposed approach, (c) watershed, (d) Otsu's threshold, (e) Delta2D and (f) ImageMaster 7.



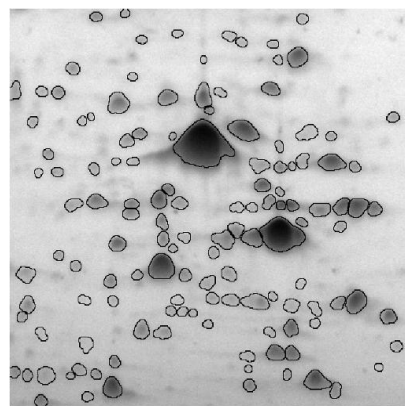
(a)



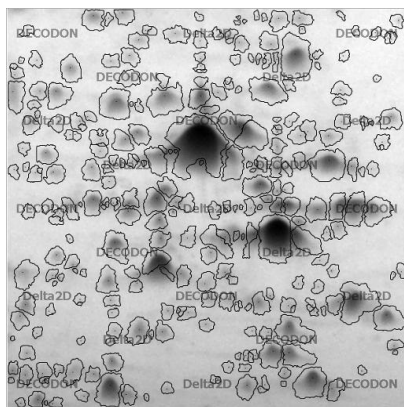
(b)



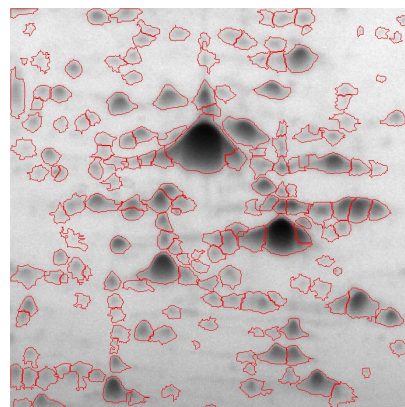
(c)



(d)



(e)



(f)

Figure 5.16: (a) Real 2D gel sub-image and segmentation results using (b) proposed approach, (c) watershed, (d) Otsu's threshold, (e) Delta2D and (f) ImageMaster 7.

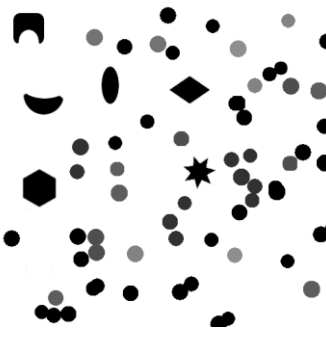
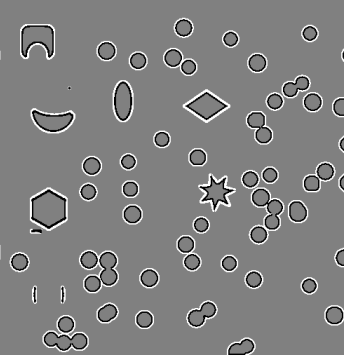
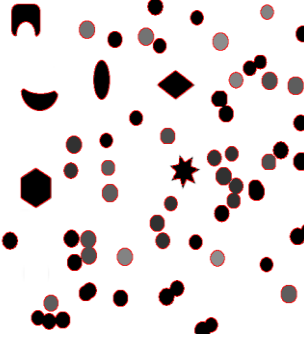
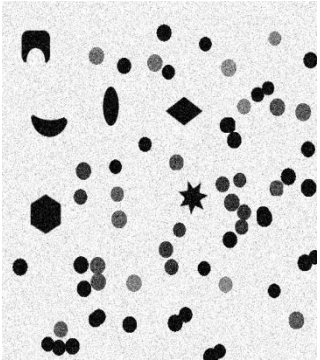
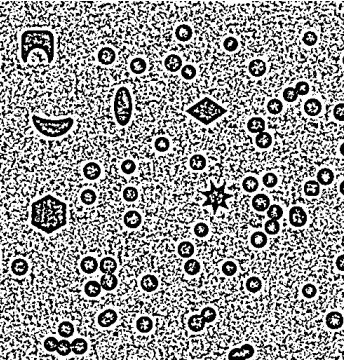
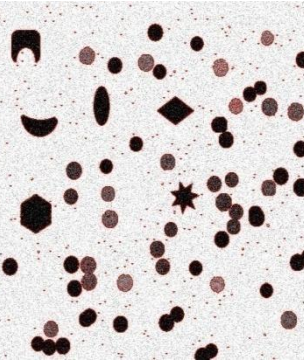
### 5.2.6 Detailed Results on Synthetic Image

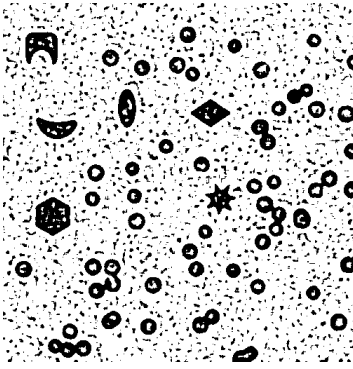
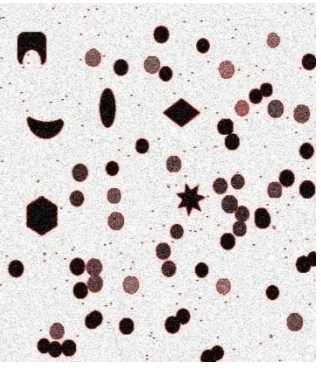
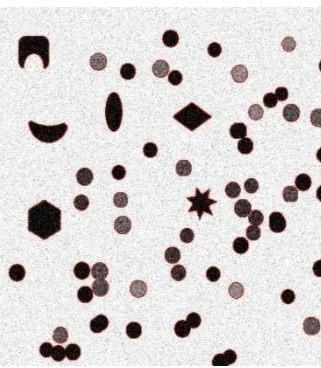
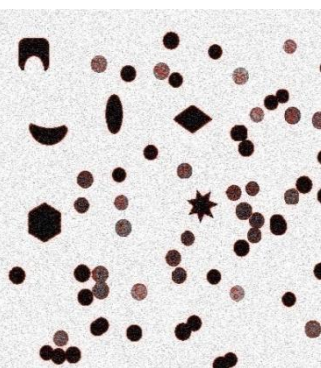
The first set of synthetic images is segmented with the traditional global k-means method as well as with the state-of-the-art region based segmentation methods, namely, Chan-Vese active contour (CV) [55] and Kernel Weighted Fuzzy C-Means incorporating local information (KWFCM) [52]. These methods have been applied to a synthetic image shown in Figure 5.18 and the obtained segmentation errors have been plotted in Figure 5.17. The proposed approach produces, overall, the least segmentation error and thus, outperforms these methods. The synthetic image has various objects of different intensities and shapes. The result shown in Figure 5.17 also reflects that the proposed method is less sensitive to image noise and can provide better segmentation even when low-intensity objects are present. Global methods don't produce accurate segmentation results of 2D gel images shown in Figure 5.19.

Some natural images containing objects which are either darker or lighter as compared to their local background are selected from a public database [77]. Figure 5.20 show that the proposed method provides more desirable segmentation with less number of background pixels.

In this chapter, a novel wavelet based method for accurate and noise robust image segmentation is presented. The method is formulated upon a subjective criterion that blob objects are either darker or lighter than their local background. The darker or brighter regions are extracted by comparing the multiscale density of the signs of wavelet coefficients and are further refined using a region splitting and merging strategy. Experimental results show that proposed approach outperforms the state-of-the-art methods. Its application on 2D gel images demonstrates that this method may prove as a powerful tool for the segmentation of other similar scientific images.

Table 5.1 Detailed result on synthetic image

Original image	Bandwidth (h)	Darker regions, lighter regions and plateau regions indicated by black, white and gray color respectively.	Effect on Final segmentation  Parameters for synthetic image : $R_N=2$ , Th=6
 <p>Noise free synthetic image</p>	1		
	1		

<p>Synthetic image corrupted with an additive Gaussian noise of standard deviation <math>\sigma_n = 40</math>.</p>	<p>3</p>		
	<p>6 (see the corner of the star and smooth background)</p>		
	<p>9</p>		

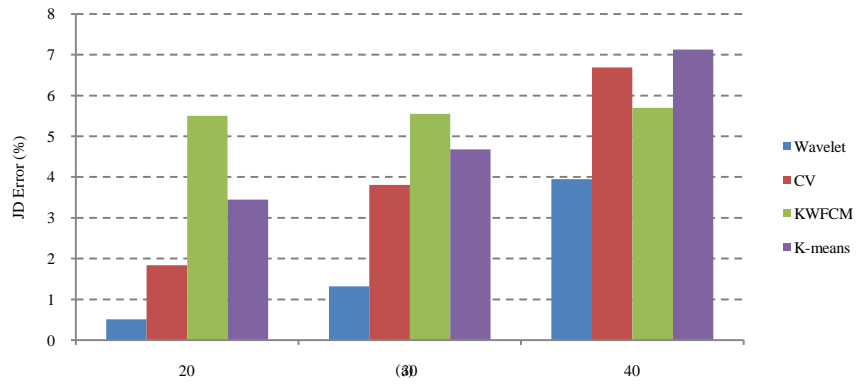
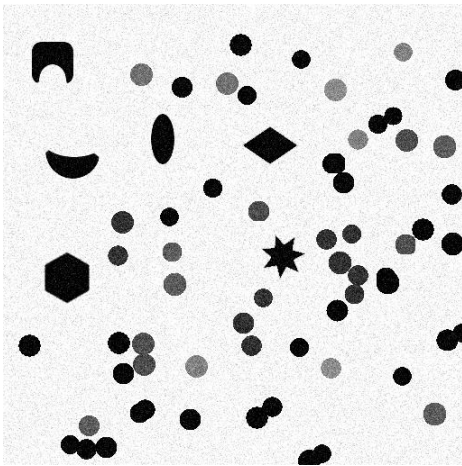
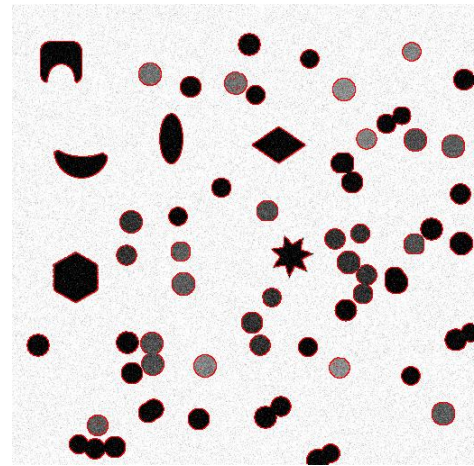


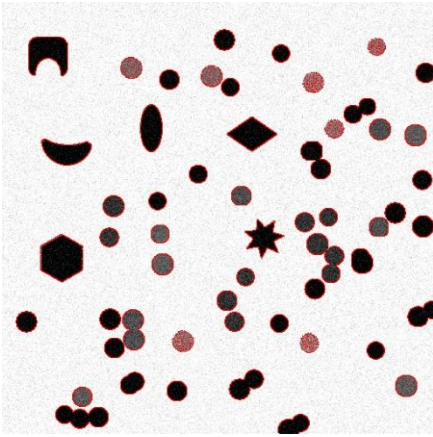
Figure 5.17: Segmentation errors for the image of Fig. 5.21(a) with different methods. The horizontal axis represents the standard deviation of Gaussian noise in the image.



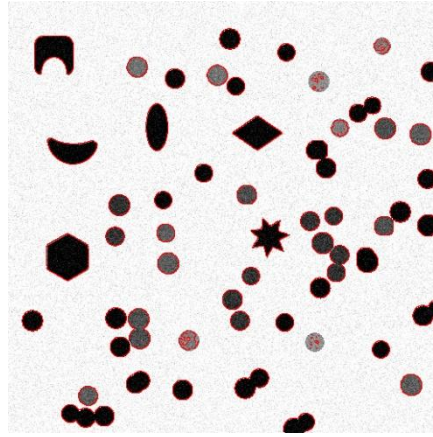
Noisy synthetic image corrupted with the additive Gaussian noise of standard deviation  $\sigma_n = 20$ .



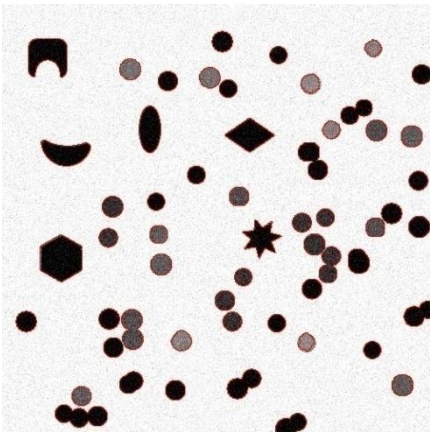
The proposed approach produces the least error among the methods presented here. (JD Error = 0.46%, execution time = 8.5 seconds)



k-means with no. of cluster=2 (low gray value object affected) (JD Error=3.45%, execution time=1.1 seconds)



KWFCM with no. of cluster = 2 (lowest gray value object almost undetected-very small portion detected) (JD Error= 5.5%, execution time=100 seconds)



CV –two phase segmentation with  $\mu = 0.2 \times 255^2$ , initialized with small circles all over the image, max. Iterations =100, time-step=0.5. (lower gray value object affected) (JD Error=1.84%, execution time=60 seconds)

Figure 5.18: Comparison with other state-of-the-art methods

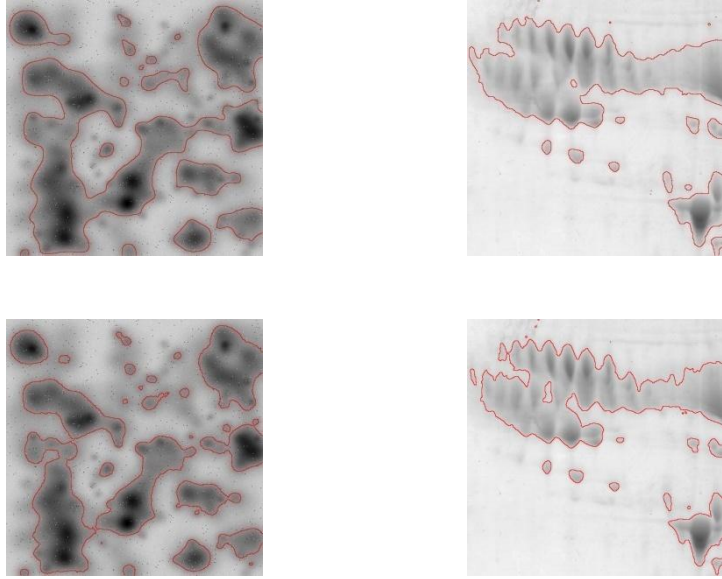


Figure 5.19: First Row: CV method on synthetic and real 2D gel images.

Second Row: KWFCM method on the same synthetic and real 2D gel

images

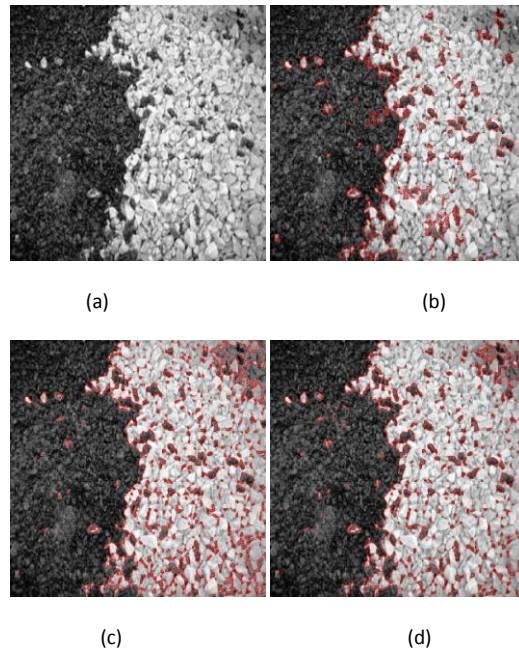


Figure 5.20: (a) An image from the public database and its segmentation using (b) Proposed approach

(c) CV and (d) KWFCM.

## Conclusion

The proposed strategy for 2D gel electrophoresis image analysis from denoising to segmentation of the protein spots has been explained for the extraction of true protein spots. The proposed novel approaches based on nonseparable wavelet decomposition have been implemented for better characterization of the interior regions and the edges of the protein spots and for removal of artifacts and streaks.

In this work, a successful attempt has been made to utilize advantages of various wavelet based methods to move towards a more reliable and accurate technique for denoising of proteomic 2DGE images. Separable wavelets are tensor product of 1D wavelets and can't carry much directional information. Nonseparable wavelets are directional and therefore they capture directional information more efficiently. This property has been utilized for the denoising of 2DGE images in our work. From our experiments, we observed that superb results were obtained on using undecimated quincunx wavelet with Bayes threshold.

In order to provide better segmentation results, the behaviour of spots, background and streaks has been analyzed in nonseparable wavelet domain. Three methods have been systematically developed by addressing problems one by one. Each method provides different insights to the analysis of 2D gel images and nurtures the understanding of the problems to be solved. In the first method, the behaviour of streaks is analyzed in a combined domain of watershed and wavelets that primarily helps in the segmentation of protein spots. The presence of faint spots and artifacts is another big challenge in the segmentation process which demanded a different approach. For this purpose, a novel wavelet inter-scale ratio was derived to characterize the spots interior region in the second method. The method successfully segments

the spots from an inhomogeneous background using a fixed global threshold. Reducing computational complexity and number of artifacts was again a challenge. The multi-scale kernel density estimation of wavelet coefficients across scales was derived for this purpose and was utilized to formulate our third segmentation method which provides the most robust and sophisticated solution for high-resolution images. The experimental results shown in this thesis demonstrate that the efficiency and accuracy of the proposed approaches is better than commercially available software and previously reported works.

Registration is an important part of 2DGE image analysis work flow. Image Registration is a process that involves aligning of two or more images with respect to a reference image using geometric transformations applied on target images. Registration methods usually require feature points which depend upon the accuracy of segmentation. A less accurate segmentation provides erroneous feature points and leads to errors in registration. The proposed segmentation algorithms are also helpful for providing more accurate registration as discussed in Appendix I.

The proposed methods are incorporated in our Spot Picker Robotic System [2] for laboratory demonstration. The Spot Picker Robotic System is a state-of-the-art technology for precise detection, positioning and excision of protein spots from 2D gel images. It can play a pivotal role in the field of proteomics by using powerful imaging algorithms to help discover new drugs and biomarkers for early disease diagnosis.

Differential analysis and selection of significant spots for excision are critically important for comparison between samples from a healthy and a diseased person. Our future work will concentrate on developing advanced methods for the registration and differential analysis of 2DGE images and building a spot classifier for a complete and fast automation of the system.

# Appendix I 2DGE Image Registration

## I.1 Introduction

Image Registration is a process that involves aligning of two or more images with respect to a reference image using geometric transformations applied on target images. Misalignment of images may be due to a variety of reasons like a change in camera perspective, lens distortion etc. Image matching in 2D gel analysis is used for finding out identical proteins in two or more gel images. But due to gel to gel variations and presence of noise, this task becomes complicated. Any protein may not be at the same pixel location in the two images and even size variations may occur. Existing software packages like ImageMaster 7 and Delta2D are semi-automated and require significant human intervention to achieve better results. A gel pair may take 4-6 hours of manual spot matching corrections with current software packages. Hence, manual analysis of these complex gel images is a significant bottleneck in the proteomics research field, which can be alleviated by improved and efficient automatic registration techniques. When several gel images have been matched, a single synthetic gel image can be generated which combines the information from the individual images in an optimal way. This synthetic gel should consist of a representative set of spots generated from several registered gel images. The merging process needs to take the shape information of registered spots into account and can also be used as a reference gel to perform further registration against unknown gel images. After alignment, there may still be differences in regions where proteins appear or disappear, and the shape and/or size of each spot could be different. These regions may form outliers that need to be examined further.

## I.2 Registration Techniques

2DE gel registration can be done either using algorithms driven directly from image metrics or using point set registration techniques. The former technique is known as intensity based while the latter is known as feature based. Both these techniques start with referring one gel image as the reference or fixed image and others gel images are called target gel images.

### I.2.1 Intensity Based

Intensity-based methods compare intensity patterns in images via image metrics. These algorithms share the common framework depicted in Figure I.1. Image registration is the process of finding a coordinate transformation function  $T(\mathbf{x})$ , given by equation (I.1)

$$T(x): \mathcal{R}^2 \rightarrow \mathcal{R}^2 \quad (\text{I.1})$$

which maps the spatial coordinates from one image  $I_1(\mathbf{x})$  onto another image  $I_2(\mathbf{x})$ , so that  $I_2(T(\mathbf{x}))$  is spatially aligned with  $I_1(\mathbf{x})$ . Mathematically, the registration problem is formulated as an optimization problem:

$$\underset{\mathbf{k}}{\operatorname{argmin}}\{ C ( T_{\mathbf{k}}, I_1, I_2 ) \} \quad (\text{I.2})$$

where  $C$  denotes a cost metric and vector  $\mathbf{k}$  contains parameters of the transformation function  $T$ .  $C$  contains two parts, similarity measure and regularization term. We have employed normalized mutual information [84][88] as a similarity measure and the smoothness constraint as regularization term. The transformation function is expressed as a linear combination of B-spline basis functions of order 3, placed on a regular control point grid.

$$T_k(\mathbf{x}) = \sum_{i,j} \begin{pmatrix} c_1(i,j) \\ c_2(i,j) \end{pmatrix} \beta^3 \left( \frac{x}{s_x} - i \right) \beta^3 \left( \frac{y}{s_y} - j \right) \quad (\text{I.3})$$

Cost metric C is minimized using the Broyden-Fletcher-Goldfarb-Shanno (BFGS) iterative optimization method.

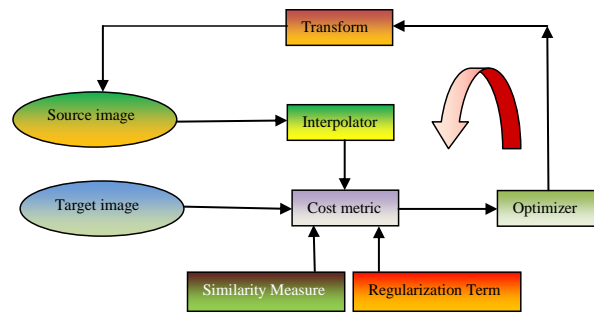


Figure I.1: Registration Framework

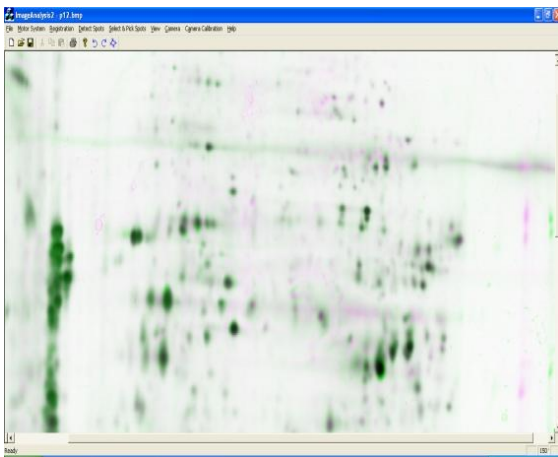


Figure I.2: Image registration result

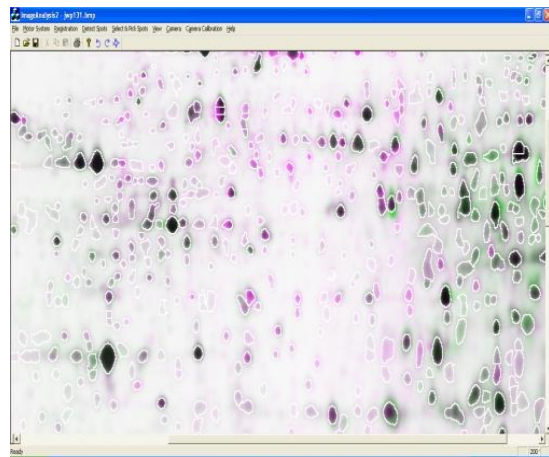


Figure I.3: Segmentation after image registration

The experimental image is displayed with pure green color (figure I.2 and I.3). The reference image is displayed with pure magenta color. The experimental image is overlaid on the reference image. Proteins which are present in both gels are represented using a dark color (dark green to black). The darkness of the colour depends upon the concentration of proteins. Algorithms driven by image metrics like mutual information and sum of squared distances (SSD) generate a

subspace containing many local minima for small spot features and these algorithms are not sufficiently robust against these minima [86].

### I.2.2 Point Set Registration

Point set registration is the process of aligning two point sets. These point sets are comprised of protein spot information, extracted using the segmentation algorithms discussed in chapter 5. Individual spot parameters like centroid, size, area, intensity, coefficient of variation etc. are calculated for each spot. Given two sets of points,  $x = (x_1, x_2, \dots, x_N)^T$  and  $y = (y_1, y_2, \dots, y_M)^T$ , where  $N, M$  is the number of points in  $x$  and  $y$  respectively.  $x_i = (x_{i1}, x_{i2})$  and  $y_i = (y_{i1}, y_{i2})$ , our aim is to find out the correspondence matrix  $m$  of size  $N \times M$  and transformation  $T$  that minimizes equation (I.4) [86]

$$E(m, T) = \sum_{i=1}^N w_i (x_i - T(y'_i))^T S_i^{-1} (x_i - T(y'_i)) + \lambda J_T \quad (\text{I.4})$$

where

$$y'_i = \frac{m_i y}{\sum_j m_{ij}}, w_i = \sqrt{\sum_j m_{ij}^2} \quad (\text{I.5})$$

and

$$S_i = (m_{ij} (S_{i,x} + S_{j,y})) / \sum_j m_{ij} \quad (\text{I.6})$$

$m$  is the correspondence matrix with values in the range  $[0, 1]$ , representing the confidence of each possible correspondence between  $y_i$  and  $x_i$ .  $y'$  and  $w$ , respectively, are the weighted mean location and combined weight for a weighted combination of original points  $y$ . Covariance

matrices  $S_{i,x}$  and  $S_{j,y}$  represent uncertainty on the location of each point. The last term  $J_T$  represents transformation smoothness [86]. Closed form solution of equation (I.4) doesn't exist and parameter  $\lambda$  provides a trade-off between smoothness and accuracy of matching. Iterated closest point (ICP) [87] based algorithm can be used in an iterative fashion to find out the best match. General ICP algorithm is depicted in figure I.4. ICP based algorithm consist of a distance metric, correspondence matrix and transformation function [86]. Distance metrics that can be used are Euclidean distance, shape context [85], mahalanobis distance etc. Shape context (SC) [85] provides a semi-global description of the spatial distribution of neighbouring points by counting the number of points in radial regions, yielding histograms that can be made invariant to affine deformations. Correspondence matrix  $m$  can be calculated from the distance metric using a variety of methods like closest point, kCP, SoftAssign [90] and Bi-partite graph matching [85]. Bi-partite graph matching ensures one to one correspondence. Finally, the transformation matrix is calculated by using initial point and correspondence and the target points are mapped to new points. Techniques exist in literature to find out closed form solutions to calculate transformation parameters like iterative M-estimation using residual distance distribution (M-estimator) [89]. The Shape context (SC) [85] based method with thin plate spline as transformation is applied to two gel images and the results obtained are depicted in figure I.5.

Segmentation method discussed in chapter 5 is deployed to find out the protein spots in two gel images and then SC method is applied on the pair of gel images. Matching results are shown in figure I.5. Match vectors are shown in the target image in green color.

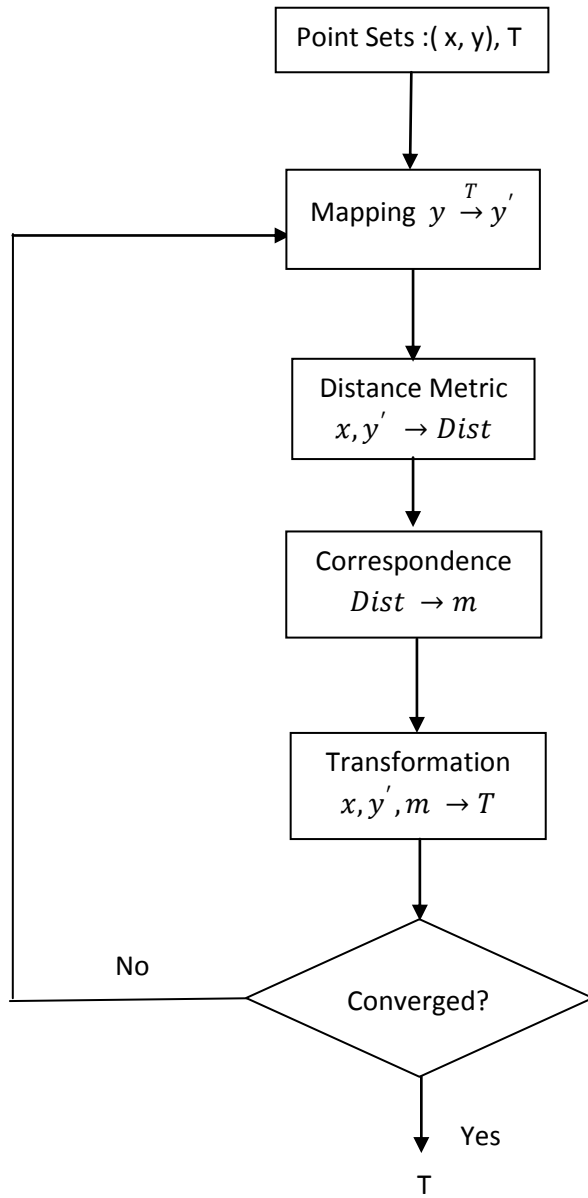


Figure I.4: ICP algorithm

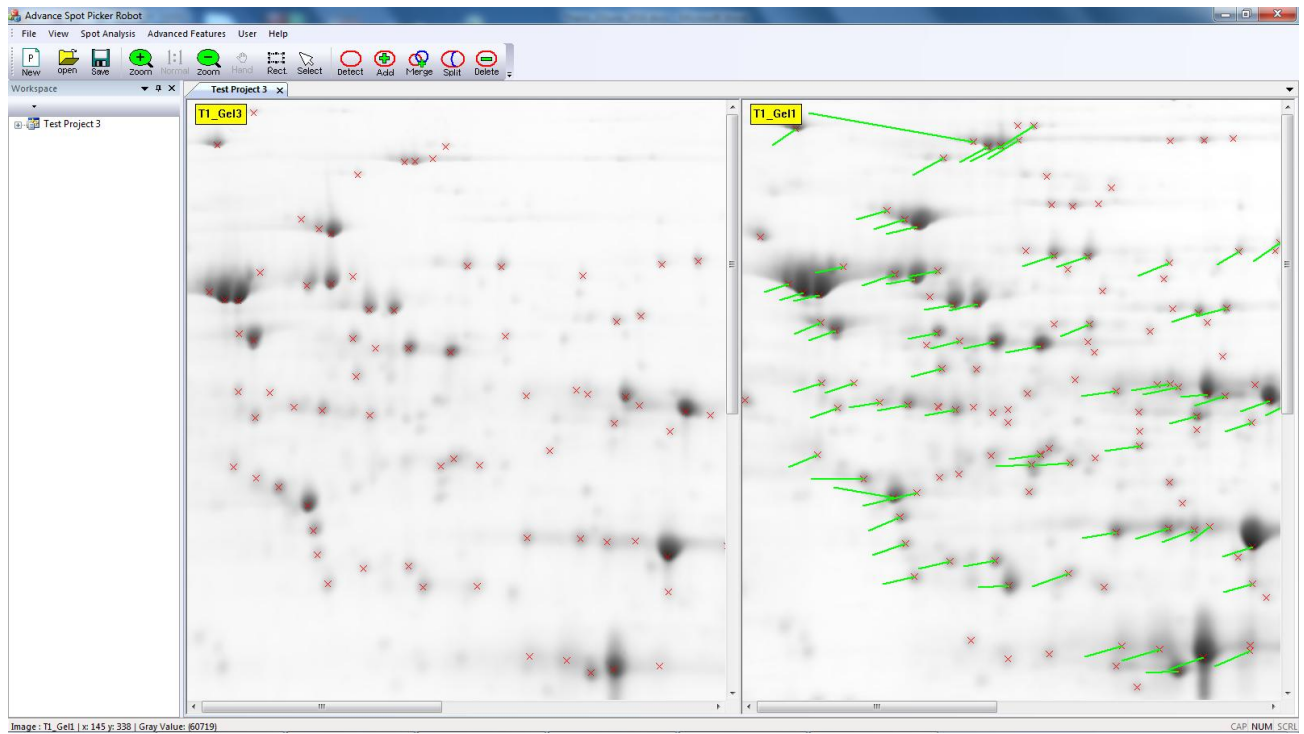


Figure I.5 SC[85] method results. T1\_Gel3 is reference gel image and T1\_Gel1 is target gel image. Match vectors are shown in green color.

## References

- [1] Marc R. Wilkins, Christian Pasquali, Ron D. Appel, KeliOu, Olivier Golaz, et al., "From Proteins to Proteomes: Large Scale Protein Identification by Two-Dimensional Electrophoresis and Amino Acid Analysis," *Nature Biotechnology*, Vol.14, No. 1, pp. 61-65, 1996.
- [2] "Development of Spot Picker Robot for Proteomics Applications", Ratnesh S Sengar, A.K Upadhyay, D.N.Badodkar, R.K.puri, Manjit Singh, MGR Rajan, Vikram M Gadre, *IEEE International Conference on Robotics & Automation (IEEE-ICRA2013) at Karlsruhe, Germany*, DOI: 10.1109/ICRA.2013.6630801, pp 1704-1709., [2013].
- [3] Thierry Rabilloud, Cécile Lelong," Two-dimensional gel electrophoresis in proteomics: A tutorial," *Journal of Proteomics*, vol. 74, no. 10, pp. 1829-1841, Sept. 2011.
- [4] Pierre Marie Nugues, "Two-Dimensional Electrophoresis Image Interpretation," *IEEE Trans. On Biomedical Engineering*, vol.40, no.8, pp.760-770, August 1993.
- [5] P.H. O'Farrell, "High-resolution two-dimensional gel electrophoresis of proteins," *J.Biological Chem.*, vol.250, pp.4007-4021, 1975.
- [6] P. Cutler, G. Heald, I. R. White, and J. Ruan, "A novel approach to spot detection for two-dimensional gel electrophoresis images using pixel value collection," *Proteomics*, vol. 3, pp. 392-401, 2003.
- [7] Yi-Sheng Liu et al, "Spot detection for a 2DE gel image using a slice tree with confidence evaluation," *Mathematical and Computer Modelling*, vol.50, pp.1-14, 2009.
- [8] M. A. Savelonas, E. A. Mylona, Dimitris Maroulis, "Unsupervised 2D gel electrophoresis image segmentation based on active contours," *Pattern Recognition*, vol. 45, no. 2, pp. 720-731, Feb. 2012.
- [9] L. Vincent, P. Soille, "Watersheds in digital spaces: An efficient algorithm based on immersion simulations," *IEEE Trans. Pattern Anal.Mach. Intell.*, vol. 13, no. 6, pp. 583-598, Jun 1991.
- [10] Kim, Y., Kim, J., Won, Y., In, Y., "Segmentation of protein spots in 2D gel electrophoresis images with watersheds using hierarchical threshold," *Lecture Notes in Computer Science*, no. 2869, pp. 389-396, 2003.
- [11] Mylona, E.A., Savelonas, M.A., Maroulis, D., Kossida, S., "A Computer-Based Technique for Automated Spot Detection in Proteomics Images," *Information Technology in Biomedicine, IEEE Transactions on* , vol.15, no.4, pp.661-667, July 2011.
- [12] A. dos Anjos, A. Moller, B. Ersboll, C.Finnie, and H. Shahbazkia, "New Approach for Segmentation and Quantification of Two-Dimensional Gel Electrophoresis Images," *Bioinformatics*, vol. 27,no. 3, pp. 368-375, 2011.
- [13] Kostopoulou, E., Zacharia, E., Maroulis, D., "An Effective Approach for Detection and Segmentation of Protein Spots on 2D-Gel Images," *Biomedical and Health Informatics, IEEE Journal of*, vol.PP, no.99, pp.1,1, 2013.
- [14] A.M. Wheelock, A.R. Buckpitt, "Software-induced Variance in Two-Dimensional Gel Electrophoresis Image Analysis," *Electrophoresis*, vol. 26, pp. 4508-4520, 2005.
- [15] K. Kaczmarek, B. Walczak, S. de Jong, B.G.M. Vandeginste, "Preprocessing of two-dimensional gel electrophoresis images," *Proteomics*, vol.4, pp.2377-2389, 2004.
- [16] Morten Rye, Ellen M. Fargestad, "Preprocessing of electrophoretic images in 2DE analysis," *Chemometrics and Intelligent Laboratory Systems*, vol. 117, pp. 70-79, Aug 2012.

- [17] Sternberg, S.R., "Biomedical Image Processing," *Computer*, vol.16, no.1, pp. 22- 34, Jan 1983.
- [18] Bettens, E., Scheunders, P., Sijbers, J., Van Dyck, D., Moens, L., "Automatic segmentation and modelling of two-dimensional electrophoresis gels," *Image Processing, 1996. Proceedings., International Conference on*, vol.2, no., pp.665-668, 16-19 Sep 1996.
- [19] Massimo Natale, Alfonso Caiazzo, Enrico M. Bucci, Elisa Ficarra," A Novel Gaussian Extrapolation Approach for 2D Gel Electrophoresis Saturated Protein Spots," *Genomics, Proteomics & Bioinformatics*, ISSN 1672-0229, 10.1016/j.gpb.2012.06.005, November 2012.
- [20] M. Rogers, J. Graham, R.P. Tonge, "Statistical models of shape for the analysis of protein spots in two-dimensional electrophoresis gel images," *Proteomics*, vol. 3, pp. 887–896, 2003.
- [21] M.B. Rye, B.K. Alsberg, "A multivariate spot filtering model for two-dimensional gel electrophoresis," *Electrophoresis*, vol. 29, pp. 1369–1381, 2008.
- [22] Appel RD, Vargas JR, Palagi PM, Walther D, Hochstrasser DF, "ImageMaster II--a third-generation software package for analysis of two-dimensional electrophoresis images: II. Algorithms," *Electrophoresis*, vol. 18 (15), pp. 2735-48, Dec. 1997.
- [23] <http://www.decodon.com/delta2d.html>
- [24] Ratnesh Singh Sengar, A. K. Upadhyay, Pushkar G. Patwardhan, Manjit Singh, Vikram M. Gadre, "Approaches based on nonseparable filter banks in 2D Gel electrophoresis image analysis," *Proceedings of Asia Pacific Signal and Information Processing Association (APSIPA) International Conference*, p.p. no. 387-392, December 2010.
- [25] Sengar, R.S., Upadhyay, A.K., Singh, M., Gadre, V.M., "Segmentation of two-dimensional electrophoresis gel image using the wavelet transform and the watershed transform," *The eighteenth annual National Conference on Communications (NCC-2012)*, DOI:10.1109/NCC.2012.6176861, 3-5 Feb. 2012.
- [26] Video lectures: Advanced Digital Signal Processing-Multirate and Wavelets: <http://nptel.iitm.ac.in/courses/117101001/28>.
- [27] Peter R. Massopust, "Fractal Functions, Fractal Surfaces, and Wavelets" Academic Press, 1994.
- [28] Mallat,S. *A Wavelet tour of Signal Processing*. Academic Press, San Diego, CA 1998.
- [29] Wornell G.W. and Oppenheim A. V., "Wavelet based representations for a class of self-similar signals with application to fractal modulation," *IEEE Trans. on Information Theory*, vol. 2, pp. 785-800, 1992.
- [30] Meyer,Y. *Ondelettes et Operateurs*, Hermann, Paris, 1990, vol. I–III.
- [31] Mallat S, Hwang W.L, "Singularity detection and processing with wavelets," *Information Theory, IEEE Transactions on*, vol.38, no.2, pp.617-643, Mar 1992.
- [32] A. Pizurica, W. Philips, I. Lemahier and M. Acheroy, "A versatile wavelet domain noise filtration technique for medical imaging," *IEEE Trans. on Medical Imaging* vol. 22, no. 3, March 2003.
- [33] S.G. Mallat, "A Theory for Multiresolution Signal Decomposition: The Wavelet Representation," *IEEE Transactions on Pattern Analysis and Machine Intelligence*, Vol. 11, No. 7, pp. 674-693, July 1989.

- [34] T. Chen and P. Vaidyanathan, "Considerations in multi-dimensional filter bank design," *IEEE International Symposium on Circuits and Systems*, Vol. 1, pp. 643-646, 1993.
- [35] M. Vetterli, "Multi-dimensional sub-band coding: Some theory and algorithms," *IEEE Transactions Signal Processing*, Vol. 6, No. 2, pp. 97-112, Feb. 1984.
- [36] Minh N.Do and Martin Vetterli, "The Contourlet Transform: An Efficient Directional Multiresolution Image Representation," *IEEE Transactions on Image Processing*, Vol. 14, pp. 2091-2106, 2005.
- [37] P. J. Burt and E. H. Adelson, "The Laplacian pyramid as a compact image code," *IEEE Transactions Commun.*, Vol. 31, No. 4, pp. 532540, Apr. 1983.
- [38] R. H. Bamberger and M. J. T. Smith, "A filter bank for the directional decomposition of images: Theory and design," *IEEE Transactions Signal Processing*, Vol. 40, No. 4, pp. 882-893, Apr. 1992.
- [39] M. N. Do and M. Vetterli, "Framing pyramids," *IEEE Transactions Signal Processing*, pp. 2329-2342, Sep. 2003.
- [40] M. N. Do, "Directional multiresolution image representations," Ph.D. dissertation, Swiss Federal Institute of Technology, Lausanne, Switzerland, December 2001.
- [41] AL Da Cunha, A.L, Jianping Zhou, Do. M.N, "The Nonsampled Contourlet Transform: Theory, Design, and Applications," *IEEE Transactions on Image Processing*, Vol.15, No.10, pp.3089-3101, Oct. 2006
- [42] K. Kaczmarek, B. Walczak, S. De Jong, and B.G.M. Vandeginste, "Baseline reduction in two-dimensional gel electrophoresis images," *ActaChromatographica*, Vol. 15, pp. 82-96, 2005.
- [43] S. Church, "Advances in two-dimensional gel matching technology," *Bio Chemical Soc. Transactions*, Vol. 32, pp. 511-516, 2004.
- [44] Motwani M., Gadiya M., Motwani R., Harris F Jr, "A Survey of Image Denoising Techniques," in *Proceedings of GSPx 2004*, September 27-30, 2004.
- [45] R. Rangarajan, R. Venkataramanan, and S. Shah., "Image denoising using wavelets," Technical report, College of Engineering, University of Michigan, 2002.
- [46] Donoho D. L., Johnstone I. M., "Adapting to Unknown Smoothness via Wavelet Shrinkage," *Journal of American Statistical Association*, Vol. 90, No. 432, 1995, pp. 1200-1224. doi:10.2307/2291512.
- [47] David L Donoho., "Denoising by soft thresholding," *IEEE Transactions on Information Theory*, Vol. 41, No. 3, pp. 613-627, May 1995.
- [48] S. LoPresto, K. Ramchandran, and M. T. Orchard, "Image coding based on mixture modelling of wavelet coefficients and a fast estimation quantization framework," in Proc. *IEEE Data Compression Conf., Snowbird, UT*, 1997, pp. 221230.
- [49] M. KivancMihcak, I Kozintsev, K Ramchandran, "Low-Complexity Image Denoising Based on Statistical Modelling of Wavelet Coefficients," *IEEE Signal Processing Letter*, Vol. 6, No. 12, Dec. 1999.
- [50] B. Natarajan, "Filtering random noise from deterministic signals via data compression," *IEEE Trans. of Signal Processing*, Vol. 43, pp. 25952605, Nov. 1995.
- [51] X. Zhang, f. Jia, S. Luo, G. Liu, Q. Hu, A marker-based watershed method for X-ray image segmentation, *Computer Methods and Programs in Biomedicine*, 113(3) (2014) 894-903, <http://dx.doi.org/10.1016/j.cmpb.2013.12.025>.

- [52] M. Hassan, A. Chaudhry, A. Khan, M. A. Iftikhar, Robust information gain based fuzzy c-means clustering and classification of carotid artery ultrasound images, *Computer Methods and Programs in Biomedicine*, 113(2) (2014) 593-609<http://dx.doi.org/10.1016/j.cmpb.2013.10.012>.
- [53] M. Gong et al., Fuzzy C-Means Clustering With Local Information and Kernel Metric for Image Segmentation, *IEEE Trans. Image Process.*,22(2) (2013) 573-584<http://dx.doi.org/10.1109/tip.2012.2219547>.
- [54] Yafeng Li, Wavelet-based fuzzy multiphase image segmentation method, *Pattern Recognition Letters*, 53(1) (2015) 1-8<http://dx.doi.org/10.1016/j.patrec.2014.10.013>.
- [55] T.F.Chan,L.A.Vese, Active contours without edges, *IEEE Trans. Image Process.*,10(2) (2001) 266-277<http://dx.doi.org/10.1109/83.902291>.
- [56] V. Ch. Korfiatis, P. A. Asvestas, G. K. Matsopoulos, Automatic local parameterization of the Chan Vese active contour model's force coefficients using edge information, *Journal of Visual Communication and Image Representation*, 29 (2015) 71-78<http://dx.doi.org/10.1016/j.jvcir.2015.02.008>.
- [57] Hui Kong,H.C. Akakin, S.E.Sarma, A Generalized Laplacian of Gaussian Filter for Blob Detection and Its Applications, *IEEE Transactions onCybernetics*,43(6) (2013) 1719-1733<http://dx.doi.org/10.1109/tsmcb.2012.2228639>.
- [58] C. S. Hoefflich, J. J. Corso, Segmentation of 2D gel electrophoresis spots using a Markov random field, *Progress in Biomedical Optics and Imaging 2009 - Proceedings of SPIE*, (2009) <http://dx.doi.org/10.1117/12.811802>.
- [59] H. Feng, B. Xiong, C. Sun, X. Xia, A Laplacian of Gaussian-based approach for spot detection in two-dimensional gel electrophoresis images, *Computer and Computing Technologies in Agriculture IV*, Springer Berlin Heidelberg, (2011) 8-15[http://dx.doi.org/10.1007/978-3-642-18369-0\\_2](http://dx.doi.org/10.1007/978-3-642-18369-0_2).
- [60] M. Persson, J. Bigun, Detection of spots in 2D electrophoresis gels by symmetry features, *Pattern recognition and data mining*, Springer Berlin Heidelberg, (2005) 436-445[http://dx.doi.org/10.1007/11551188\\_47](http://dx.doi.org/10.1007/11551188_47).
- [61] C. Fernandez-Lozano, J. A. Seoane, M. Gestal, D. Rivero, J. P. Dorado, A.,A texture-based classification method for proteins in two-dimensional electrophoresis gel images: A feature selection method using Support Vector Machines and Genetic Algorithms, *VISAPP 2013 - Proceedings of the 8th International Conference on Computer Vision Theory and Applications*, Barcelona, Spain, 1(2013) 401-404<http://www.scopus.com/inward/record.url?eid=2-s2.0-84878232924&partnerID=40&md5=94102d80d115b2578a43eb37e96b8108>.
- [62] U. Z. Ijaz, S. U. Chaudhary, S. D. Moon,Y. K. Kyung, Computational Strategies for Protein Quantitation in 2D Electrophoresis Gel Image Processor for Matlab, *Frontiers in the Convergence of Bioscience and Information Technologies* (2007) 129-134<http://dx.doi.org/10.1109/fbit.2007.95>.
- [63] P. Tsakanikas, E. S. Manolakos, Active contours based segmentation of 2DGE proteomics images, *16th European Signal Processing Conference*, (2008) 1-5.

- [64] S. Nhek, B. Tessema, U.G. Indahl, H. Martens, E.F. Mosleth, 2D electrophoresis image segmentation within a pixel-based framework, *Chemometrics and Intelligent Laboratory Systems*, 141 (2015) 33-46.
- [65] Massimo Natale, Alfonso Caiazzo, Enrico M. Bucci, Elisa Ficarra, A Novel Gaussian Extrapolation Approach for 2D Gel Electrophoresis Saturated Protein Spots, *Genomics, Proteomics & Bioinformatics*, (2012) ISSN 1672-0229, 10.1016/j.gpb.2012.06.005.
- [66] Matuzevičius, D., A. Serackis, and D. Navakauskas. Mathematical models of oversaturated protein spots. *Electronics and Electrical Engineering.–Kaunas: Technologija 1* (2007) 73.
- [67] K. Haris, S. N. Efstratiadis, N. Maglaveras, and A. K. Katsaggelos, “Hybrid image segmentation using watersheds and fast region merging,” *IEEE Trans. Image Processing*, vol. 2, pp. 1684–1699, Dec. 1998.
- [68] P. Salembier and M. Pardas, “Hierarchical morphological segmentation for image sequence coding,” *IEEE Trans. Image Processing*, vol. 3, pp. 639–651, Sept. 1994.
- [69] Kovacevic, J., Vetterli, M., Nonseparable two- and three-dimensional wavelets, *IEEE Transactions on Signal Processing*, 43(5)(1995) 1269-1273.
- [70] Jelena Kovacevic and Wim Sweldens, Wavelet Families of Increasing Order in Arbitrary Dimensions, *IEEE Trans. Image Process.*, 9(3) (2000) 480-496.
- [71] Kivanc Mihcak, M., Kozintsev, I., Ramchandran, K., Moulin, P., “Low-complexity image denoising based on statistical modeling of wavelet coefficients,” *Signal Processing Letters, IEEE* , vol.6, no.12, pp.300-303, Dec. 1999.
- [72] T. Lindeberg, Feature detection with automatic scale selection *International Journal of Computer Vision*, 30 (2) (1998), pp. 79–116
- [73] B. W. Silverman, *Density Estimation for Statistics and Data Analysis*. vol. 26, Chapman & Hall/CRC press, 1986.
- [74] Mallat, S., Zero-crossings of a wavelet transform, *IEEE Transactions on Information Theory*, 37(4)(1991) 1019-1033.
- [75] Cvetkovic, Z.; Vetterli, M., Discrete-time wavelet extrema representation: design and consistent reconstruction, *IEEE Transactions on Signal Processing*, 43(3)(1995) 681-693.
- [76] Millionsi, R., Sbrignadello, S., Tura, A., Iori, E., Murphy, E., Tessari, P. The inter- and intra-operator variability in manual spot segmentation and its effect on spot quantitation in two-dimensional electrophoresis analysis, *Electrophoresis*, 31(10) (2010) 1739-1742.
- [77] <http://world-2dpage.expasy.org/swiss-2dpage/>
- [78] J. Somasekar, B. Eswara Reddy, Segmentation of erythrocytes infected with malaria parasites for the diagnosis using microscopy imaging, *Computers & Electrical Engineering*, (2015) <http://dx.doi.org/10.1016/j.compeleceng.2015.04.009>.
- [79] V. Lempitsky, A. Zisserman, Learning to count objects in images, *Advances in Neural Information Processing Systems*, (2010) 1324-1332 <http://papers.nips.cc/paper/4043-learning-to-count-objects-in-images.pdf>.

- [80] R. S. Sengar, A. K. Upadhyay, M. Singh, V. M. Gadre, Analysis of 2D-Gel Images for Detection of Protein Spots Using a Novel Nonseparable Wavelet Based Method, *Biomedical Signal Processing and Control*, 25 (2016) 62-75.
- [81] R. S. Sengar, A. K. Upadhyay, M. Singh, V. M. Gadre, Wavelet Based Bimodal Image Segmentation for Blob Extraction with Application to 2D Gel Images, submitted.
- [82] "Wavelet and Fractals in Earth Science", Chapter-4: Multiscale Processing-A Boon for Self- similar Data, Data Compression, Singularities and Noise Removal", Ratnesh Sengar, Venkateswarao Cherukuri, Arpit Agrawal and Vikram M. Gadre, *CRC Press, Taylor & Francis Group*, 2013.
- [83] "Wavelet and Fractals in Earth Science", Chapter-3: Genesis of Wavelet Transform Types and Applications", S Sundararajan and N. Vasudha, *CRC Press, Taylor & Francis Group*, 2013.
- [84] A. Rangarajan, H. Chui, and J. S. Duncan, "Rigid point feature registration using mutual information," *Med. Image Anal.*, vol. 4, pp. 1–17, 1999.
- [85] S. Belongie, J. Malik, and J. Puzicha, "Shape matching and object recognition using shape context," *IEEE Trans. Pattern Anal. Mach. Intell.*, vol. 24, no. 4, pp. 509–522, Apr. 2002.
- [86] M. Rogers, J. Graham, "Robust and Accurate Registration of 2D Electrophoresis Gels Using Point-Matching," in *IEEE Transactions on image processing*, vol. 16, no. 3, pp. 624–635, March 2007.
- [87] P. J. Besl and H. D. McKay, "A method for registration of 3D shapes," *IEEE Trans. Pattern Anal. Mach. Intell.*, vol. 14, no. 2, pp. 239–256, Feb. 1992.
- [88] H. Chui, A. Rangarajan, J. Zhang, and C. M. Leonard, "Unsupervised learning of an atlas from unlabelled point-sets," *IEEE Trans. Pattern Anal. Mach. Intell.*, vol. 26, no. 2, pp. 160–173, Feb. 2004.
- [89] P. J. Huber, *Robust Statistics*. New York: Wiley, 1981.
- [90] S. Gold, C.-P. Lu, A. Rangarajan, S. Pappu, and E. Mjolsness, "New algorithms for 2D and 3D point matching: Pose estimation and correspondence," in *Advances in Neural Information Processing Systems*, G. Tesauro, D. S. Touretzky, and T. K. Leen, Eds. Cambridge, MA: MIT Press, 1994, pp. 1019–1031.